PREDICTIVE PORE-SCALE MODELLING OF MULTIPHASE FLOW

A DISSERTATION
SUBMITTED TO THE DEPARTMENT OF
EARTH SCIENCE AND ENGINEERING OF
IMPERIAL COLLEGE LONDON
IN PARTIAL FULFILMENT OF THE REQUIREMENTS
FOR THE DEGREE OF
DOCTOR OF PHILOSOPHY

Per Henrik Valvatne
2004

Abstract

I show how to predict flow properties for a variety of porous media using pore-scale modelling with geologically realistic networks. A state of the art pore-scale network model is developed for this purpose. It combines topologically disordered networks that represent real systems with detailed displacement mechanisms for any sequence of water and oil flooding, and any wettability. The model is verified by successfully predicting experimental relative permeability from a well described water-wet Berea sandstone. More complex experimental data are subsequently investigated. By developing a methodology combining realistic network topology with network properties tuned to easily obtainable experimental data such as mercury injection capillary pressures, I successfully predict flow properties for several porous media, initially applied to a water-wet sand pack. The wettability of the porous medium is recognized as being important for multiphase properties. I will first reproduce the surprising experimental trend whereby maximum oil recovery is achieved for systems with Amott wettability index around zero, and explain this behaviour from a pore-scale perspective. Subsequently I will combine careful wettability characterization with the methodology for modifying networks to successfully predict relative permeability for both oil- and mixed-wet datasets. For water flooding I introduce a method for assigning contact angles to match measured wettability indices. The aim of this work is not simply to match experiments, but to use easily acquired data to predict difficult-to-measure properties. Furthermore, the variation of these properties in the field, due to wettability trends and different pore structures, can now be predicted reliably.

Acknowledgements

I would like to thank my advisor Professor Martin J. Blunt for his constant support, guidance and encouragement during this study. Without his assistance, this work would have not been accomplished. Statoil, and in particular Dr. Pål-Eric Øren, is thanked for many helpful discussions, both during my stay at the Statoil research centre in Trondheim and during his visits to Imperial College. If it had not been for Statoil kindly letting me use some of their networks, this work would certainly not have turned out this successful. As the title suggests, the focus of this thesis is on predictive pore-scale modelling, something that is not possible without comparison to real data. It has been very much appreciated that both Shell and Statoil have given us access to complete datasets, something that has made this work stronger than if I would had to rely only on published material. I look forward to continue research into pore-scale modelling, something that has been made possible by Shell deciding to employ me. Dr. Xudong Jing is thus thanked for championing the cause of pore-scale modelling within Shell, and for being extremely helpful in finding good experimental data for us to use. Financial support from the sponsors of the Imperial College Consortium on Pore-Scale Modelling is gratefully acknowledged.

Contents

List of Tables

List of Figures

Chapter 1

Introduction

The understanding of multiphase flow in porous media is of great importance in many fields such as hydrology, contaminant cleanup and petroleum engineering. Macroscopic properties – principally capillary pressure and relative permeability – are often needed when modelling flow and transport at the continuum scale, whether it be transport of non-aqueous phase liquids (NAPL) in contaminant clean-up or the production of oil during reservoir water flooding. These macroscopic properties are, however, difficult to obtain. It is possible to conduct physical experiments on samples of the reservoir, but this will only reflect one set of conditions. Furthermore, the scale of the reservoir itself is so much larger that a few experiments are unlikely to describe the variation likely to be present. Hence, there is a need to develop physically-based models that can predict multiphase flow and transport properties and their likely variation in a reservoir setting, based on readily available experimental data.

Though many models have been suggested over the years, the focus of this thesis will be on network modelling wherein the void space of the porous medium is represented at the microscopic scale by a lattice of pores connected by throats. By applying rules that govern the transport and arrangement of fluids in pores and throats, macroscopic properties, for instance capillary pressure or relative permeability, can then be estimated across the network, which typically consists of several thousand pores and throats representing a rock sample of a few millimetres cubed.

In Chapter 2 I will conduct a literature review of the current state of network modelling, with special emphasis on the use of network models to predict experimental data. This has mainly become possible through the use of networks that are realistic representations of porous media, and a better understanding of wettability effects on the pore-scale. Two main approaches to generate realistic networks have been reported in the literature. From a voxel-based representation of the porous medium, either numerically constructed or directly imaged, a topologically equivalent network can be directly generated. Alternatively, one can use a regular network but map the statistical properties of the porous medium, obtained from image or experimental data, onto it. Both of these methods will be reviewed.

Chapter 3 will describe the mathematical details and assumptions made that are at the foundations of the computer code that has been written as part of this thesis to simulate multiphase flow in network models. Details about generating the networks themselves will however be ignored, as this does not form part of this thesis. The computer code is written in such a way that no assumptions are made about the topology of the network.

The computer code described in Chapter 3 will then be subsequently used to predict experimental data. In Chapter 4 only water-wet media will be considered. As wettability is easier to characterise in this case, it will allow us to focus on verifying the details of the implemented network model. We will also introduce a methodology for modifying networks using easily obtainable experimental data. A network originally constructed to represent a Berea sandstone will be modified to predict multiphase properties of a sand pack.

Very few porous media are in fact water-wet, and the influence of wettability on predicted flow properties will be investigated in Chapter 5. First, we will try to predict production characteristics of mixed-wet systems for which we have a specific realistic network. Subsequently we will combine the methodology for modifying networks with prediction of different mixed-wet and oil-wet media. Experimental capillary pressure and relative permeability data from both reservoir sandstones and carbonates will be used. We will also introduce a new method for distributing mixed wetting at the pore-scale, and show how this improves the predictions of a reservoir sandstone. Finally, in Chapter 6 we will summarize the important findings of this work, and give some thoughts about the application and future direction of predictive pore-scale modelling.

The following articles have all been either based on material presented in this thesis, or used the computer code developed for this thesis:

- Blunt, M.J., M.D. Jackson, M. Piri and P.H. Valvatne, Detailed physics, predictive capabilities and macroscopic consequences for pore-network models of multiphase flow, *Advances in Water Resources*, 25, 1069-1089, 2002.
- Jackson, M.D., P.H. Valvatne, and M.J. Blunt, Prediction of wettability variation and its impact on waterflooding using pore- to reservoir-scale simulation, proceedings of the 2002 SPE Annual Technical Conference and Exhibition, SPE 77543, Soc. of Petroleum Engineers, San Antonio, 2002 (accepted by SPEJ).
- Jackson, M.D., P.H. Valvatne, and M.J. Blunt, Prediction of wettability variation and its impact on flow using pore- to reservoir-scale simulations, *Journal of Petroleum Science and Engineering*, 39, 231-246, 2003.
- Lopez, X., P.H. Valvatne, and M.J. Blunt, Predictive network modeling of single-phase non-Newtonian flow in porous media, *Journal of Colloid and Interface Science*, 264, 256-265, 2003.
- Lopez, X., P.H. Valvatne, and M.J. Blunt, Use of network modeling to investigate single-phase polymer flow in porous media, *Journal of Non-Newtonian Rheology*, submitted, 2003.
- Valvatne, P.H., M. Piri, X. Lopez and M.J. Blunt, Predictive pore-scale modeling of single and multiphase flow, proceedings of the ESF Workshop on Recent Advances in Multiphase Flow and Transport in Porous Media, European Science Foundation, Delft, 2003 (submitted to *Transport in Porous Media*).
- Valvatne, P.H. and M.J. Blunt, Predictive pore-scale network modeling, proceedings of the 2003 SPE Annual Technical Conference and Exhibition, SPE 84550, Soc. of Petroleum Engineers, Denver, 2003.
- Valvatne, P.H. and M.J. Blunt, Predictive pore-scale modeling of two-phase flow in mixed-wet media, *Water Resources Research*, submitted, 2003.

Chapter 2

Literature Review

Modelling flow behaviour using network models was pioneered by Fatt in the 1950s [1956a; 1956b; 1956c]. By distributing the pores and throats on a regular 2D lattice and sequentially filling them in order of inscribed radius using the Young-Laplace equation, he was able to produce capillary pressure and relative permeability curves for drainage (as a function of average saturation) that had the same characteristics as those obtained experimentally. He investigated the effects of different network lattices (square, triangular, honeycomb and double-hexagonal) and found that these gave results that were closer to experimental measurements than assuming that the porous medium could be modelled as a bundle of parallel tubes. The pore size distribution was found to be more important for the results than were differences between lattices. Fatt computed the flow properties using an equivalent physical network of electrical resistors, since at the time (1956), numerical solution of the flow/conductance equations was not possible.

Further advances in network modelling didn't occur until the late 1970s when computer processing power became more readily available. Chatzis and Dullien [1977] focused on the assumptions made earlier by Fatt. They noted that 2D networks could not reliably predict the behaviour in 3D, which until then had been a common assumption. The percolation threshold, when one phase spanned the system, was found to be highly dependent on the dimensionality of the problem, as predicted by percolation theory. They also noted the importance of coordination number z (the number of throats connected to a pore), with breakthrough occurring later with reduction in average z. Their networks consisted of both pores and throats, both of which had assigned volumes. The invading fluid was injected from the inlet face and filled pores and throats in order of radius, in a similar process to that described by Wilkinson and Willemsen [1983] who introduced the concept of invasion percolation, which is the theoretical foundation for drainage, and will be described in detail later. They also allowed clusters of defending fluid to become surrounded by the invader and become trapped. Trapping was further investigated by Dias and Wilkinson [1986].

Micro-model experiments of drainage and imbibition allowed the pore-scale physics of displacement to be understood. Lenormand *et al.* [1983] used models with rectangular cross-section capillaries to observe and describe the displacement processes in imbibition that still are at the foundations for network modelling – piston-like displacement, snap-off and cooperative pore-body filling. The details of these processes will be described later.

2.1 Description of the Pore Space

Until recently most networks were based on a regular lattice. The coordination number can vary depending on the chosen lattice (e.g. 5 for a honeycombed lattice or 6 for a regular cubic lattice). Chatzis and Dullien [1977] compared their results from regular networks to experimental mercury intrusion data from sandstones, and noted that regular networks combined with circular capillaries did not yield a realistic description of real sandstones.

Jerauld and Salter [1990] performed an extensive study of relative permeability and explained the trends seen using pore-scale network modelling. Using a cubic lattice with circular capillaries they were able to reproduce the features of relative permeability curves seen in experiments. They found that the most important structural property of the network was the size aspect ratio between pore-bodies and throats. This was found to influence significantly the amount of relative permeability hysteresis between flooding cycles as well as the shape of the curves. Also influencing the shape was the spatial correlation of pore and throat sizes, and to some degree the pore size distribution.

In order to match the coordination number of a given rock sample, which typically is between 3 and 8 [*Jerauld and Salter*, 1990], it is possible to remove throats from a lattice of higher coordination number. Dixit *et al.* [1997], again using a regular cubic lattice, found that in less well-connected media, with an average coordination number of 4 rather than 6, the size aspect ratio between pore-bodies and throats had less influence on the relative permeability. The reduced connectivity of the network was found to dominate the relative permeability hysteresis.

To better reflect real porous media it is possible to randomly distribute points within the model area and then construct a network from the triangulation of these points. Jerauld *et al.* [1984a; 1984b] constructed random networks from Voroni diagrams. These networks had an initial coordination number of more than 15. This was subsequently reduced by removing the longest throats until an average coordination number of 6 were achieved. However, little difference in relative permeability was observed when comparing to regular networks [*Jerauld and Salter*, 1990]. Blunt and King [1990; 1991] constructed networks using a similar approach. These were then used to investigate the influence of both capillary and viscous forces on pore-scale displacements.

All the methods described so far fail to capture any of the statistics associated with real porous media. The use of networks derived from a real porous medium was pioneered by Bryant *et al.* [1992; 1993a; 1993b]. They extracted their networks from a random close packing of equally-sized spheres in which all sphere coordinates had been measured. They included compaction effects (by moving the sphere centres closer together vertically) and cementation (by increasing the spheres radii without moving their coordinates). They were able to show that the hydraulic conductivities of the network were spatially correlated and made good predictions of the trend in permeability with porosity for Fontainebleau sandstone. In contrast, using a statistically equivalent but uncorrelated network, the permeability was over-predicted by a factor of two [*Bryant et al.*, 1993b]. This finding shows the crucial importance of using geologically realistic networks when predicting flow behaviour. Other transport properties, such as relative permeability and electrical conductivity, as well as capillary pressure, were also compared successfully with experimental results from sand packs, bead packs and a simple sandstone. However, since their networks were based on a pack of equally-sized spheres, resulting in a constant coordination number of 4, the application to more complex sandstones was limited.

In order to capture the connectivity of a real rock and reproduce this in the subsequent network representation, the rock itself has to be analyzed. It is common to do this in a two-step approach. First a 3D voxel-based representation (typically in a binary format where 0 indicates matrix and 1 void space) of the pore space is created that should capture the statistics of the real rock, from which an equivalent network (in terms of topology, pore volume, throat radii, clay content*, etc*) is then extracted. Neither of these steps is exclusive to the field of network modelling, and both can be treated independently.

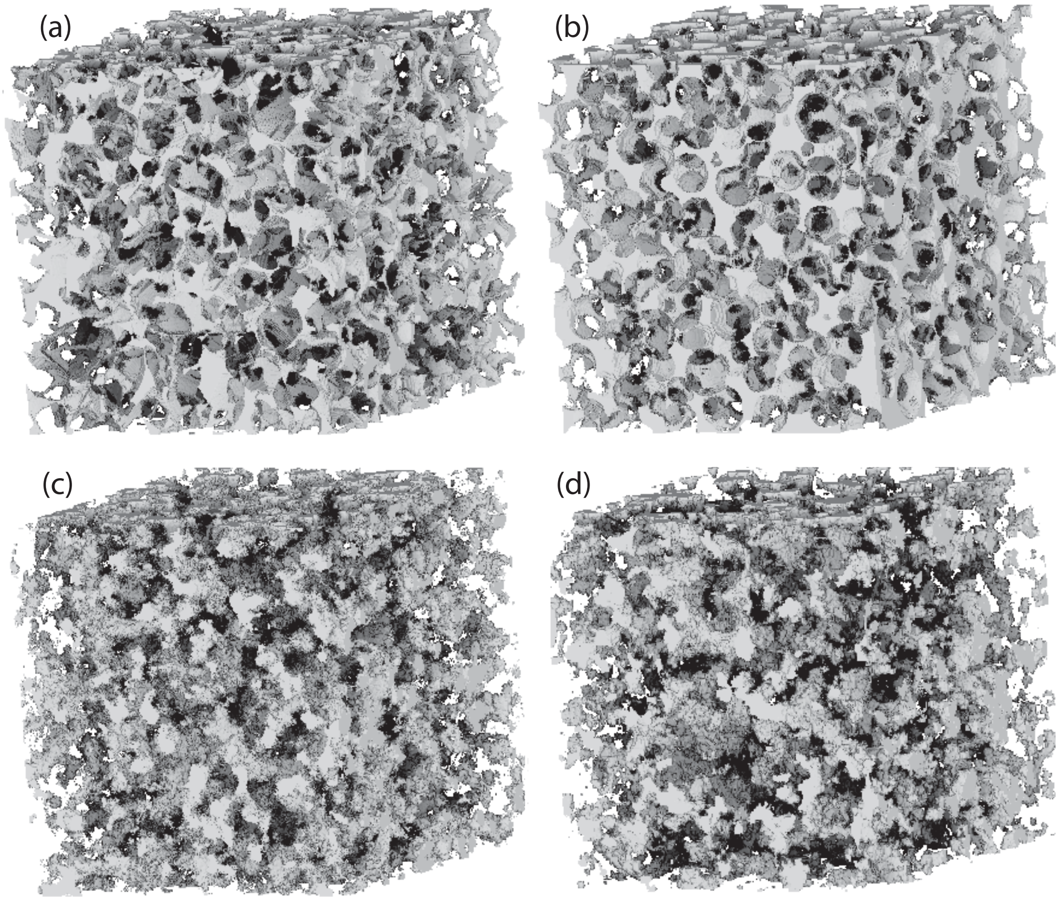

Figure 2.1: Comparison between different 3D voxel representations of a Fontainebleau sandstone [*Biswal et al.*, 1999], generated using different reconstruction techniques. The side length of each sample is 2.25 mm. (a) X-ray microtomography. (b) Object-based modelling. (c) Gaussian field technique. (d) Simulated annealing.

The pore space description can be generated directly using X-ray microtomography [*Dunsmuir et al.*, 1991; *Spanne et al.*, 1994; *Coker et al.*, 1996], where the rock is imaged at resolutions of around a few microns. This can be done due to the differences in X-ray absorption of rock matrix and void space. A 3D image of a Fontainebleau sandstone is shown in Figure 2.1 (a) along with a 2D cross-section in Figure 2.2 (a). This method has the advantage of directly reconstructing the pore space, but due to the specialized scanners required, it is not readily available and also very costly. It is, however, very useful for validating numerical reconstruction techniques of the microstructure, described below.

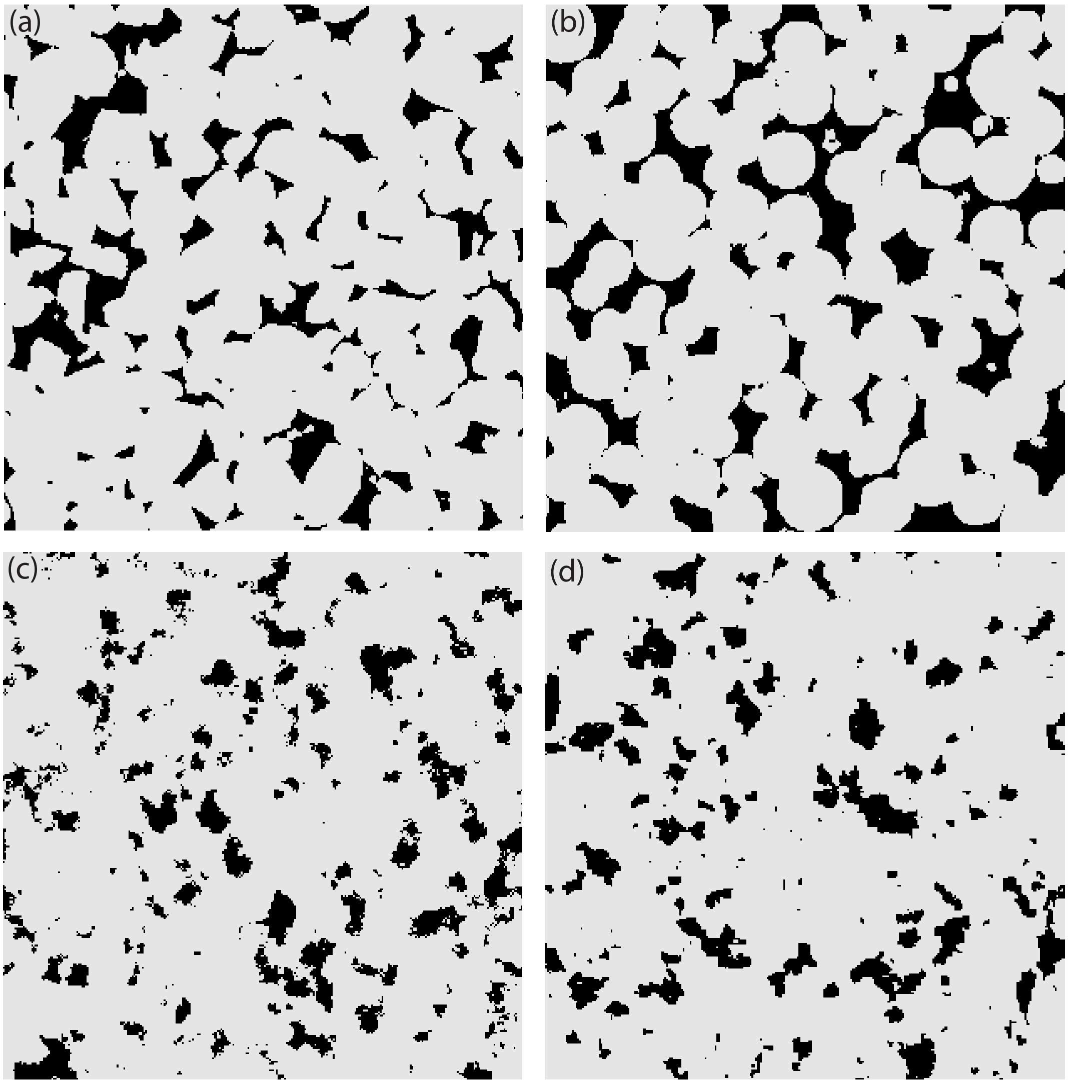

Figure 2.2: Comparison between different 2D cross-sections of a Fontainebleau sandstone [*Biswal et al.*, 1999], generated using different reconstruction techniques. The side length of each sample is 2.25 mm. (a) X-ray microtomography. (b) Object-based modelling. (c) Gaussian field technique. (d) Simulated annealing.

It is possible to generate a 3D model of the pore space by reproducing statistical information measured on 2D thin sections, of which an example is shown in Figure 2.3. Porosity, also called the one-point correlation function, and the two-point correlation function, measuring the probability of finding two points separated by a distance **u** within the same phase, pore or matrix, are the most basic quantities used to characterize porous media. However, both of these methods fail to incorporate any information about the underlying topology of the porous medium. The lineal-path function is the probability of finding a line segment of length L completely within either the pore space or matrix [*Lu and Torquato*, 1992]. This provides more characterization of the structure of the medium as the function can be evaluated on a specific phase (pore space or matrix). It also has the benefit of being relatively quick to evaluate.

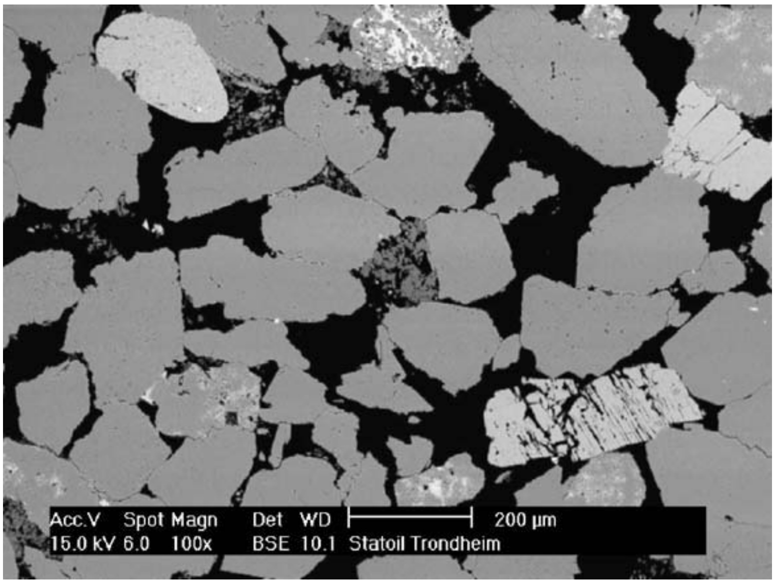

Figure 2.3: 2D thin section image of a Berea sandstone, generated using back scatted electron (BSE) imaging. The pore space is black, matrix is light grey and clay minerals are dark grey [*Øren and Bakke*, 2003].

Hilfer [1991] introduced the concepts of local porosity distribution and local percolation probability to improve the geometric characterization of porous media. Local porosity distribution is the probability density of finding the local porosity ϕ in the range $\phi \pm \Delta\phi$ in a cell of side lengths L. From the resulting histogram and porosity variance it is possible to get an indication of the level of heterogeneity within the investigated volume. Local percolation probability is a measure of the connectivity of the sample, measuring the fraction of cells with side length L that percolate in a given direction (a continuous path through the cell exists). This is clearly an important characteristic of the reconstructed porous medium as it has a direct relation to the transport properties, something that is not captured by the other quantitative measures.

Most stochastic reconstruction algorithms are based on thresholded Gaussian field techniques. Adler and Thovert [1998] have written an extensive review article on these. They are based on porosity and two-point correlation functions, both of which can be readily obtained by image analysis of 2D thin sections. The technique is similar to that used in geostatistics. A continuous correlated field is generated using Fourier transform methods and thresholded to retrieve the binary phases (pore space and matrix) with the correct porosity and correlation function, Figure 2.2 (c) and Figure 2.3 (c). This method can also be extended to include more phases, such as clays.

Realising that the earlier Gaussian based methods were not very good at reproducing the underlying particulate structures of the porous media, as evident from Figure 2.3 (c), Yeong *et al.* [1998b; 1998a] developed a stochastic method based on simulated annealing, later extended by Manwart *et al.* [2000]. Rather than being restricted to one- and two-point correlation functions, the objective function used can be made to match additional quantities such as multi-point correlation functions, lineal-path function or pore size distribution function to name a few. Since the method is based on moving pore-space voxels around to minimize the objective function, the correct porosity is always retained. They subsequently reconstructed a 3D Fontainebleau and Berea sandstones from 2D sections using an objective function based on both two-point correlation function and either lineal-path or pore size distribution function, Figure 2.2 (d) and Figure 2.3 (d). The estimated percolation probability was closer to the reference than when only using the two-point correlation function. Incorporating more higher-order information into the objective function, such as the local percolation probability, would most likely improve the reconstruction further, but that would also increase the computational cost of the method significantly.

Another technique is the use of object-based modelling whereby the actual rock-forming process is simulated. Packing algorithms for spheres are well established [*Adler and Thovert*, 1998] and algorithms for arbitrary shapes have also been presented by several authors [*Coelho et al.*, 1997; *Pilotti*, 2000; *Jia and Williams*, 2001; *Latham et al.*, 2001; *Latham et al.*, 2002]. An algorithm that takes into account the whole rock-forming process where primary grain sedimentation is followed by compaction and diagenesis has been presented by Bakke and Øren [1997; 2002] and later by Jin *et al.* [2003]. A grain size distribution is determined from image analysis of thin sections. Grains are then randomly picked from this distribution during the sedimentation process. Compaction is modelled by moving the centre of each grain down in proportion to its original vertical position. Finally, diagenetic processes are modelled. Quartz overgrowth is modelled by increasing the radii of the grains, and clays are precipitated on quartz surfaces. The amount of diagenesis to include is also determined from thin section analysis. Though this reconstruction method does not guarantee that statistical geometrical parameters such as the two-point correlation functions are honoured, it is assumed that these will be adequately reproduced since the actual rock-forming process is simulated, Figure 2.2 (b) and Figure 2.3 (b).

Biswal *et al.* [1999] performed a quantitative comparison of three reconstruction methods (Gaussian field, simulated annealing and object-based) on a Fontainebleau sandstone, where the reference, containing 300^3 voxels, was obtained using microtomography. They found that the object-based technique reproduced the two-point correlation function reasonably well. When comparing connectivity using local percolation probability it was clear that the object-based technique was far superior to the statistical techniques. This agrees with analysis performed by Øren and Bakke [2002] and Hilfer [2000].

Recently several statistical reconstruction techniques have been suggested that try to improve on the deficiencies of the Gaussian field techniques, while not being as computationally demanding as simulated annealing. Thovert *et al.* [2001] introduced a method that is a hybrid between the statistical and object-based methods. Their technique is statistical, using only porosity and two-point correlation function, but conditioned to an underlying granular structure, defined using a pore size distribution derived from the two-point correlation function. This is based on a Poissonian penetrable sphere model. They verified their method using a 3D Fontainebleau sample and reported good agreement with the reference, even for the percolation probability. Hilfer and Manswart [2001; 2002] also developed a hybrid between statistical and object-based method. Initially a close packing of spheres is laid down. Matrix voxels are then randomly distributed in the pore space until a prescribed porosity is attained. The configuration of the added matrix voxels are then updated using simulated annealing, matching the two-point correlation function. They also verified their method using a 3D Fontainebleau sample and the local percolation probability was found to be significantly better than traditional simulated annealing though not quite as good as a traditional object-based method.

For many types of porous media it might, however, be difficult to define the structures that make up the matrix. In carbonate rocks post-depositional diagenesis often completely dominates the matrix structure [*Lucia*, 1999], making object-based techniques difficult to use. In field-scale reservoir characterization the same problems are often experienced where there are multiple facies with distinctive connected geometries; for example, in fluvial reservoirs. Gaussian field techniques will not reproduce the channel connectivity whereas object-based methods rely on the facies geometries being easily parameterized. Strebelle [2002] suggested a statistical algorithm in which the multiple-point statistics were inferred from exhaustive 2D training images of equivalent reservoir structures and then used to reconstruct the reservoir, adhering to any conditioning data. This method was applied successfully to both fluvial and more complex patterned reservoirs. The ability to reproduce any pattern makes this method highly attractive for reconstructing complex porous media like carbonates. Okabe *et al.* [2003] have used this algorithm to reconstruct a 3D Fontainebleau sandstone from a 2D training image. Although the granular structure is not as well reproduced as in object-based methods, the local percolation probability is significantly better reproduced than that achieved by other statistical methods such as Gaussian field techniques.

2.2 Methods to predict transport properties

When estimating single phase transport properties like absolute permeability it is possible to conduct flow experiments directly on the 3D reconstructed sample. Many authors have reported good agreement with experimentally obtained values when solving the Stokes equation for single phase flow using finite difference methods [*Roberts et al.*, 1996; *Adler and Thovert*, 1998; *Hilfer and Manwart*, 2001; *Manwart and Hilfer*, 2002; *Øren and Bakke*, 2002] or the Lattice-Boltzmann method [*Manwart et al.*, 2002]. The importance of reproducing long-range connectivity in any reconstruction technique is clearly evident from calculations of absolute permeability. Whereas object-based methods reproduce permeability values within a few percentage points, traditional Gaussian field techniques and simulated annealing typically under-predict permeability by about a factor of ten for low porosity systems that are close to the percolation threshold [*Hilfer and Manwart*, 2001; *Manwart et al.*, 2002; *Manwart and Hilfer*, 2002; *Øren and Bakke*, 2002]. For higher porosity systems, the statistical methods generally perform somewhat better at reproducing the local percolation probability [*Manwart et al.*, 2000], with permeability predicted within a factor of about five [*Øren and Bakke*, 2003].

Even single phase simulations conducted directly on the 3D reconstructed sample are computationally very expensive. A common way to model both single and multiphase flow quickly on large systems is to represent complex porous media by an equivalent network of pores and connecting throats. Absolute permeability has been successfully predicted, as already mentioned, by Bryant *et al.* [1993b] using this method. Another approach is to skip the 3D reconstruction process and estimate absolute permeability directly from the 2D thin sections. Lock *et al.* [2002] computed a distribution of fluid conductances by recoding pore areas and perimeter lengths. From this a single effective conductance was found using effective medium theory, resulting in a direct estimate of absolute permeability. This approach was applied to a number of sandstone thin sections with predicted absolute permeabilities generally within a factor of 2 of the measured values.

For multiphase flow it is possible to use Lattice-Boltzmann techniques [*Gunstensen and Rothman*, 1993; *Chen and Doolen*, 1998; *Hazlett et al.*, 1998] to solve the transport equations on the 3D reconstructed sample. Being computationally very demanding, their use in multiphase flow problems is, however, limited to relatively small systems. As a consequence their applications are more tailored towards understanding the fundamental physics of flow in complex systems rather than for quantitative predictions.

A whole range of empirical or semi-empirical methods for predicting relative permeability have suggested over the last five decades [*Dullien*, 1992]. One of the most widely used is found by combining the model by van Genuchten [1980], relating effective wetting saturation to capillary pressure, with the model for relative permeability by Mualem [1976]. Empirical fitting parameters are found by matching the van Genuchten model to experimental capillary pressure. These parameters are subsequently used for the relative permeability predictions. However, what most of these models have in common is that they are only applicable for strongly water-wet data, and many of them also rely on difficult to define parameters such as tortuosity exponents.

In this work, the approach chosen for predicting multiphase flow properties is pore-scale network modelling. In the following section we will therefore review in some detail the aspects for constructing and modelling flow through such networks.

2.3 Networks, pore shapes and wetting layers

2.3.1 Constructing networks

In cases where the matrix is just made up of a random packing of equal spheres, an equivalent network of pores and connecting throats can be created by tessellating the pack into tetrahedral cells. The pores will then be the cells, with throats being where cells share a common face [*Bryant et al.*, 1993b]. This method can, however, not be used in more complex voxel-based representations of the pore space. In those cases the skeleton of the pore space is first created, consisting of the centre-lines of the pore space.

Lindquist *et al.* [1996; 1999; 2000] extended a thinning algorithm [*Lee et al.*, 1994] in which the pore space is eroded until only the centre-lines remain. Though they didn't create networks on which to perform fluid flow simulations, they did analyze geometric properties such as connectivity and tortuosity of skeletons generated from various micro-CT imaged rock samples. Liang *et al.* [1998] proposed an improvement to the existing thinning algorithms. This method was applied to statistically reconstructed samples of Berea sandstone and chalk [*Talukdar et al.*, 2002]. One cause of concern was however that the level of smoothing applied to the reconstructed sample gave rise to significant differences in the topology of the skeleton [*Liang et al.*, 2000]

The problem with pore space thinning algorithms is that pore space irregularities can create additional line segments and multiple vertices often have to be merged into a single pore. This can easily result in the subsequent network becoming too tortuous [*Bakke and Øren*, 1997]. When generating networks from object-based reconstruction methods, one is aided by being able to easily identify the separate grains. By dilating each grain until adjacent grains meet, a Voroni diagram is created. The skeleton is then simply the points on the boundary surfaces that have neighbouring voxels from three or more grains with pore locations being points with four or more neighbouring grains [*Bakke and Øren*, 1997]. The area, perimeter and radius of each throat are defined by rotating a vector about the pore space centreline in the reconstructed medium, recording the values at the narrowest constriction and the averages. For pore bodies the vector is rotated about the centre point, using the average of the recorded values. Volumes are calculated by simply counting the voxels. A network constructed using this method is shown in Figure 2.4 (b).

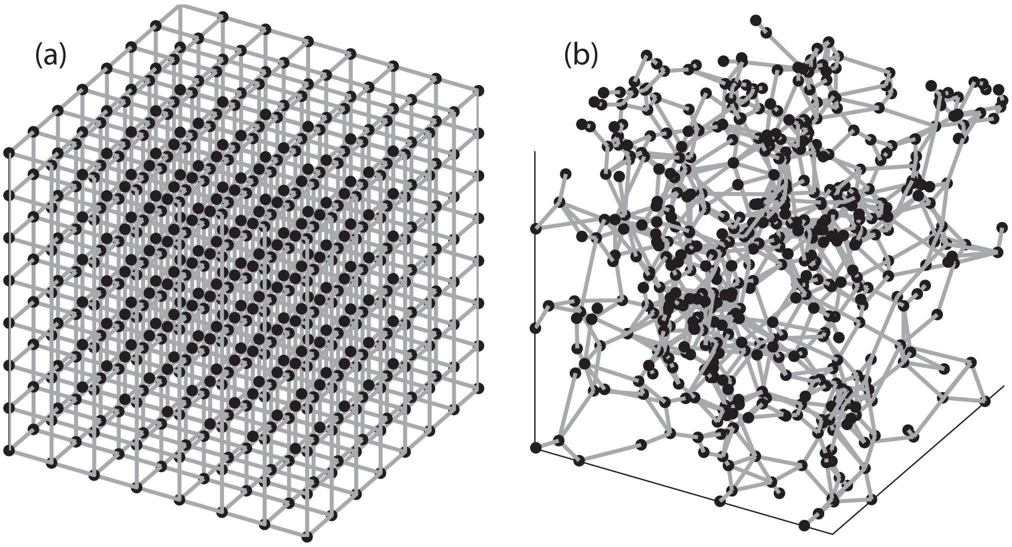

Figure 2.4: Different network lattices consisting of 512 pore bodies. (a) A regular cubic lattice with a constant coordination number of 6. (b) From a 3D voxel-based representation of the pore space it is possible to construct a topologically equivalent network [*Bakke and Øren*, 1997]. The average coordination number in this case is 3.6.

An alternative to the thinning and dilation approaches has been suggested by Delerue *et al.* [1999; 2002] whereby the skeleton is created from the Voronoi diagram of the pore space. Although this method does not ensure the connectivity of the skeleton, as the others methods do, good agreement with experimentally obtained conductivity was reported for a soil that had been imaged with microtomography.

When using pore-scale modelling to predict experimental data, it is clearly important that the underlying network is representative of the rock. However, if the exact rock type has to be used for the network construction, the application of predictive pore-scale modelling will be severely limited due to the complexity and cost of methods such as X-ray microtomography. How much information about the rock is needed in the network representation in order to make good predictions of experimental data thus becomes an important question. Chatzis and Dullien [1977] noted the importance of coordination number on flow behaviour while Bryant *et al.* [1992; 1993a; 1993b] could only get good predictions of permeability when spatially correlating the geometric properties of the network elements.

2.3.2 Calibrating networks using capillary pressure

Capillary pressure as a function of wetting phase saturation has commonly been used as a tool to calibrate the network model due to the close relationship to the distribution of inscribed radii [*Dullien*, 1992]. Wise [1992] used measured capillary pressure combined with the Laplace equation to randomly distribute the radii on a regular cubic lattice, of which an example is shown in Figure 2.4 (a). The throats with the smallest radii were subsequently removed from the network until a match with the absolute permeability was achieved, resulting in a network with coordination number less than six.

Rajarman *et al.* [1997] also conducted simulations on cubic networks but the throat radii were both spatially correlated in a given direction as well as cross correlated between throats connected to a single pore. Cross correlation was found to influence both the capillary pressure response and relative permeability more than did the spatial correlation. Both the pore size distribution and correlation parameters were subsequently optimized to obtain a best possible match between predicted and experimental capillary pressures for various unconsolidated soils. These networks were then used to predict primary drainage wetting phase relative permeability with some encouraging results.

Fischer and Celia [1999] calibrated their networks to capillary pressure very similarly to Rajarman *et al.* [1997]. Experimental data from a wide range of unconsolidated soils were used to test the methodology, with relative permeabilities available for both water and gas. The matches with capillary pressures were generally good, as were the predicted absolute and water relative permeabilities. For gas relative permeability the hysteresis between secondary drainage and tertiary imbibition was under predicted, resulting in relatively poor predictions. They noted that additional structural components were needed in the network topology if improvement in the predictions were to be achieved.

An alternative to using capillary pressure when calibrating network models is to infer the properties from the reconstructed sample of the sandstone. In this approach the network is not constructed directly from the voxel representation, but rather its statistical properties are mapped onto a regular grid. This approach is motivated not just by the fact that capillary pressure might not always be available, but also by the observation that the optimized pore size distribution obtained in the previous methods is not unique [*Vogel*, 2000]. Depending how the pore sizes were spatially correlated, a good match with the reference capillary pressure could be obtained with significantly different pore size distributions.

Vogel and Roth [1997; 1998; 2001] obtained pore size distribution and pore connectivity from reconstructed samples of unconsolidated soils. The reconstruction was obtained by multiple 2D thin sections. Rather than obtaining a continuous pore size distribution, the range of pore sizes was divided into set number of bins (typically 10), obtained using an erosion-dilation approach. At each size interval the connectivity of pores larger than that size is quantitatively measured. When subsequently constructing the network representation, a face-centred cubic lattice with a maximum coordination number of 12, and the same pore size distribution and pore connectivity measure was imposed. The pore connectivity will affect both the distribution of pore sizes as well as the effective coordination number. Predicted primary drainage capillary pressures and hydraulic conductivities were then compared against experimental results. Though the predictions clearly were worse than those obtained by Fischer and Celia [1999], they were considerably better than those obtained when excluding the effects of pore connectivity in the network construction.

Hilpert *et al.* [2003] used a similar approach to that of Vogel and Roth, though using a regular cubic lattice rather than a face-centred one and explicitly modelling pore bodies as well as throats. By also introducing cross correlation between throats sizes connected to a single pore they were able to predict both experimental primary drainage and imbibition capillary pressures for different sphere packs with reasonable accuracy.

Tsakiroglou and Paytakes [2000] combined extracting statistical properties from reconstructed samples with conditioning to capillary pressures from mercury intrusion and retraction. First pore size distribution and connectivity information is extracted from thin section analysis with throat size distribution estimated from the experimental capillary pressures. These parameters are then optimized along with the coordination number distribution using a regular cubic lattice until a satisfactory match with both intrusion and extraction capillary pressures are obtained. The performance of the method was however only measured by the match to capillary pressure and predicted absolute permeability, both of which were quite good. No additional transport properties were predicted.

Using reconstructed samples of Fontainebleau sandstones, obtained by microtomography, Sok *et al.* [2002] compared transport predictions from topologically equivalent networks to those based on a face-centred cubic lattice with the same statistical properties. Even when including spatial and cross correlation for pore and throat sizes as well as the correct distribution of coordination numbers, the regular lattices gave poor predictions of both invasion pattern and residual saturations. Their conclusion was that those statistical parameters that can be easily obtained from the reconstructed medium are not sufficient for reliable predictions of transport properties and that additional higher-order topological information is needed.

The predicted transport properties are obviously not just a function of lattice topology and pore size distribution but also how each individual pore element is represented and the amount of pore-scale physics they can accommodate. Most of the network models described so far have been modelled as a collection of cylindrical tubes representing the throats, though in the work by Fischer and Celia [1999] the throats had a biconical shape rather than a uniform cylinder. It was argued by Reeves and Celia [1996] that this allowed for more accurate calculation of volumes and interfacial area as the location of possible fluid interfaces in throats could be accurately resolved. It also helped minimize trapping of wetting fluid in throats during drainage with the throats being allowed to drain if the interface from each side touched.

If pores were explicitly included they were often modelled as spheres or cylinders. In the work of Bryant *et al.* [1992; 1993a; 1993b] the throats were assumed to control flow through the network, with the pores contributing volume. McDougall and Sorbie [1995; 1997] used a similar approach but only assigned volume to the throats. In some finer textured soils it was argued by Vogel [2000] that this was a better representation of the pore morphology than placing all the volume in pore bodies.

2.3.3 Wetting layers

The major restriction from only using circular tubes in network modelling is their inability to contain more than one fluid. The pore space in real rock is highly irregular with wetting fluid remaining in grooves and crevices due to capillary forces, even after the centre has been occupied by non-wetting fluid. This behaviour has been extensively observed in micromodel experiments where the flow channels typically have a square cross-section [*Lenormand et al.*, 1983] The wetting layers might not be more than a few microns in thickness, with little effect on overall saturation or flow. Their contribution to wetting phase connectivity is however of vital importance, ensuring low residual wetting phase saturation due to the prevention of trapping. Wetting films, as observed by Dullien *et al.* [1989] in smooth bead packs, are only nanometers in thickness, stabilized by molecular forces. These covered the smooth beads but were found not to conduct hydraulically and contributed negligibly to saturation. The wetting fluid was trapped in pendular rings between the beads, resulting in a residual saturation of 9 percent. Once the beads were etched in acid, creating grooves in the surface, the residual wetting phase saturation fell to 1 percent as a result of flow in layers.

It is clear that a network model consisting exclusively of circular tubes will not capture this behaviour, resulting in wrong predictions for residual saturation, transport properties and hysteresis effects. Kovscek *et al.* [1993] suggested using star shaped tubes in order to capture the effects of wetting layers. This is the same cross-sectional shape as that resulting from using grain boundary shaped throats, as used by for example Man and Jing [1999; 2000; 2001]. Other popular pore shapes include squares [*Blunt*, 1997a, 1998; *Fenwick and Blunt*, 1998; *Dillard and Blunt*, 2000] and equilateral triangles [*Hui and Blunt*, 2000]. These different shapes are illustrated in Figure 2.5.

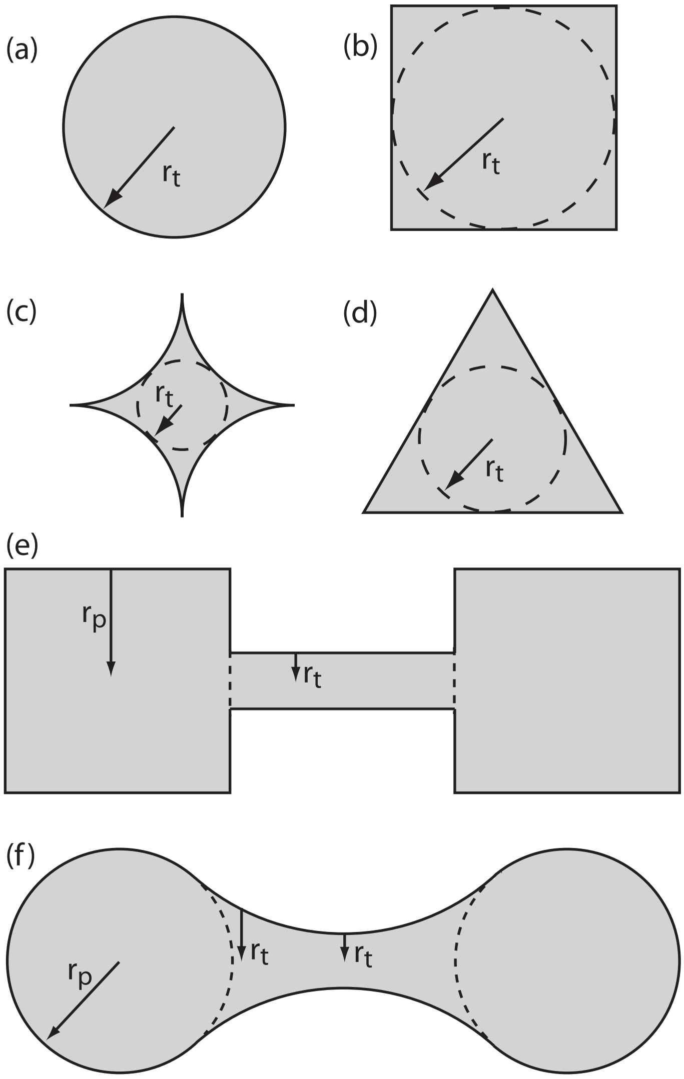

Figure 2.5: Popular pore shapes used in network modelling studies include circular (a), square (b), star shaped (c) and triangular (d). The throats can either have a constant radius (e) or vary smoothly (f).

When using networks based on reconstructed sandstones one would like to relate the individual pore shape to that observed in the reconstructed medium, which one cannot do when using a single cross-sectional shape. Since the real pore space is highly irregular it is not feasible to reproduce it exactly, but one can still include the measured quantities (cross-sectional area, radius and perimeter length) through the use of a dimensionless shape factor G, as suggested by Mason and Morrow [1991]. This is defined as the average cross-sectional area divided by the perimeter squared. Once the shape factor has been measured on the reconstructed medium an equivalent (in terms of G) irregular triangle can be defined, where G varies from 0 for a slit-shaped pore to $\sqrt{3}/36$ for an equilateral triangle. A highly irregular pore will thus have a low shape factor, resulting in the equivalent triangle having sharp corners, with more wetting fluid retained and higher conductivity in the wetting layers. A further advantage of this approach is that not only will it correct for layer volume and conductivity, but calculated capillary entry pressure will now be a direct function of the pore shape using expressions derived by several authors [*Mason and Morrow*, 1991; *Ma et al.*, 1996; *Øren et al.*, 1998]. In the few cases where pore shapes are in fact quite regular in the reconstructed medium one can use other equivalent pore shapes like squares ($G = 1/16$) or circles ($G = 1/4\pi$). It is assumed that the wetting fluid residing in corners is connected to those of adjacent pores and throats, with the result that the wetting fluid generally spans the entire network (excluding possible elements with circular cross-section). This is the approach used by Øren *et al.* [1998], Patzek [2001] and will also be followed by the work presented here.

2.4 Wettability effects

The wetting condition of the porous medium is of great importance in defining the flow characteristics. The oil-water contact angle θ_{ow} is defined as the angle of contact of oil and water on a solid surface measured through the denser (water) phase, as illustrated in Figure 2.6 (a). Three broad classifications can be identified – water-wet, oil-wet or intermediate-wet, where the contact angles are less than 90°, greater than 90° or close to 90°, respectively. A combination of these wetting conditions is also possible. I will refer to this latter condition as mixed-wet – most hydrocarbon bearing reservoirs are found to fall into this category [*Anderson*, 1986a].

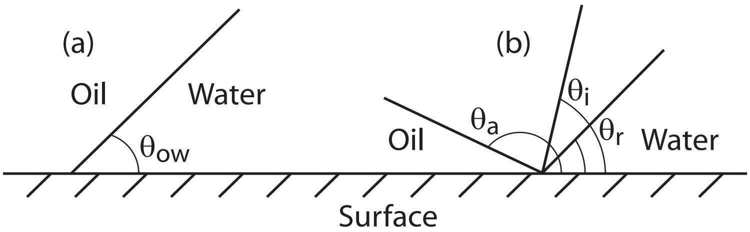

Figure 2.6: (a) The oil-water contact angle θ_{ow} is measured through the denser phase (water). (b) On rough surfaces the advancing contact angle θ_a (increase in water saturation) is typically found to be significantly larger than the receding contact angle θ_r (reduction in water saturation). The intrinsic contact angle θ_i is that measured at rest on a smooth surface [*Morrow*, 1975].

Consider that initially the rock is water-saturated and strongly water-wet. Following primary oil flooding it is assumed that the part of the rock in direct contact with hydrocarbon will alter its wettability, whereas the crevices and small throats still containing water will remain strongly water-wet. Initially a thin water film protects the pore walls from the asphaltenes in the oil that can make the pore walls become oil-wet [*Kovscek et al.*, 1993]. In some pores this film might collapse, allowing the pore to become oil-wet. Some wettability alteration might still occur in pores where the film remains as a result of asphaltenes diffusing across the water film [*Kaminsky and Radke*, 1997]. The rock might therefore end up with three distinctively different simultaneous wetting populations – strongly water-wet where oil has not invaded, strongly oil-wet where the water films have collapsed and intermediate-wet where the films remain. This type of wetting condition has indeed been observed experimentally [*Masalmeh*, 2003]. The same wettability state is likely to occur in groundwater situations where non-aqueous phase liquids have been in contact with the soil for many months or years.

In addition to wettability alteration, contact angles are affected by the direction of flow. Due to surface roughness, advancing contact angles θ_a (increase in water saturation) are typically found to be significantly larger than receding contact angles θ_r (reduction in water saturation), Figure 2.6 (b). Morrow [1975] developed several models for this contact angle hysteresis by measuring both advancing and receding angles in a number of smooth and roughened Teflon tubes and relating these to the intrinsic contact angle as measured at rest on a smooth surface. Although one would expect to see no difference between advancing and receding contact angles in completely smooth tubes (referred to as Class I model), some hysteresis was observed (Class II model). Morrow explained this by minor inaccuracies in the tube manufacturing process. Following roughening of the tubes, substantially more hysteresis was observed (Class III model). The amount of hysteresis experienced in real porous media is still, however, highly uncertain due to the difficulty of measuring and classifying results from non-ideal systems where both mineralogy and fluid composition can have large influences [*Buckley et al.*, 1998]. Xie *et al.* [2002] measured both advancing and receding contact angles on a quartz surface during repeated flooding cycles. The receding contact angle was generally found to remain stable. Depending on which of the 10 crude oil samples were used, the advancing contact angle was found to either remain stable (four crude oils) or decrease somewhat with flooding cycle. The amount of hysteresis was generally found to be between 40 and 70 degrees, somewhat less than the Class III model but considerably more than the Class II model, as suggested by Morrow [1975].

The flow behaviour when large parts of the rock surface are strongly oil-wet is found to be significantly different from intermediate and water-wet conditions. Salathiel [1973] conducted flooding experiments on a range of cores with different wettability. He found that oil production continued long after initial water breakthrough in mixed-wet cores with very low residual oil saturation obtained as a result. However, a very large number of injected pore volumes of water were needed to achieve these low saturations. Salathiel suggested that oil escaped through connected layers that could exist in strongly oil-wet pores. Kovscek *et al.* [1993] suggested this behaviour could be captured in network models using the above-mentioned star shaped network elements. Following drainage only the part of the pore wall in direct contact with oil would become oil-wet with the corners remaining water-wet. The oil-water interface in the corners would initially remain pinned during water flooding, allowing oil layers to become sandwiched between water in the corners and that in the centre. With this pore level scenario he was able to reproduce the experimental trends observed by Salathiel.

From Amott core-flood tests and nuclear magnetic resonance (NMR) it is possible to obtain a bulk indication of the wettability [*Anderson*, 1986b]. How the mixed wettability is distributed on the pore-scale is, however, much more difficult to evaluate. Kovscek *et al.* [1993] proposed a theoretical model where the smaller pores become oil-wet while the larger ones remain water-wet. Using cryo- and environmental scanning electron microscopy it is possible to visualize directly the distribution of fluids at the pore-scale [*Fassi-Fihri et al.*, 1991; *Combes et al.*, 1998; *Durand and Rosenberg*, 1998]. These studies suggested that the distribution of clay, in particular kaolinite, plays a very important role in determining what parts of the rock becomes oil-wet.

The impact of wettability on relative permeability has been extensively studied using pore-scale network modelling. McDougall and Sorbie [1995; 1997] investigated trends in relative permeability as well as recovery efficiency. Even with a fairly simple network model that didn’t explicitly include wetting layers they were able to predict trends in recovery that indicated that optimum recovery would be obtained with about half the pore space being oil-wet, something that had been previously observed experimentally [*Jadhunandan and Morrow*, 1995].

Dixit *et al.* [1998; 1999; 2000] used the same simple network model as McDougall and Sorbie [1995] to introduce a wettability classification system, relating recovery from mixed-wet systems to aging and fraction of oil-wet pores. They also developed analytical expressions relating different wettability indices to different mixed-wetting scenarios and compared these to network modelling predictions [2000]. It was suggested that if experimental capillary pressures were available for different flooding cycles, it should be possible to determine whether oil-wet pores were correlated to pore size or just randomly distributed.

Blunt [1997b; 1998] used square elements for both pores and throats. This allowed him to explicitly model wetting layers and from simple geometrical considerations develop capillary pressure expressions for the different filling events described by Lenormand *et al.* [1983]. In each element multiple wetting conditions were allowed to exist, with the corners remaining water-wet while the centre becoming oil-wet in a similar approach to that of Kovscek *et al.* [1993]. The effects on relative permeability from a wide range of wetting conditions were investigated and although the main conclusions were the same as those reached using simpler network models [*Dixit et al.*, 1997; *McDougall and Sorbie*, 1997; *Dixit et al.*, 1998] an improved understanding of strongly oil-wet systems was made possible.

Only very limited mixed-wet experimental relative permeability data have been predicted using pore-scale network modelling. Only recently when combining geologically realistic networks with improved understanding of pore level physics have some promising results been shown by Øren *et al.* [1998] who predicted relative permeability for a water-wet Bentheimer sandstone and for a mixed-wet reservoir sandstone. Jadhunandan and Morrow [1995] measured oil recovery from a series of Berea cores. Mixed-wetting conditions where achieved primarily by varying the initial water saturation. Maximum recovery was achieved in cores where the Amott wettability index was close to zero, corresponding to intermediate initial water saturations. Using geologically realistic networks from reconstructed samples of Berea sandstone both the trend [*Jackson et al.*, 2003] and a quantitative match [*Øren and Bakke*, 2003] with experimental recoveries have been predicted. Jackson *et al.* [2003] assumed that all invaded pores following primary drainage become oil-wet. The experimentally measured wettability indices were then matched by varying the distribution of oil-water contact angles. We will pursue a similar but more thorough approach in this thesis. Øren and Bakke [2003] introduced a method for estimating the oil-wet fraction and contact angle distributions using the measured wettability indices. They were able to obtain a quantitative match with experiments using several different schemes for selecting the oil-wet pores.

2.5 Discussion

Pore-scale network modelling has been an active field of research for more than two decades. However, its main application has been constricted to better understanding pore-scale physics and explaining general displacement trends rather than a tool to predict the flow behaviour of a specific porous medium. The reason for this is simple: flow in real porous media is a complex problem. A pore-scale network model with predictive capabilities will need to carefully address both the statistical and topological properties of the porous medium, the physics of fluid transport at the pore-scale, and wettability characterization. Recent advances in these three areas have thus been the focus of this literature survey.

It seems clear that using a regular lattice structure to represent real porous media is not feasible if the network model is to have predictive capabilities. Even when mapping most of the morphological properties of a sandstone onto the lattice Sok *et al.* [2002] were unable to satisfactorily predict the transport properties of the sandstone. Another approach used in conjunction with regular lattices is to use easily obtainable macroscopic properties such as experimental capillary pressure to populate the properties of the lattice. This is then used to predict other macroscopic properties like relative permeability that are more difficult to obtain experimentally. Though Fischer and Celia [1999] managed to predict relative permeability for individual flooding cycles quite well, they were unable to predict hysteresis trends between different cycles. The experimental data they tried to predict will in fact be revisited in Chapter 4 of this thesis.

One approach that has shown itself to be successful in predicting experimental transport properties is that pioneered by Øren and co-workers at Statoil [1997; 1998; 2002]. By obtaining the lattice structure directly from a voxel-based representation of the porous media they are able to capture both the relevant statistical and topological properties of the media. Combining this with a network model that is able to model all the relevant pore-scale physics has progressed network modelling to the stage where it now can be used to reliably predict transport properties of real systems. This approach will indeed be followed in this thesis. However, there are still remaining issues, some of which will be addressed in this work. The approach as presented by Øren *et al.* assumes that lattice and subsequent flow predictions are specific to the properties of the porous medium used in the voxel-based reconstruction. I will present in Chapter 4 a methodology for combining realistic networks, originally constructed to represent one particular porous medium, with conditioning to easily obtainable experimental data to predict flow properties of a variety of different porous media.

Predictive pore-scale modelling of systems with complex wetting behaviour is something that is almost completely absent from the literature. One reason for this is the high degree of uncertainty relating to the characterization of mixed wettability on the pore-scale. Relatively simple theoretically based scenarios for mixed wetting [*Kovscek et al.*, 1993] are found to inadequately describe real systems [*Durand and Rosenberg*, 1998]. However, if some degree of confidence can be attached to the basics of the pore-scale network model, i.e. lattice properties and implemented pore-scale physics, valuable insight into the displacement process can be achieved by comparing experimental data to network model predictions [*Jackson et al.*, 2003; *Øren and Bakke*, 2003]. This is something that will be investigated in further detail in Chapter 5.

Chapter 3

Network Model

In this section we will outline the mathematical details and assumptions made when simulating multiphase flow in network models. This broadly follows the work of Øren *et al.* [1998], Patzek [2001] and Al-Futaisi and Patzek [2003]. The most basic assumption made is that the flow is capillary dominated (quasi-static) with the viscous pressure drop in the model being insignificant in comparison to the capillary pressure. The capillary number N_{cap} (ratio of viscous to capillary forces) should be less than 10^{-4} [*Blunt and Scher*, 1995], as defined by

$$N_{cap} = \frac{\mu v}{\sigma}, \tag{3.1}$$

where μ is viscosity, σ is interfacial tension and v is fluid velocity. What this means in practice is that all interfaces are kept static throughout the network with the exception of a single displacement event.

We will refer to the initial wetting phase as water and the non-wetting phase as oil (unless experimental data is based on other fluids). Also, since mixed-wet systems make the terms drainage (non-wetting phase invasion) and imbibition (wetting-phase invasion) ambiguous, we will refer to these processes as oil and water flooding, respectively.

3.1 Description of the pore space

A 3D voxel representation of Berea sandstone is the basis for the networks used in this paper, Figure 1. A topologically equivalent network of pores and throats is then generated with properties (radius, volume, *etc*) extracted from the original voxel representation.

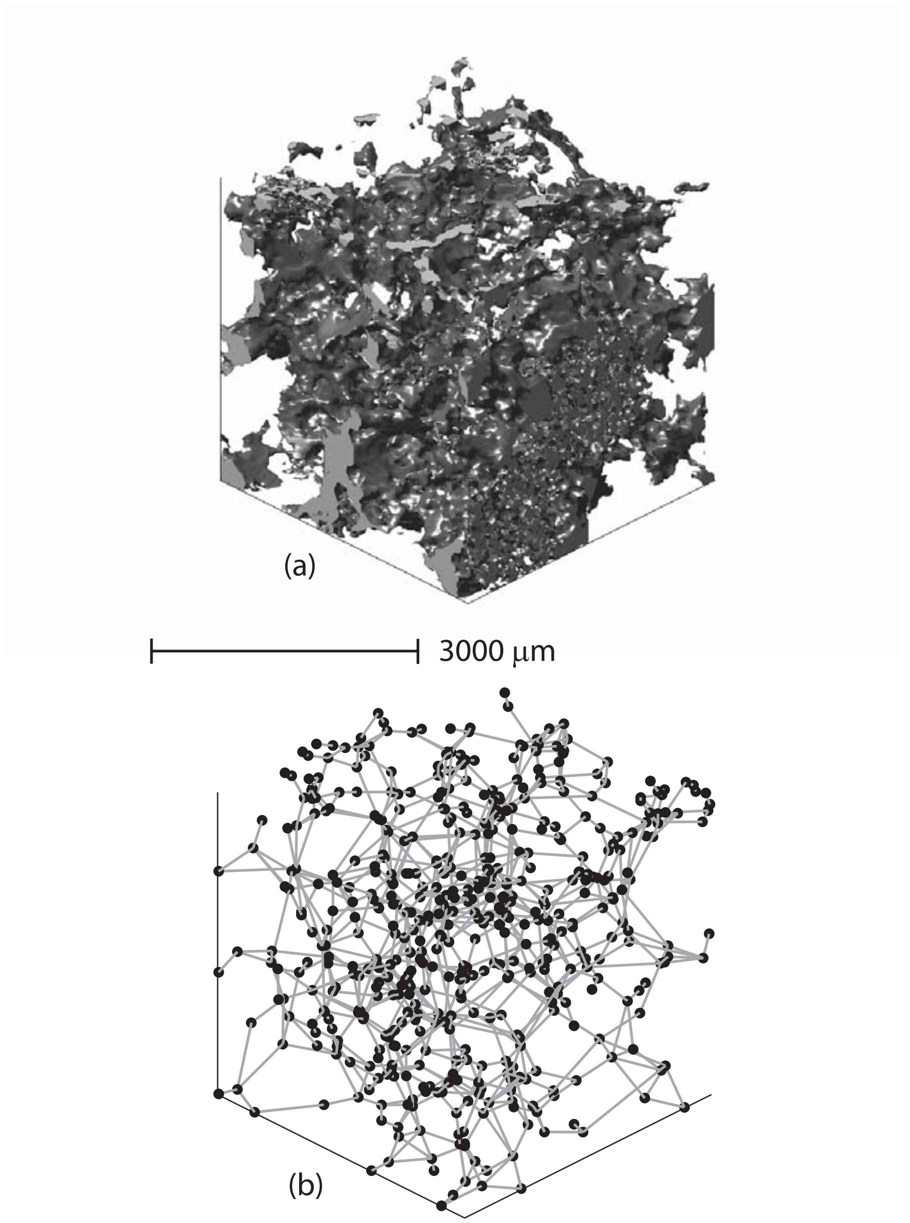

Figure 3.1: (a) 3D image of a sandstone along with (b) a topologically equivalent network representation [*Bakke and Øren*, 1997].

The individual network elements are uniform ducts with circular, triangular or square cross-sectional shapes. These have the same shape factor [*Mason and Morrow*, 1991], $G = A/P^2$, as the voxel representation, where A is the cross-sectional area and P the perimeter length, as illustrated in Figure 3.2. In the voxel representation these are average values recorded along the throat and at the pore centre. As the pore space becomes more irregular the shape factor decreases. A circle and a square have shape factors of 1/16 and $1/4\pi$, respectively. For a triangle the shape factor will range from zero for a slit shaped triangle to 3/36 for an equilateral triangle.

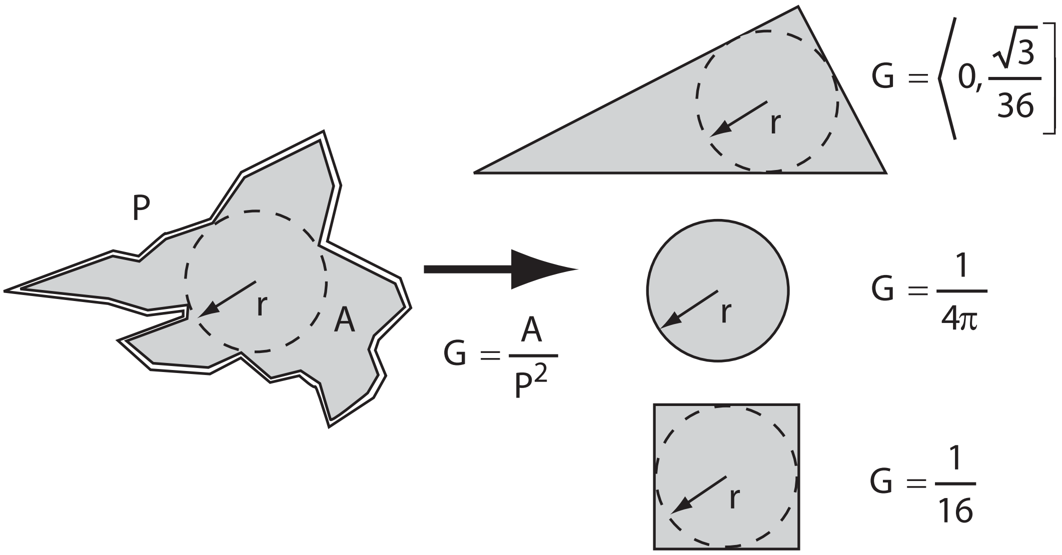

Figure 3.2: The network elements (triangular, circular or square cross-section) have the same shape factor [*Mason and Morrow*, 1991] as that measured on the irregular voxel representation.

For a given shape factor the corner half angles β can take on a range of values where $\beta_1 \leq \beta_2 \leq \beta_3$. First β_2 is chosen randomly within the allowed range

$$\beta_{2,min} = \operatorname{atan}\left\{\frac{2}{\sqrt{3}}\cos\left[\frac{\operatorname{acos}\left(-12\sqrt{3}G\right)}{3} + \frac{4\pi}{3}\right]\right\} \tag{3.2}$$

and

$$\beta_{2,max} = \operatorname{atan}\left\{\frac{2}{\sqrt{3}}\cos\left[\frac{\operatorname{acos}\left(-12\sqrt{3}G\right)}{3}\right]\right\}, \tag{3.3}$$

with β_1 subsequently given by

$$\beta_1 = -\frac{1}{2}\beta_2 + \frac{1}{2}\operatorname{asin}\left(\frac{\tan\beta_2 + 4G}{\tan\beta_2 - 4G}\right), \tag{3.4}$$

and finally $\beta_3 = \pi/2 - \beta_1 - \beta_2$ [*Patzek*, 2001]. Compared to the voxel image the network elements are obviously only idealized representations. However, by maintaining the measured shape factor a quantitative measure of the irregular pore space is maintained. Fairly smooth pores with high shape factors will be represented by network elements with circular cross-sections, whereas more irregular pore shapes will be represented by triangular cross-sections, possibly with very sharp corners.

Using square or triangular shaped network elements allows for the explicit modelling of wetting layers (water or oil depending on the wetting state), whereby non-wetting phase occupies the centre of the element and wetting phase remains in the corners. The pore space in real rock is highly irregular with water remaining in grooves and crevices after primary oil flooding, due to capillary forces. This behaviour has been observed in micromodel experiments where flow channels typically have a square cross-section [*Lenormand et al.*, 1983]. The wetting layers might not be more than a few microns in thickness, with little effect on the overall saturation or flow. Their contribution to wetting phase connectivity is, however, of vital importance, ensuring low residual wetting phase saturation by preventing trapping.

Micro-porosity and water saturated clays will typically not be drained during core analysis. Rather than explicitly including this in the network representation, a constant clay volume that remains water-filled is associated with each element.

3.2 Primary oil flooding

Since all the elements (pores and throats) in the network model initially only contain water, displacement can only occur through piston-like displacement whereby the centre of an element can only be filled if it has an adjacent element containing oil. The capillary pressure required for the oil meniscus to invade a water-filled element is given by the Young-Laplace equation

$$P_{cow} = P_o - P_w = \sigma_{ow}\left(\frac{1}{R_1} + \frac{1}{R_2}\right), \tag{3.5}$$

where σ_{ow} is the oil-water interfacial tension and R_1 and R_2 are the principal radii of curvature of the interface. When we know the shape of the pore and the contact angle at which the interface hits the solid surface we can use expressions that are easier to evaluate. For a circular pore it is simply

$$P_{cow} = \frac{2\sigma_{ow}\cos\theta_{owr}}{r}, \tag{3.6}$$

where θ_{owr} is the receding oil-water contact angle and r is the inscribed radius [*Dullien*, 1992]. Gravity effects can be included easily by subtracting $\Delta\rho_{ow}gh$ from the capillary entry pressure expressions, where $\Delta\rho_{ow}$ is the density difference between oil and water, g is the gravitational constant and h is the height above datum of the element. For the remaining part of this thesis I will omit the oil-water subscript.

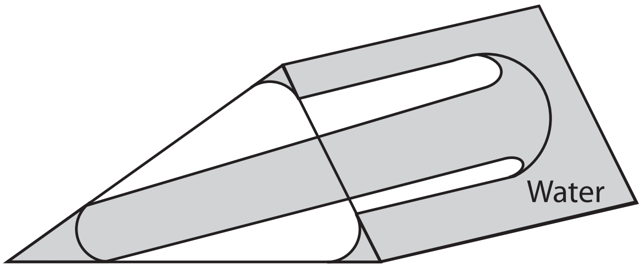

Figure 3.3: View of oil (transparent) displacing water in a triangular duct during piston-like displacement.

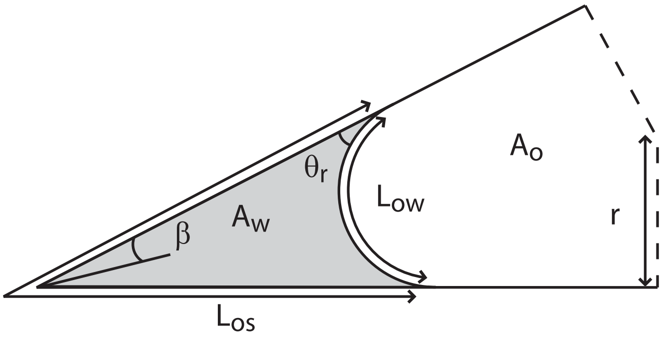

Figure 3.4: Cross-sectional view of a single corner in a polygonal shaped element.

Only a very small fraction of network elements will have a circular cross-section. For polygonal shaped elements the capillary entry pressure expressions become complex as the wetting fluid remains in the corners as arc menisci (AMs). Entry pressures are found by calculating the force balance acting on the interface in the duct, as illustrated in Figure 3.3. This method has become known as the Mayer, Stowe and Princen (MS-P) method [*Mason and Morrow*, 1991] and we follow Øren *et al.*'s [1998] generalization of it, given by

$$P_c = \frac{\sigma \cos\theta_r \left(1 + 2\sqrt{\pi G}\right)}{r} F_d(\theta_r, G, \beta), \tag{3.7}$$

where F_d is a dimensionless correction factor for wetting fluid that might be retained in the corners. For a polygonal shaped element, for which one corner is shown in Figure 3.4, it can be calculated by considering a small displacement *dx* of the AM. This must be balanced by the change in surface free energy,

$$P_c A_{eff} = \left(L_{ow}\sigma_{ow} + L_{os}\sigma_{os} + L_{os}\sigma_{ws}\right)\mathrm{d}x\ , \tag{3.8}$$

where A_{eff} is effective area occupied by oil, L_{os} is the length of the oil-surface interface and L_{ow} is the length of the oil-water interface. A horizontal force balance gives the Young equation,

$$\sigma_{os} = \sigma_{ws} + \sigma_{ow}\cos\theta_{owr}\ , \tag{3.9}$$

that allows us to simplify (3.8),

$$\frac{P_c}{\sigma_{ow}} = \frac{1}{R} = \frac{L_{ow} + L_{os}\cos\theta_{owr}}{A_{eff}}\ , \tag{3.10}$$

where R is the radius of curvature. The interface lengths can be determined from elementary geometry,

$$A_{eff} = A - R^2 \sum_{i=1}^{n} \left[\frac{\cos\theta_{\mathrm{r}}\cos(\theta_r + \beta_i)}{\sin\beta_i} + \theta_r + \beta_i - \frac{\pi}{2}\right] = \frac{r^2}{4G} - R^2 S_1\ , \tag{3.11}$$

$$L_{os} = \frac{r}{2G} - 2R\sum_{i=1}^{n} \frac{\cos(\theta_r + \beta_i)}{\sin\beta_i} = \frac{r}{2G} - 2RS_2, \tag{3.12}$$

$$L_{ow} = 2R\sum_{i=1}^{n}\left(\frac{\pi}{2} - \theta_r - \beta_i\right) = RS_3\ , \tag{3.13}$$

where n is the total number of corners containing AM's ($\beta < \pi/2 - \theta_r$) and $A = r^2 / (4G)$ is the total polygon area. A quadratic expression for the curvature radius is then given by,

$$R = \frac{r\cos\theta_r\left(-1 \pm \sqrt{1 + \dfrac{4GD}{\cos^2\theta_r}}\right)}{4GD}\ , \tag{3.14}$$

$$D = S_1 - 2S_2\cos\theta_r + S_3\ . \tag{3.15}$$

The sign in (3.14) must be chosen so that the curvature radius that is less than the inscribed radius. The dimensionless correction factor in (3.7) is therefore given by

$$F_d(\theta_r, G, \beta) = \frac{1 + \sqrt{1 + \dfrac{4GD}{\cos^2\theta_r}}}{\left(1 + 2\sqrt{\pi G}\right)} \, . \tag{3.16}$$

In the case of a circular tube where there are no corners, F_d will be 1 and (3.7) will simplify to (3.6).

The throats along the inlet face of the network model are all assumed to be connected to a reservoir of oil. The pressure in the oil phase P_o is then increased while the water phase pressure P_w is kept constant throughout the network, resulting in increased capillary pressure P_c. The elements are filled in order of increasing capillary entry pressure (assuming they have an oil-filled neighbour). This process continues until some predefined saturation is reached, or all elements have been filled by oil. Once a polygonal element has been filled by oil, water still remains in the corners. This will ensure that water, as the wetting phase, will remain connected throughout primary oil flooding, since escape to the outlet is always possible through wetting layers.

3.3 Secondary water flooding

The part of the rock in direct contact with oil will have its wettability altered following primary oil flooding, whereas the corners and elements still only containing water will remain strongly water-wet, Figure 3.5. In addition to wettability alteration, contact angles are affected by the direction of flow due to surface roughness. Contact angle hysteresis between the flooding cycles is thus modelled using the Class III model suggested by Morrow [1975]. By defining a distribution of intrinsic contact angles, the receding θ_r (reduction in water saturation) and advancing θ_a (increase in water saturation) values can be found using the relationship illustrated in Figure 3.6.

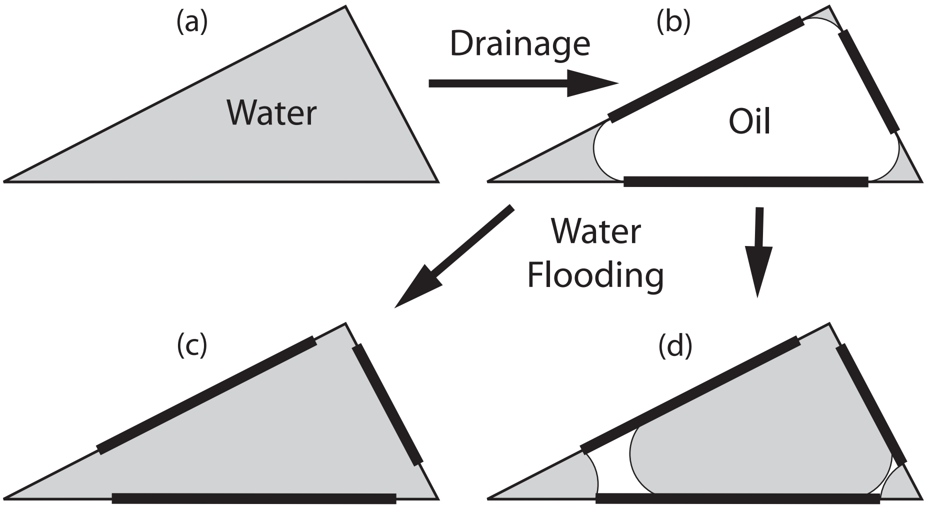

Figure 3.5: Possible fluid configurations. (a) Initially the element is water-filled and strongly water-wet. (b) Following primary oil flooding the part of the element in contact with oil will alter its wettability. (c) During water flooding the element might again become completely water-filled. (d) If wettability alteration was large enough, oil might become sandwiched as a layer between water in the corner and the centre.

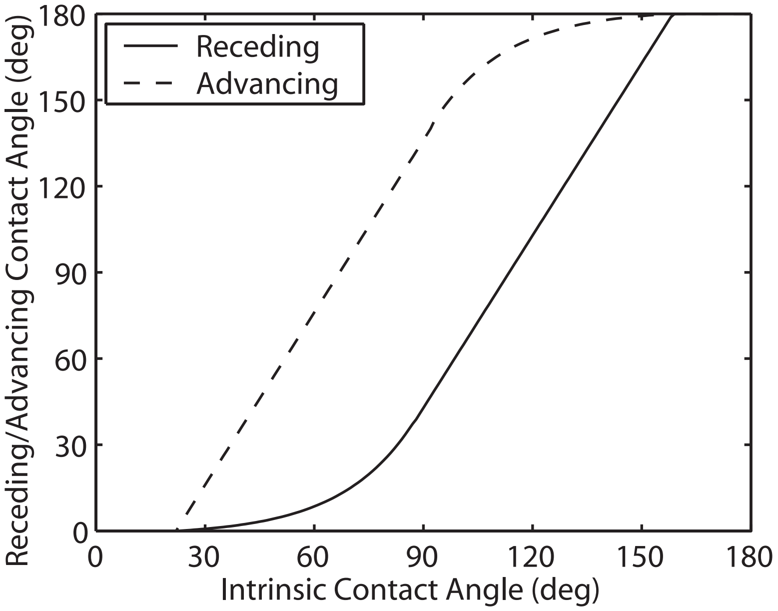

Figure 3.6: Relationship between receding and advancing contact angles on a rough surface, as a function of intrinsic contact angle measured at rest on a smooth surface [*Morrow*, 1975].

With wettability alteration and water in corners the mechanisms by which water can displace oil become more complex [*Lenormand et al.*, 1983]. The three main processes are piston-like displacement, pore body filling and snap-off.

3.3.1 Piston-like displacement

As the capillary pressure drops, the oil-water interface in corner i will initially remain pinned at the last position b_i obtained during primary oil flooding, Figure 3.7 (a).

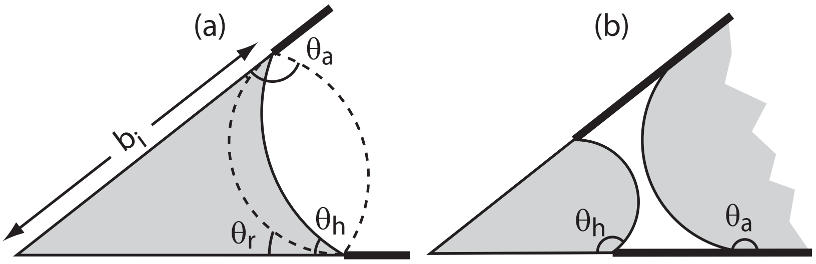

Figure 3.7: Fluid configurations in corners. (a) A pinned interface hinges between receding and advancing contact angles. (b) Oil might become sandwiched between water in corners and water in the centre.

In order to maintain capillary equilibrium, the contact angle $\theta_{h,i}$ will hinge at this position in order to maintain capillary equilibrium. Therefore,

$$b_i = R_{min} \frac{\cos(\theta_r + \beta_i)}{\sin\beta_i}, \tag{3.17}$$

$$\theta_{h,i} = \operatorname{acos}\left(\frac{b_i \sin\beta_i}{R}\right) - \beta_i , \tag{3.18}$$

where $R = \sigma / P_c$ is the radius of curvature and R_{min} is the smallest radius of curvature obtained during primary oil flooding. Only when reaching the advancing contact angle θ_a will the interface start to move along the pore surface. During spontaneous (positive capillary pressure) piston-like displacement the capillary entry pressure is again found by calculating the force balance acting on the interface. Since the hinging contact angle is a function of capillary pressure, the following equations are solved iteratively to obtain the solution for the curvature radius corresponding to the capillary entry pressure:

$$R = \frac{A_{eff}}{L_{ow} + L_{os}\cos\theta_a}, \tag{3.19}$$

$$A_{eff} = A - R^2 \sum_{i=1}^{n} \left[\frac{\cos\theta_{h,i} \cos(\theta_{h,i} + \beta_i)}{\sin\beta_i} + \theta_{h,i} + \beta_i - \frac{\pi}{2} \right], \tag{3.20}$$

$$L_{os} = \frac{r}{2G} - 2 \sum_{i=1}^{n} b_i, \tag{3.21}$$

$$L_{ow} = 2R \sum_{i=1}^{n} \operatorname{asin}\left(\frac{b_i \sin\beta_i}{R} \right). \tag{3.22}$$

If the hinging contact angles have all reached the limiting advancing value, the expression for the capillary entry pressure will be the same as that during primary oil flooding with the receding contact angle replaced by the advancing one. In the case where one or more of the interfaces have reached the advancing contact angle the expression for b_i (3.17) is simply replaced by

$$b_i = R \frac{\cos(\theta_a + \beta_i)}{\sin\beta_i}. \tag{3.23}$$

From these expressions it is clear that spontaneous displacement might occur for advancing contact angles greater than 90°, with the maximum angle given by

$$\cos\theta_{a,max} \approx \frac{-4G \sum_{i=1}^{n} \cos(\theta_r + \beta_i)}{\frac{r}{R_{min}} - \cos\theta_r + 12G\sin\theta_r}. \tag{3.24}$$

During forced water invasion (negative capillary pressure) the absolute entry pressure is simply given by (3.7) with θ_r replaced by $\pi - \theta_a$.

3.3.2 Pore body filling

The capillary entry pressure for filling a pore body during spontaneous water flooding is limited by the largest radius of curvature that can be achieved. This will depend on the number of adjacent oil-filled throats [*Lenormand et al.*, 1983], as shown in Figure 3.8.

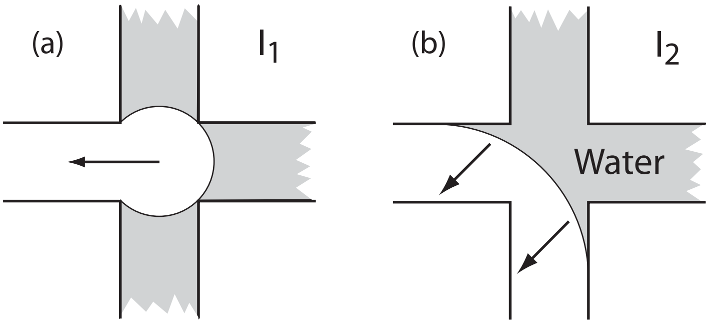

Figure 3.8: Pore body filling processes. The capillary entry pressure will be lower when several connecting throats (b) are filled with oil compared to when only a single throat is oil-filled (a).

A pore body with coordination number z can thus be filled by $z - 1$ possible events, I_1 to I_{z-1}, each occurring at a separate capillary pressure. If only a single adjacent throat is filled with oil (I_1 mechanism) the process is similar to piston-like displacement, with the entry pressure found using the approach outlined in the previous section. Since the exact spatial location of the oil-filled throats is difficult to estimate, it is common to express the capillary entry pressure as a parametric model [*Blunt*, 1998]:

$$P_c = \frac{2\sigma\cos\theta_a}{r} - \sigma\sum_{i=1}^{n} A_i x_i \, , \tag{3.25}$$

where n is the number of connecting oil-filled throats, A_i are arbitrary numbers and x_i are random numbers between zero and one. Since A_i have dimensions of m^{-1} we chose to relate it to permeability,

$$A_2 \text{ - } A_n = \frac{0.03}{\sqrt{K}} \, , \tag{3.26}$$

where the permeability K is measured in m^2. This approximately reproduces the results by Blunt [1998]. When only one connecting throat contains oil (I_1 event) the process is similar to piston-like displacement and hence $A_1 = 0.0$ μm^{-1}. This is also the most favoured event. During forced water invasion the capillary entry pressure is not dependent on the number of adjacent oil-filled throats and the filling process is again similar to piston-like displacement.

The choice of weights will clearly have an impact on what type of displacement will be most favoured. Larger weights will reduce the capillary entry pressure when the pore body is surrounded by multiple oil-filled throats, making other displacement events, like snap-off, more favourable. This effect will be similar to that achieved by having a smaller advancing contact angle or a larger size aspect ratio between pore bodies and throats, both of which make snap-off more likely to occur compared to pore body filling.

3.3.3 Snap-off

In snap-off an element is filled with water as the result of corner water layers swelling so much that the fluid/fluid interface becomes unstable. Snap-off will only occur if there is no adjacent element whose centre is filled with water. If $\theta_a < \pi/2 - \beta_1$ the arc menisci will advance smoothly along the pore wall once θ_a has been reached. Once two menisci meet, there no longer is an oil-water-solid contact, resulting in the oil-water interface becoming unstable with spontaneous water filling as the result, as shown in Figure 3.9 (a). The capillary pressure at which this occurs depends on whether one or several menisci have started to advance along the pore wall. If two or more menisci have started to move, the menisci in the sharpest corners will meet at a capillary pressure

$$P_c = \frac{\sigma}{r}\left(\cos\theta_a - \frac{2\sin\theta_a}{\cot\beta_1 + \cot\beta_2}\right), \tag{3.27}$$

whereas if only the meniscus in the sharpest corner has started to advance, it will meet the pinned meniscus in the most oblique corner at a capillary pressure

$$P_c = \frac{\sigma}{r}\left(\frac{\cos\theta_a\cot\beta_1 - \sin\theta_a + \cos\theta_{h,3}\cot\beta_3 - \sin\theta_{h,3}}{\cot\beta_1 + \cot\beta_2}\right). \tag{3.28}$$

The event with the highest capillary pressure will be the one that occurs.

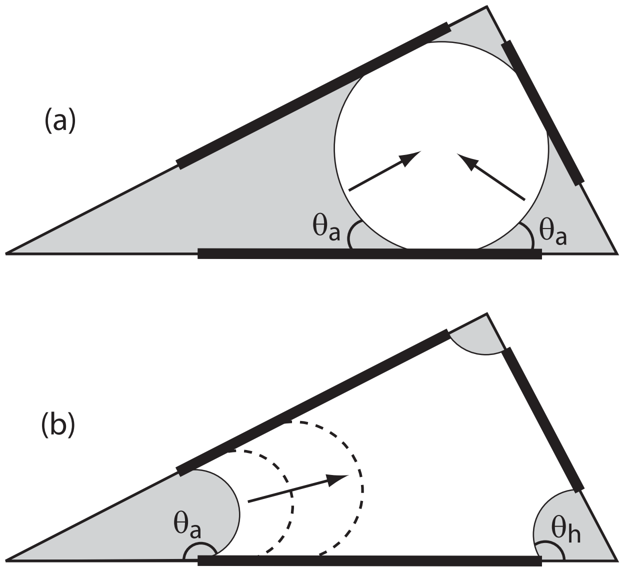

Figure 3.9: Snap-off events. (a) During spontaneous water injection snap-off will occur once water in corners meet along the pore wall. (b) During forced water injection snap-off will occur as soon as the advancing contact angle is reached.

During forced water invasion snap-off will occur as soon as $\theta_{h,1}$ has reached θ_a or $\theta_a - \beta_1$ in the case where $\theta_a > \pi - \beta_1$. Once the arc meniscus starts advancing along the pore wall, the absolute negative curvature will decrease, making it unstable with spontaneous filling as the result, Figure 3.9 (b), with the entry pressure given by

$$P_c = \frac{\sigma \cos(\theta_a + \beta_1)}{R_{min} \cos(\theta_r + \beta_1)} \qquad \theta_a \leq \pi - \beta_1 \tag{3.29}$$

or

$$P_c = \frac{-\sigma}{R_{min} \cos(\theta_r + \beta_1)} \qquad \theta_a > \pi - \beta_1. \tag{3.30}$$

Piston-like displacement is always favoured (occurring at a higher capillary pressure) to snap-off wherever piston-like displacement is topologically possible. Snap-off can, however, still be an extremely important displacement process as it does not require any adjacent elements being water-filled. Hence, it can occur anywhere where the oil is connected to the outlet.

3.3.4 Oil layers

When the water interface enters the element during forced invasion a layer of oil, Figure 3.7 (b), might become sandwiched between water in the corner and that in the centre if

$$\theta_a > \frac{\pi}{2} + \beta_i \,. \tag{3.31}$$

This can occur because the inner oil-water interface has a hinging contact angle that might be much less than the advancing contact angle associated with the outer interface. Stable oil layers can significantly increase recovery as they increase oil connectivity in much the same way that water layers influence primary oil flooding. The oil layer will collapse once the two interfaces meet, which if the capillary pressure is the same across the two interfaces, is given by the condition

$$P_c = \frac{\sigma \cos\left(\mathrm{acos}(2\sin\beta_i + \cos\theta_a) + \beta_i\right)}{b_i \sin\beta_i} \,. \tag{3.32}$$

3.3.5 Displacement process

At the beginning of water flooding the reservoir is at some given initial water saturation and capillary pressure. Water is then injected by increasing the water phase pressure, keeping the oil phase pressure constant through the outlet reservoir, resulting in a reduced capillary pressure. All possible displacement events are sorted in terms of capillary entry pressure, with the event with the highest capillary pressure executed first. The initial list of possible events is much bigger than it was during oil flooding. Not only are elements with adjacent water included, but also all possible snap-off events.

During primary oil flooding trapping was unimportant (though possible because oil-filled elements with a circular cross-section do not contain water layers) as water in corners ensured global connectivity, whereas during water flooding it becomes crucial. Once an element is filled from spontaneous invasion, it no longer conducts oil, since it is completely water-filled. Snap-off events, which typically occur in small throats, will reduce oil connectivity even further. Once a cluster of oil-filled elements becomes trapped it no longer is in pressure communication with the outlet. The capillary pressure within that cluster is frozen and the oil within it cannot be displaced. If the model is primarily oil-wet, trapping again becomes less important as the oil can escape through oil layers.

3.4 Subsequent flooding cycles

We assume that no further wettability alteration takes place following that occurring after primary oil flooding. Secondary oil flooding might thus become a spontaneous process. The possible displacement events occurring are the same as those described for water flooding. If oil layers are present we assume that the capillary entry pressure is only affected by the outer oil-water interface, which initially is pinned at the last position attained during water flooding. The entry pressure is calculated analogously to spontaneous piston-like water invasion. If no oil layers are present the entry pressure is simply given by (3.7) with $F_d = 1$. Oil snap-off is also possible as long as water and oil is not trapped.

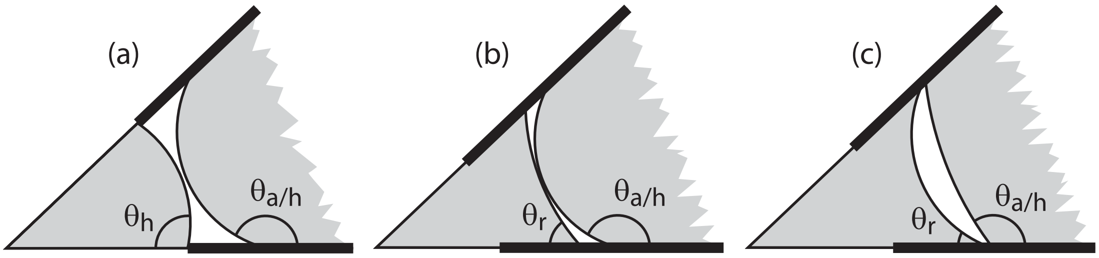

Figure 3.10: Possible layer configurations that might occur in network elements. (a) During secondary water flooding the layer will collapse once the two interfaces meet at the crest of the interface. (b) During higher order flooding cycles several more layer configurations are available. If water either in the centre or in the layers is trapped, the capillary pressure across the interfaces might not be equal. (c) Depending on the capillary pressures the layer might collapse as the interfaces meet at the base rather than at the crest.

If secondary water flooding progressed down to residual oil saturation, most oil layers will typically have collapsed, though we assume a molecular film of oil will remain. As the capillary pressure increases during secondary oil flooding these layers will reform if a neighbouring element contains non-trapped oil either in layers or in the centre. The capillary pressure at which this happens will depend on whether any of the water, either in the corners or in the centre, is trapped. If none is trapped the capillary pressure is given by (3.32) and we assume that the outer interface will subsequently hinge at the last position before the layer collapsed. If none of the water is trapped, but both the inner $\theta_{ih,j}$ and outer $\theta_{oh,j}$ contact angles for a given corner j are hinging, as depicted in Figure 3.10 (a), the collapsing capillary pressure can be found by iteratively solving the following equations:

$$\frac{\cos\theta_{ih,j} - \cos\theta_{oh,j}}{\sin\beta} = 2 \,, \tag{3.33}$$

$$\cos(\cos\theta_{ih,j} + \beta_j) = \frac{b_{i,j}\sin\beta_j}{R} \,, \tag{3.34}$$

$$\cos(\cos\theta_{oh,j} - \beta_j) = \frac{b_{o,j}\sin\beta_j}{R} , \tag{3.35}$$

where $b_{i,j}$ and $b_{o,j}$ are the pinned apex distances for the inner and outer interfaces.

If water in the corner is trapped, the inner interface has a constant radius of curvature R_i and inner hinging contact angle $\theta_{ih,j}$, fixed in position the moment water got trapped. If the outer interface is not hinging, the oil layer will collapse at a radius of curvature

$$R = \frac{R_i\,(\cos\theta_{ih,j} - \sin\beta_j)}{\cos\theta_a + \sin\beta_j} \,, \tag{3.36}$$

whereas if the outer interface is hinging, the radius of curvature can be found by iteratively solving (3.35) in combination with (3.36), replacing θ_a with $\theta_{oh,j}$.

Similarly, if water in the centre is trapped, the outer interface has a constant radius of curvature R_o. The collapsing radius of curvature is found iteratively by solving (3.34) in combination with,

$$R = \frac{R_o\,(\cos\theta_a + \sin\beta_j)}{\cos\theta_{ih,j} - \sin\beta_j} \,. \tag{3.37}$$

If outer interface in hinging, replace θ_a with $\theta_{oh,j}$.

In some cases the layer might collapse once the interfaces touch at the base rather than the crest of the interface, Figure 3.10 (c). This is possible if water in the corner is trapped with $\theta_{ih,j} < \pi - \theta_a$. The radius of curvature is then given by

$$R = \frac{b_{i,j}\sin\beta_j}{\cos(\theta_a - \beta_j)} \,. \tag{3.38}$$

3.5 Calculation of transport properties

Estimation of transport properties can be done at any point during the displacement. Saturation is calculated using the prevailing maximum in capillary pressure (or minimum in the case of water injection) to compute the radius of curvature of the fluid interfaces. It is assumed that fluid flow in each phase is independent of the other phase and that the network configuration, i.e. the location of all the fluid interfaces is frozen in place. The absolute permeability K of the network is found from Darcy's law,

$$K = \frac{\mu_p q_{tsp} L}{A(\Phi_{inlet} - \Phi_{outlet})}, \tag{3.39}$$

when the network is fully saturated with a single phase p of viscosity μ_p. The total single-phase flow rate q_{tsp} through the network is found by imposing a potential drop ($\Phi_{inlet} - \Phi_{outlet}$) across its length L, with A being the cross-sectional area of the model. Potential is defined as $\Phi = P - \rho_p gh$, where P is the pressure, ρ_p is the phase density, g is the gravitational constant and h is the height above datum. The relative permeability k_{rp} is then given by

$$k_{rp} = \frac{q_{\mathrm{tmp}}}{q_{tsp}}, \tag{3.40}$$

where q_{tmp} is the total flow rate of phase p in multiphase conditions with the same imposed pressure drop. The total flow rate is found by solving for the pressure everywhere, imposing mass conservation at every pore i,

$$\sum_{\mathrm{j}} q_{p,ij} = 0, \tag{3.41}$$

where j runs over all the throats connected to pore i. For this to be valid we must assume the flow to be incompressible and that the viscous pressure drops are insignificant compared to the capillary pressure. This is consistent with the previously stated assumptions about capillary dominance. The flow rate q_p between two pores i and j is given by

$$q_{p,ij} = \frac{g_{p,ij}}{L_{ij}}(\Phi_{p,i} - \Phi_{p,j}), \tag{3.42}$$

where g_p is the fluid conductance, L is the length between the pore centres and Φ_p is the phase potential. The conductance between two pore bodies $g_{p,ij}$ is taken to be the harmonic mean of each individual conductance,

$$\frac{L_{ij}}{g_{p,ij}} = \frac{L_i}{g_{p,i}} + \frac{L_t}{g_{p,t}} + \frac{L_j}{g_{p,j}}, \tag{3.43}$$

where t indicates the connecting throat. The pore body lengths, L_i and L_j, are the lengths from the pore-throat interface to the pore centre, as illustrated in Figure 3.11. A linear set of equations can be defined from (3.41) and (3.42) that can be solved in terms of pore pressures. This is done using an algebraic multigrid solver [*Ruge and Stueben*, 1987]. With the pressures known at either side of any cross-sectional plane within the network model, the total flow rate can be computed from (3.42). To prevent boundary effects influencing relative permeability predictions, only the last half of the network is used for these calculations.

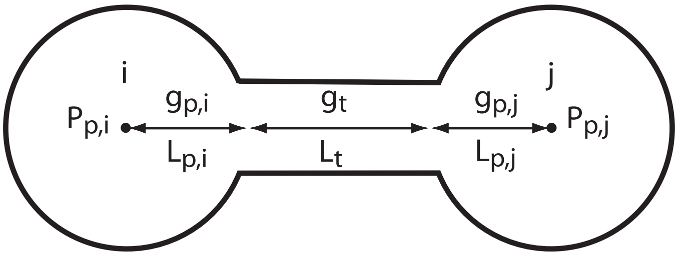

Figure 3.11: Conductance between two pores bodies *i* and *j*.

For single-phase laminar flow in a circular tube the conductance g_p is given analytically by the Hagen-Poiseuille formula,

$$g_p = k\frac{A^2G}{\mu_p} = \frac{1}{2}\frac{A^2G}{\mu_p}. \tag{3.44}$$

Analytical expressions for equilateral triangles and squares can also be developed [*Patzek and Silin*, 2001] with k being 3/5 and 0.5623 respectively. From numerical simulations Øren *et al.* [1998] found that the conductance for an irregular triangle was closely approximated by (3.44), using the same constant k as for an equilateral triangle, 3/5.

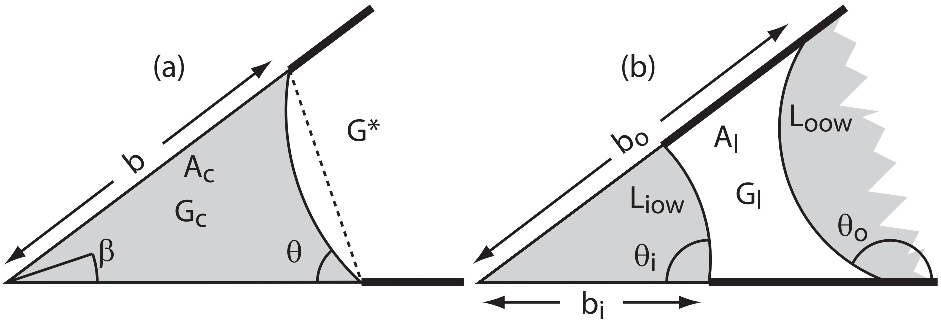

Figure 3.12: Corner configurations along with parameters affecting the shape. (a) Flow in a corner. (b) Flow in a layer.

In multiphase conditions an individual polygonal network element might contain both oil and water. Expressions for flow in element centres (where the corners contain a different phase) and flow in water and oil layers are all needed. These expressions are typically derived empirically from numerical simulations of flow in arbitrarily shaped ducts. For flow in the centre we continue to use (3.44) but multiply it by the fraction of the cross-section occupied by the phase in the centre, whereas flow in layers require separate expressions as the geometry becomes more complex. There are a number of variables affecting the shape of the corners and layers (Figure 3.12) − half angle β, contact angles θ and meniscus apex distances b. The boundary condition for the fluid interface is clearly very important. Here we assume infinite surface shear viscosity (no-slip boundary condition) which should be valid for a surfactant-laden water-oil interface.

3.5.1 Conductance of water layers

For flow in corners we use the correlation proposed by Øren *et al.* [1998], given by

$$A_c = \left(\frac{b_i \sin\beta}{\cos(\theta_i + \beta)}\right)^2 \left(\frac{\cos\theta_i \cos(\theta_i + \beta)}{\sin\beta} + \theta_i + \beta - \frac{\pi}{2}\right), \tag{3.45}$$

$$G_c = \frac{A_c}{4b_i^2\left(1 - \frac{\sin\beta}{\cos(\theta_i + \beta)}\left(\theta_i + \beta - \frac{\pi}{2}\right)\right)^2}, \tag{3.46}$$

$$G^* = \frac{\sin\beta \cos\beta}{4(1 + \sin\beta)^2}, \tag{3.47}$$

$$C = 0.364 + 0.28\frac{G^*}{G_c}, \tag{3.48}$$

$$g_{pc} = C\frac{A_c^2 G_c}{\mu_p}, \tag{3.49}$$

where G_c is the shape factor for the corner section containing the fluid, G^* is the shape factor without any curvature on the fluid interface and A_c is the corner area. The performance of the correlation was tested using a 2D finite element code for incompressible laminar flow. For a variety of corner configurations it was found to predict the conductance well within a ten percent error margin (Figure 3.13) with a mean absolute error of 4.9 percent. It was also found to compare favourably to correlations proposed by Patzek and Kristensen [2001] and Zhou *et al.* [1997].

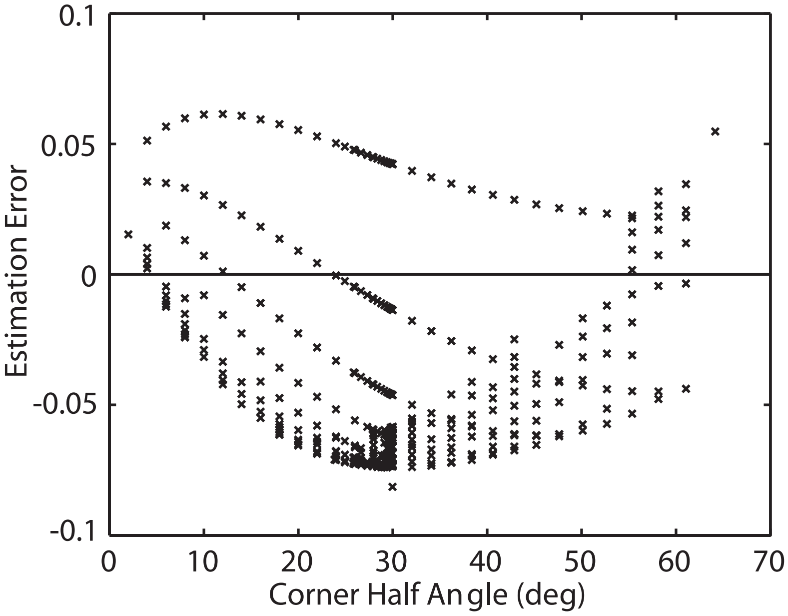

Figure 3.13: Performance of the layer conductance correlation suggested by Øren *et al.* [1998] when compared to numerical finite element simulations.

3.5.2 Conductance of oil layers

Predicting the conductance of oil layers is more difficult than water layers since there are two interfaces to include, Figure 3.12 (b). No correlation in the literature was found to adequately predict the hydraulic conductance. Numerical simulations, using a 2D finite element code for incompressible laminar flow (using an internal Statoil research code), were conducted, with the grid containing 4000 elements. 1035 different configurations were investigated, with the outer contact angle θ_o was varied between 120 and 180 degrees, the meniscus apex distance ratio between 0.01 and 0.6 and layer shape factor between 0.002 and 0.048, resulting in a variation of corner half angles from 3 to 62 degrees. Based on these simulations we suggest the following correlation:

$$\tilde{b}_i = \frac{b_i}{b_o}, \tag{3.50}$$

$$\tilde{A}_o = \left(\frac{\sin\beta}{\cos(\theta_o - \beta)}\right)^2 \left(\frac{\cos\theta_o \cos(\theta_o - \beta)}{\sin\beta} - \theta_o + \beta + \frac{\pi}{2}\right), \tag{3.51}$$

$$\tilde{A}_i = \left(\frac{\tilde{b}_i \sin\beta}{\cos(\theta_i + \beta)}\right)^2 \left(\frac{\cos\theta_i \cos(\theta_i + \beta)}{\sin\beta} + \theta_i + \beta - \frac{\pi}{2}\right), \tag{3.52}$$

$$\tilde{A}_l = \tilde{A}_o - \tilde{A}_i, \tag{3.53}$$

$$\tilde{L}_{oow} = \frac{2 \sin\beta}{\cos(\theta_o - \beta)} \left(\frac{\pi}{2} - \theta_o + \beta\right), \tag{3.54}$$

$$\tilde{L}_{iow} = \frac{2\tilde{b}_i \sin\beta}{\cos(\theta_i + \beta)} \left(\frac{\pi}{2} - \theta_i - \beta\right), \tag{3.55}$$

$$G_l = \frac{\tilde{A}_l}{\left(\tilde{L}_{oow} + \tilde{L}_{iow} + 2\,(1 - \tilde{b}_i)\right)^2}, \tag{3.56}$$

$$\ln \tilde{g}_l = a_1 \ln^2(\tilde{A}_l^3 G_l) + a_2 \ln(\tilde{A}_l^3 G_l) + a_3, \tag{3.57}$$

$$g_{pl} = \frac{b_o^4 \tilde{g}_l}{\mu_p}, \tag{3.58}$$

where $\tilde{A}_l$ is the dimensionless area of the layer, $\tilde{A}_o$ and $\tilde{A}_i$ are the outer and inner dimensionless corner areas, $\tilde{L}_{oow}$ and $\tilde{L}_{iow}$ are the dimensionless oil-water interface lengths, G_l is the layer shape factor and $\tilde{g}_l$ is the dimensionless layer conductance. The constants a_1 to a_3, tabulated in Table 3.1 are found from a polynomial fit to the numerical results shown in Figure 3.14.

Table 3.1: Tabulation of polynomial fit parameters as a function of corner half angle.

Half angle, β	a_1	a_2	a_3
Global fit	-2.401E-02	2.840E-01	-2.953
0-10	-1.061E-02	5.161E-01	-2.065
10-20	-2.681E-02	1.867E-01	-3.598
20-30	-4.402E-02	-6.320E-02	-4.375
30-40	-3.152E-02	1.695E-01	-3.360
40-50	-3.137E-02	1.933E-01	-3.267
50-60	-2.320E-02	3.118E-01	-2.925
60-	-3.576E-02	-6.537E-04	-4.702

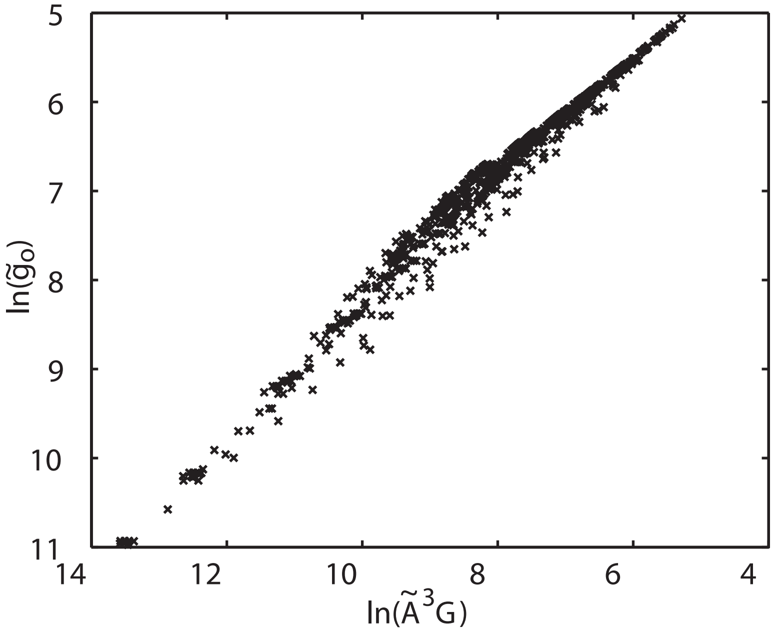

Figure 3.14: Basis for the polynomial fit to data. The dimensionless conductivity can be approximated from the dimensionless layer area and shape factor.

The performance of the correlation, when compared to numerical simulation results, is shown in Figure 3.15. The mean absolute error is 8.7 percent when using a global polynomial fit to the data and 7.1 percent when using a separate fit for 7 intervals of corner half angles. The largest errors occur in the wider corners but this is not such a problem as the combined layer conductance for a network element will typically be dominated by the sharpest corner. It is clear that the proposed correlation compares favourably to that suggested by Hui and Blunt [2000] that has a mean absolute error of 24.7 percent with the largest errors occurring in the important sharp corners, as evident from Figure 3.15 (c). In this work we use separate polynomial fits when calculating oil layer conductance.

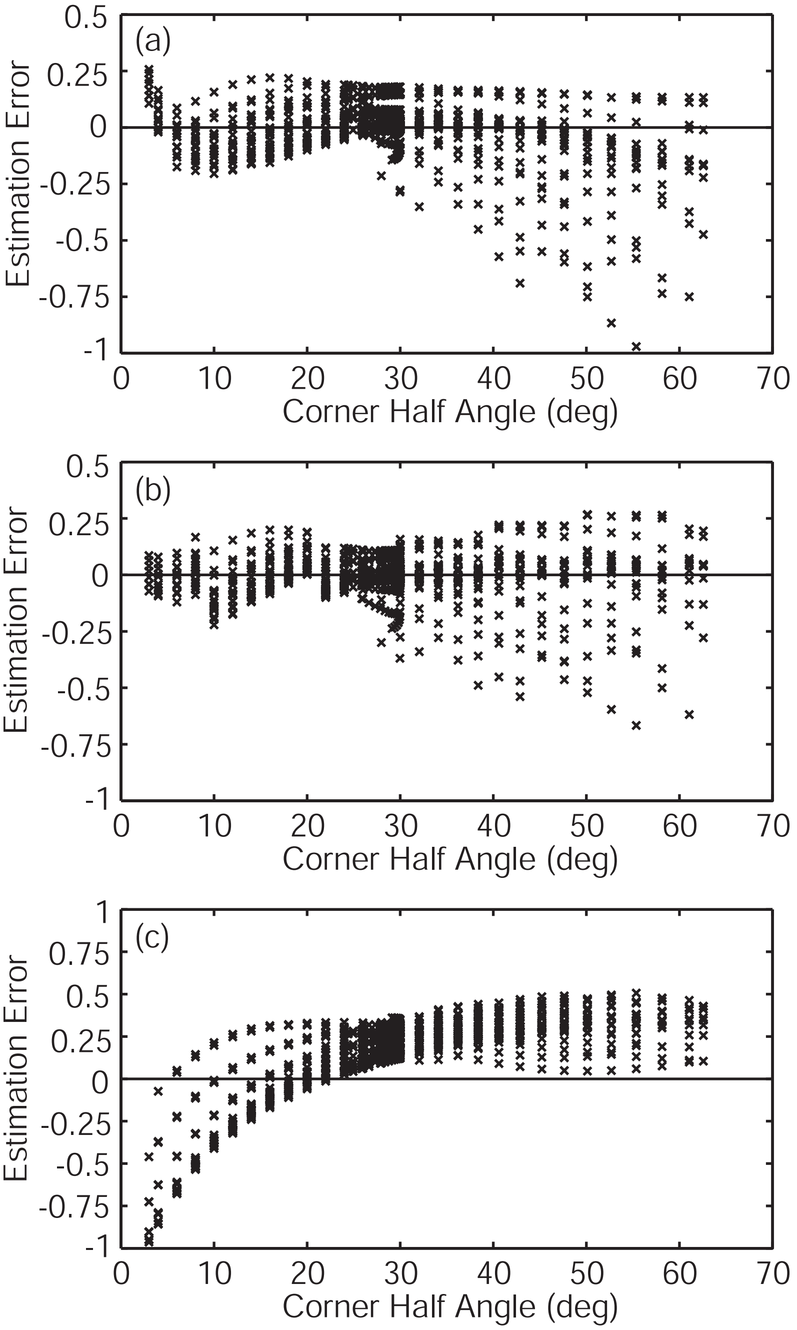

Figure 3.15: Performance of layer conductance correlations when compared to numerical finite element simulations. (a) Proposed correlation with a global polynomial fit. (b) Proposed correlation with separate polynomial fits for different corner half angles. (c) Correlation proposed by Hui and Blunt [2000].

3.6 Electrical properties

Because Poiseuille's law is closely related to Ohm's law, $a = g_e V$, flow of electrical current is analogous to fluid flow, with pressure replaced by voltage V, fluid flow replaced by electrical current a and hydraulic conductance replaced by electrical conductance g_e. This property was used extensively by Fatt [1956c] who generated relative permeability curves by flowing current though an equivalent network of resistors. The electrical analogy to absolute permeability is formation factor F,

$$F = \frac{R_o}{R_w}, \tag{3.59}$$

where R_o is the computed resistivity at 100 percent water saturation and R_w is the water resistivity. Since the rock matrix is non-conductive, formation factor will vary inversely with absolute permeability. The resistivity of the network is found from Ohm's law,

$$R_o = \frac{A \Delta V}{a_{ts} L}, \tag{3.60}$$

where A is the cross-sectional area ΔV is the imposed voltage drop, a_{ts} is the total single phase flow of current and L is the length of the model. The electrical conductance between two pore bodies is assumed to only be a function of the cross-sectional area occupied by the conducting water,

$$g_e = \frac{A_w}{R_w}. \tag{3.61}$$

The potential field is calculated completely analogous to the pressure field, using equations (3.41) to (3.43) to solve for the potential in all pores and subsequently computing total current flow across any cross-sectional plane from (3.42). Clays are typically found to also conduct electricity, though this has not been investigated any further in this thesis. The electrical analogy to relative permeability is resistivity index I, given by

$$I = \frac{R_t}{R_o}, \tag{3.62}$$

where R_t is the resistivity at some given saturation. We assume that only water conducts electricity.

Chapter 4

Predicting Water-Wet Experimental Data

To validate the model we need to compare it against experimental results. In this section we will focus on water-wet experimental data, where the pore-level wettability is fairly easily characterized. We will start with data from Berea sandstones, where we know we have an appropriate network, allowing us to validate the basic network model. Subsequently we will investigate flow in sand packs. This poses a challenge since we have to modify our network to be representative of the porous medium.

As pore-scale network modelling has grown in complexity the amount of possible input parameters has grown. However, for this work the only parameters we will modify are the networks, through a well-defined process, and the pore-level wetting state, defined by the intrinsic contact angle θ_i. All other parameters are kept fixed for all predictions. Most of the experimental data we analyze are based on steady-state measurements. Unsteady-state data, though more abundant, require additional numerical simulations to calculate relative permeability, increasing experimental uncertainty.

4.1 Description of network

In this section we will be using a network generated from reconstructed Berea sandstone [*Lerdahl et al.*, 2000] to predict a wide range of experimental data conducted on several types of porous media. The network covers a rock volume of 3^3 mm^3, consisting of 12,349 pores and 26,146 throats. 6.5 percent of the elements were squares, 1.2 percent were circular with the rest being irregular triangles. The connection numbers varies between 1 and 19, with an average of 4.19. The porosity of the network is 0.24 with an absolute permeability of 2.5 Darcy. The distributions of inscribed radii are shown in Figure 4.1, with the main statistics tabulated in Table 4.1. As expected, there is a clear correlation between the radius of a given pore and the radii of the connecting throats, as seen from Figure 4.2. The correlation coefficient is 0.72.

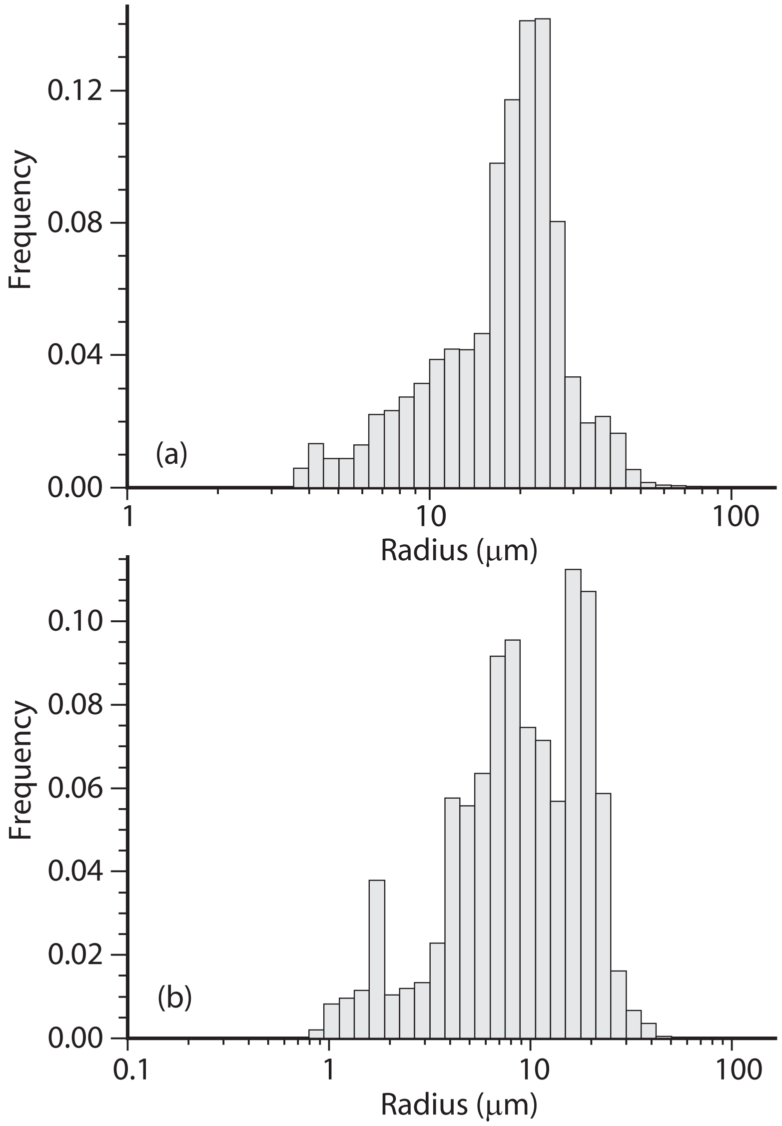

Figure 4.1: Distribution of inscribed radii for Berea sandstone. (a) Pores. (b) Throats.

Table 4.1: Statistical properties of network constructed from Berea sandstone.

	Pore radii	Throat radii
Mean (μm)	19.2	11.0
Standard deviation (μm)	8.5	7.0
Minimum (μm)	3.6	0.9
Maximum (μm)	73.5	56.9

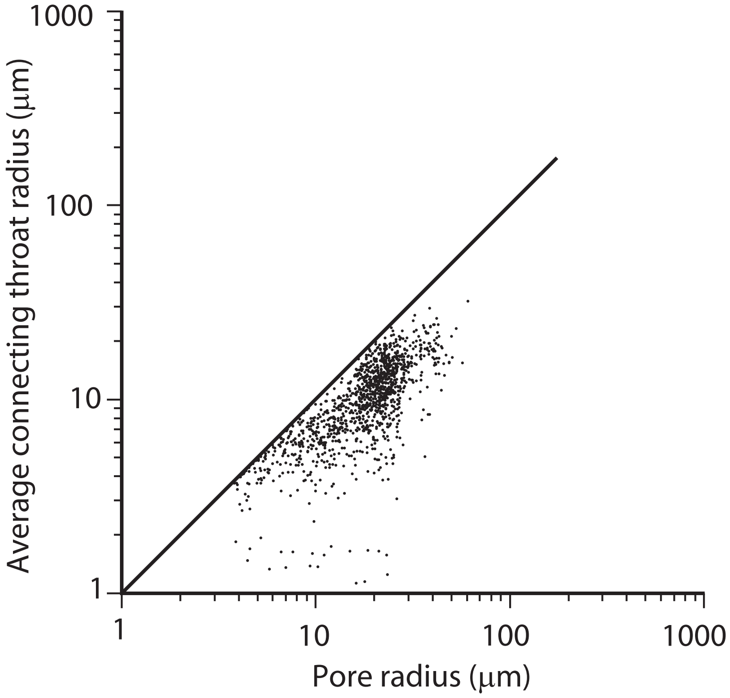

Figure 4.2: Correlation between radii of pores and connecting throats.

4.2 Berea sandstone

Predicted relative permeability for primary and secondary flooding cycles are compared to steady-state experimental data by Oak [1990] for water-oil (Figure 4.3) and oil-gas (Figure 4.4). During the primary flooding cycle the network is assumed to be strongly wetted by the wetting phase (water for the water-oil system and oil for the oil-gas system) with a receding contact angle of 0 degrees. There are no other parameters to adjust, with all geometric network properties (connection numbers, radii, shape factors, *etc*) defined in the sandstone reconstruction process. During the secondary flooding cycle the advancing contact angles will be larger, due to roughness of the surface and minor wettability alteration. The predictions shown in

Figure 4.3 (b) and Figure 4.4 (b) were obtained with intrinsic contact angles uniformly distributed between 50 and 60 degrees for the water-oil system and between 30 and 40 degrees for the oil-gas system.

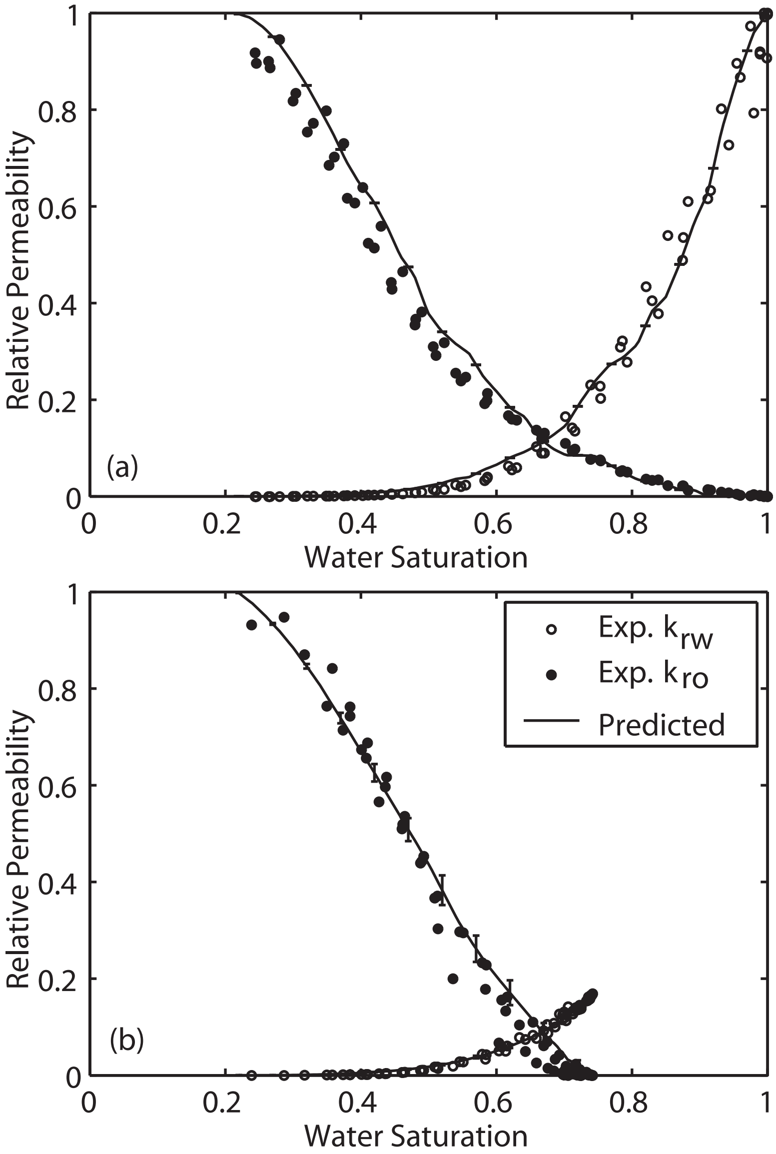

Figure 4.3: Predicted primary oil flooding (a) and secondary water flooding (b) relative permeability for water-wet Berea sandstone (lines) compared to experimental data by Oak [1990] (circles). The predicted results are the mean of 20 realizations and the length of the error bars is twice the standard deviation.

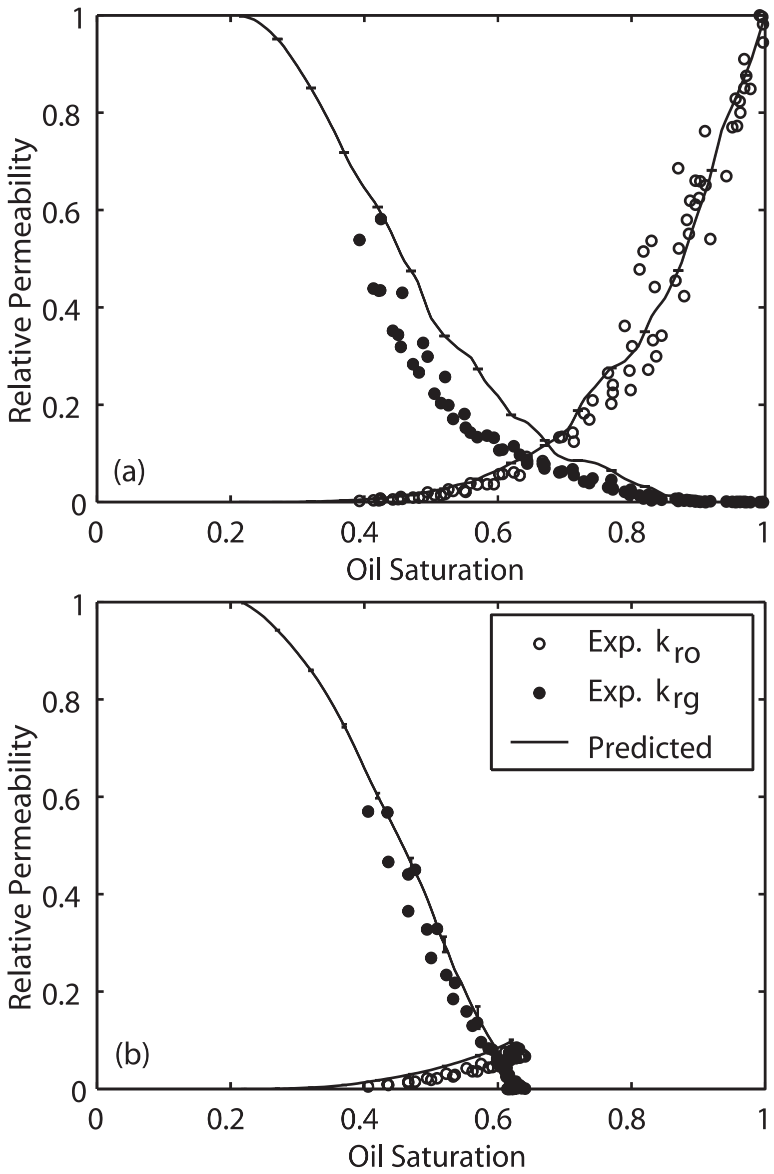

Figure 4.4: Predicted primary gas flooding (a) and secondary oil flooding (b) relative permeability for Berea sandstone (lines) compared to experimental data by Oak [1990] (circles). The predicted results are the mean of 20 realizations and the length of the error bars is twice the standard deviation.

The corresponding advancing contact angles can be found from Figure 3.6. Small changes in the distribution of contact angles did not significantly affect the results, as long as the contact angles were less than 90 degrees. Additional fluid and rock parameters are given in Table 4.2. The predictions are the mean of 20 realizations with the length of the error bars being twice the standard deviation. The network topology and the pore and throat sizes are the same for all realizations. The statistical variation is mainly the result of contact angles being randomly distributed. During the primary flooding cycle there is hardly any variation as contact angles are kept at a constant 0 degrees, though there is some small variation in the network due to the random assignment of the intermediate corner half angle. All predictions generally agree very well with the experimental data, with the exception of gas relative permeability in the primary oil flooding cycle. Oak [*Oak*, 1990] noted that this gas relative permeability was highly affected by the flooding rates used, and this might thus be the cause of the observed difference between experimental and predicted results.

Table 4.2: Fluid and rock properties used in predictions of experimental data by Oak [1990].

Connate water saturation	0.22
Surface tension, σ (10^{-3} N/m)	30.0
Water viscosity, μ_w (10^{-3} Pa/s)	1.05
Oil viscosity, μ_o (10^{-3} Pa/s)	1.39
Gas viscosity, μ_g (10^{-5} Pa/s)	1.87

4.3 Sand pack

When using pore-scale modelling to predict experimental data it is clearly important that the underlying network is representative of the rock. However, if the exact rock type has to be used for the network construction the application of predictive pore-scale modelling will be severely limited due to the complexity and cost of methods such as X-ray microtomography. In this section we will use the topological information of the Berea network (relative pore locations and connection numbers) while tuning the properties of the individual network elements using capillary pressure data. This modified network will be used to predict the flow properties of a sand pack (Table 4.3) as measured by Dury *et al.* [1997; 1998]. The experimental data are based on air-water with capillary pressure and air relative permeability available for secondary air flooding and tertiary water flooding, also referred to as the main flooding cycles. The relative permeabilities were obtained using the stationary liquid method. In this case air is the non-wetting phase, and is treated identically to oil.

Table 4.3: Rock properties of sand pack used in experiments by Dury *et al.* [1998].

Porosity	0.356
Grain size distribution (mm)	0.08 − 1.2
Column length (cm)	15

The capillary pressures for the sand pack are shown in Figure 4.6 (b). By assuming the network to be a bundle of capillary tubes it is possible to obtain an initial estimate of the throat size distribution using the air flooding capillary pressures and (3.6). Intrinsic contact angles used in the network model are consistent with experimentally measured values (Table 4.4) and during air flooding the model is strongly water-wet. Individual network throats are assigned inscribed radii from this target distribution. This is done by first sorting all throats according to their radius. Each throat in the list, starting with the largest, are then assigned a new inscribed radius from the target distribution by simply doing a table lookup with cumulative throat volume used as input, as illustrated in Figure 4.5. This will preserve their rank order – that is the largest throat in the network is given the largest radius from the target distribution and so on, which should ensure that size correlations between individual elements and on larger scales are maintained.

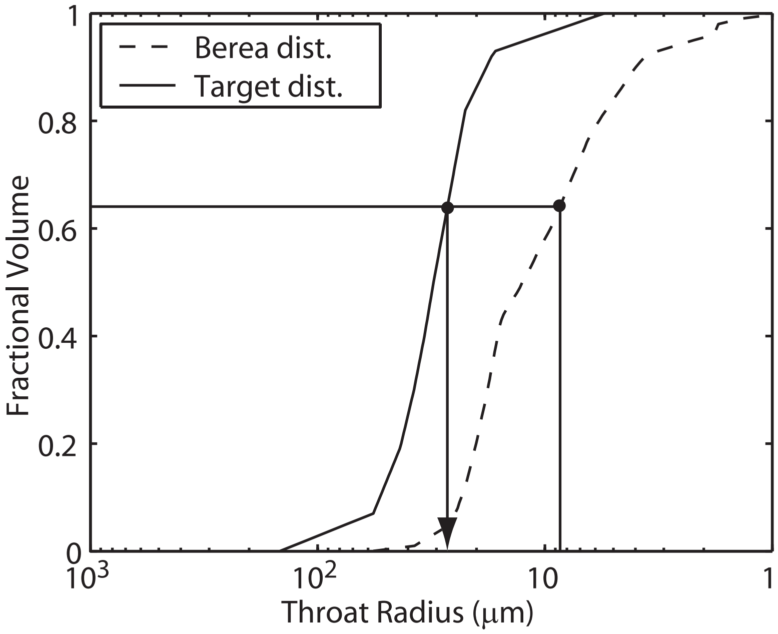

Figure 4.5: Throat elements are assigned new radii from the target distribution by doing a table lookup, using cumulative throat volume as input.

From Figure 4.6 (b) it is, however, clear that the predicted capillary pressure is not close to the experimental data. This indicates the difficulty of predicting multiphase data – the capillary pressure and relative permeabilities are influenced by the spatial distribution of pores and throats and their connectivity, something that cannot be captured using a bundle of capillary tubes assumption. The target distribution of throat sizes is subsequently modified iteratively until an adequate pressure match is obtained against the experimental air flooding data (Figure 4.7). Modifications to the throat size distribution at each iteration step were done by hand rather than by any optimization technique. The results are insensitive to the details of how the throat sizes are adjusted.

Table 4.4: Fluid properties used in predictions of experimental data by Dury *et al.* [1998].

	Water	Air
Surface tension, σ (10^{-3} N/m)	70.25	—
Measured adv. contact angle, θ_a (deg)[a]	19.9	—
Measured rec. contact angle, θ_r (deg)[a]	13.5	—
Intrinsic contact angles used, θ_i (deg)	30 - 40	—
Density, ρ (kg/m^3)	1000	1.22
Viscosity, μ (10^{-3} Pa/s)	0.97	0.018
[a] Measured using Wilhelmy plate method		

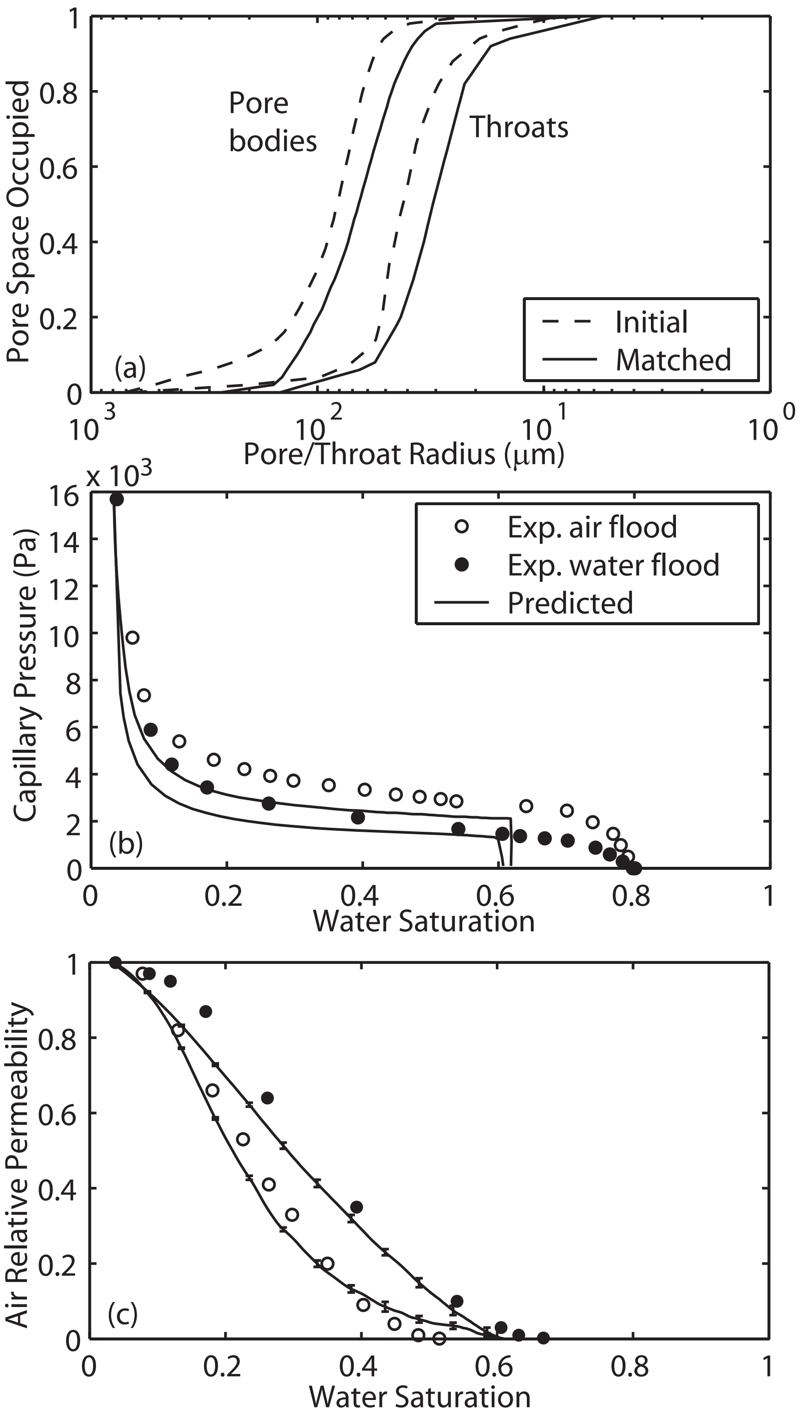

Figure 4.6: Comparison between predicted properties and experimental data by Dury *et al.* [1998]. (a) Using the experimental capillary pressure and a bundle of capillary tubes assumption an initial estimate for the throat size distribution can be made. However, the predictions for capillary pressure (b) and relative permeability (c) are poor, indicating that the pore size distribution needs to be adjusted to match the data.

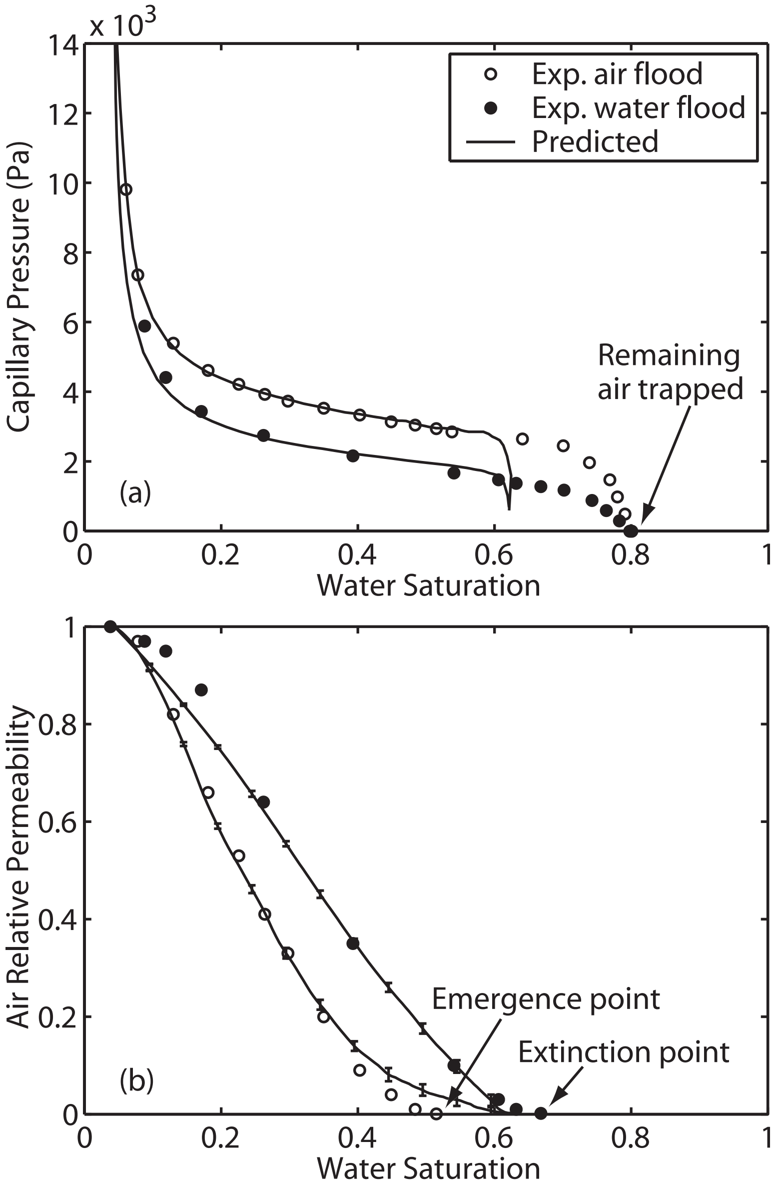

Figure 4.7: Comparison between predicted properties and experimental data by Dury *et al.* [1998] following a network modification process to match the capillary pressure data. (a) The match to experimental capillary pressure is excellent, except at high water saturations. (b) Predictions of air relative permeability are also improved.

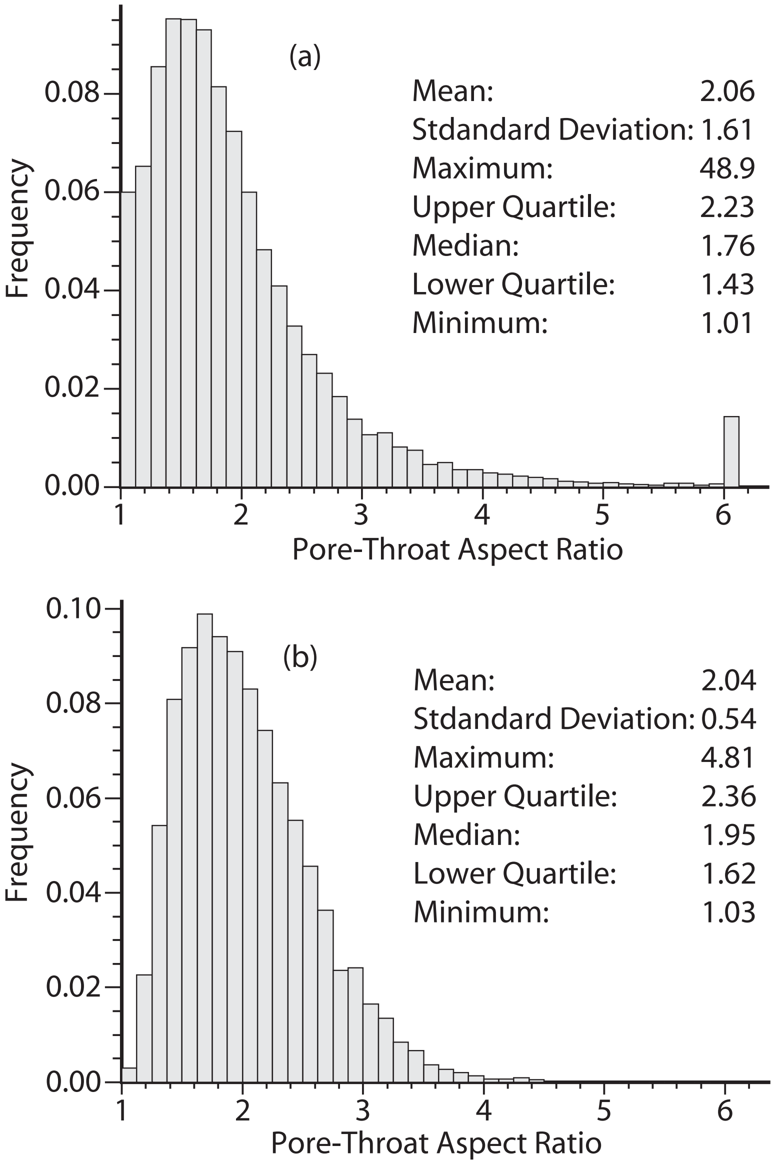

Figure 4.8: Distribution of pore body to throat radius aspect ratio for original Berea network (a) and modified network (b). The latter is used for predictions of experimental data by Dury *et al.* [1998].

Capillary pressure hysteresis is a function of both the contrast between pore body and throat radii and the contact angle hysteresis. The radii of the pore bodies is determined from

$$r_p = \max\left(\alpha\frac{\sum_{i=1}^{n} r_i}{n},\ \max(r_i)\right), \tag{4.1}$$

where n is the connection number and α is the aspect ratio between the pore body radius r_p and connecting throat radii r_i. A good match to experimental water flood capillary pressure is achieved by distributing the aspect ratios between 1.0 and 5.0 with a mean of 2.0. This distribution is very similar to that of the original Berea network (Figure 4.8), though with a lower maximum value, which in the original network was close to 50. This is expected since an unconsolidated sand pack would typically have smaller aspect ratios than a consolidated Berea sandstone. The absolute size of the model, defining individual pore and throat lengths, is adjusted such that the average ratio of throat length to radius is maintained from the original network. Pore and throat volumes were adjusted such that the target porosity was achieved, again maintaining the rank order. The final pore body and throat size distributions are shown in Figure 4.6 (a). Both distributions are shifted towards smaller values compared to the initial estimates.

In Figure 4.7 (b) the predicted air relative permeability for secondary air flooding and tertiary water flooding are compared to experimental data by Dury *et al.* [1998]. For experimental convenience the relative permeability was calculated using the air flow rate at connate water saturation S_{wc} rather than that at single phase conditions as defined by (3.40). This has, however, little influence on the results since our computed air relative permeability is 0.99 at S_{wc}. Both the relative permeability hysteresis and the extinction point (where air no longer flows across the model) following water flooding are well predicted.

From the capillary pressure curve we appear to predict much higher residual gas saturation than in the experiments. Dury [1997] suggested that the large difference in saturation between where all remaining air is trapped and where it is able to flow across the pack could be partly related to air compressibility but more likely is due to the displacement of clusters of air not spanning the network. In the network model this difference is in the order of a few percentage points, rather than the almost 20 percent seen in the experiments.

The large experimental difference between the emergence point (where air is first able to flow across the model during air flooding) and the extinction point, something that is not observed in the network model, is difficult to explain physically. Using a network originally constructed to represent a consolidated Berea sandstone, it is possible that the contrast in size between pore bodies and connecting throats is still over-predicted. This could result in snap-off becoming too dominant, resulting in too high predictions of residual oil. However, this is unlikely to explain why the network model predicts considerably smaller difference between the emergence and extinction points. With snap-off being less dominant, the number of trapped clusters following water flooding should be smaller. It would be naturally to expect that fewer forced displacement events are needed before a gas cluster once again spans the network. Hence, an over-prediction of the size contrast between pore bodies and throats should, if anything, lead to an over-prediction of the difference between emergence and extinction points.

The methodology of tuning the properties of the network to experimental capillary pressure, which is fairly easy to obtain, in order to match transport properties such as relative permeability, which undoubtedly is more difficult to obtain, has been attempted by several authors [*Wise*, 1992; *Rajaram et al.*, 1997; *Fischer and Celia*, 1999]. What distinguishes this method is that we use networks that are constructed directly from realistic images of porous media. Our assumption is that the higher order topological information, that Sok *et al.* [2002] found were crucially important if reliable predictions of transport properties were to be made, are less specific to a given system than are properties such as pore size distribution. By preserving the rank order of the individual network elements we not only maintain topological information but we also go some way towards resolving the problem of non-uniqueness as noted by Vogel [2000]. Fischer and Celia [1999] also attempted to predict this data [*Dury et al.*, 1998]. Although the relative permeability for the water flooding cycle was reasonably well predicted, they were unable to predict the observed hysteresis, resulting in a poor prediction for the gas flooding cycle. With the approach presented here we have been able to successfully predict relative permeability for both flooding cycles.

Chapter 5

Wettability Effects on Experimental Data

Most hydrocarbon-bearing reservoir rocks are found to be mixed-wet, where parts of the grain surface have become oil-wet while the rest remains water-wet [*Anderson*, 1986a]. We will first predict data from mixed-wet Berea cores. Though the network geometry should still be valid, pore-level wettability and residual saturations are more uncertain. We will subsequently try to predict mixed-wet relative permeability for other rock types. This poses a challenge since we have to modify our network while at the same time try to characterize the pore-level wetting state.

The wetting states of the cores are typically determined using the Amott method [*Anderson*, 1986b], measuring the fraction of each phase p that spontaneously imbibes,

$$I_p = \frac{\Delta S_{ps}}{\Delta S_{ps} + \Delta S_{pf}}, \tag{5.1}$$

where ΔS_{ps} and ΔS_{pf} are the spontaneous and forced parts of the displacement. It is typical to report the wetting state through a combined water-oil index $I_{w-o} = I_w - I_o$, where I_w and I_o are the water and oil indices.

5.1 Mixed-wet Berea sandstone

The influence of wettability on oil recovery during water flooding has been extensively investigated by Jadhunandan and Morrow [1995]. Experiments were conducted on 50 Berea core samples. Following primary oil flooding to some initial water saturation, between 7.9 and 32 percent, the cores were aged, during which the wettability was altered, and then subsequently water flooded until 20 pore volumes had been injected.

Using the network model combined with Buckley-Leverett analysis [*Dullien*, 1992] the experiments were reproduced to see if the same trends and results could be predicted. All cores were assumed to have connate water saturation S_{wc} of 7.9 percent, equal to the lowest initial saturation in the experiments. Following primary oil flooding to some initial water saturation S_{wi}, all network elements contacted by oil were assumed to have their wettability altered. Oil recovery was determined from the secondary water flooding cycle. Finally the Amott wettability indices were determined with additional oil and water flooding cycles. All cycles except primary oil flooding were terminated following 20 pore volumes injected with the corresponding residual saturation and oil recoveries determined from a one-dimensional Buckley-Leverett analysis using the predicted network relative permeability and ignoring capillary pressure. Fluid parameters are given in Table 5.1.

Table 5.1: Fluid properties used in predictions of experimental data by Jadhunandan and Morrow [1995]

Surface tension, σ (10^{-3} N/m)	12.0
Water viscosity, μ_w (10^{-3} Pa/s)	0.99
Oil viscosity, μ_o (10^{-3} Pa/s)	5.23

Careful attention to wettability characterization and displacement processes is needed to explain the surprising experimental results shown in 5.1 (a), where as S_{wi} increases recovery initially increases but then decreases again for the largest values. The simplest scenario is that for a given crude oil, brine and rock condition the distribution of contact angles in pores contacted by oil during primary oil flooding is similar regardless of initial water saturation [*Jackson et al.*, 2003]. The wettability variation observed through the Amott indices is then just a function of S_{wi}, with the rock becoming less oil-wet as S_{wi} increases, since fewer pores have their wettability altered. By matching the observed wettability indices at a given initial water saturation it should then be possible to predict the trends in recovery and wettability as S_{wi} is varied. With connate water saturation chosen as the reference case the wetting state was reasonably well matched with intrinsic contact angles in wettability-altered pores uniformly distributed between 85 and 120 degrees. The

Amott water I_w and oil I_o indices were calculated to be 0.00 and 0.47, the same as the experimental values.

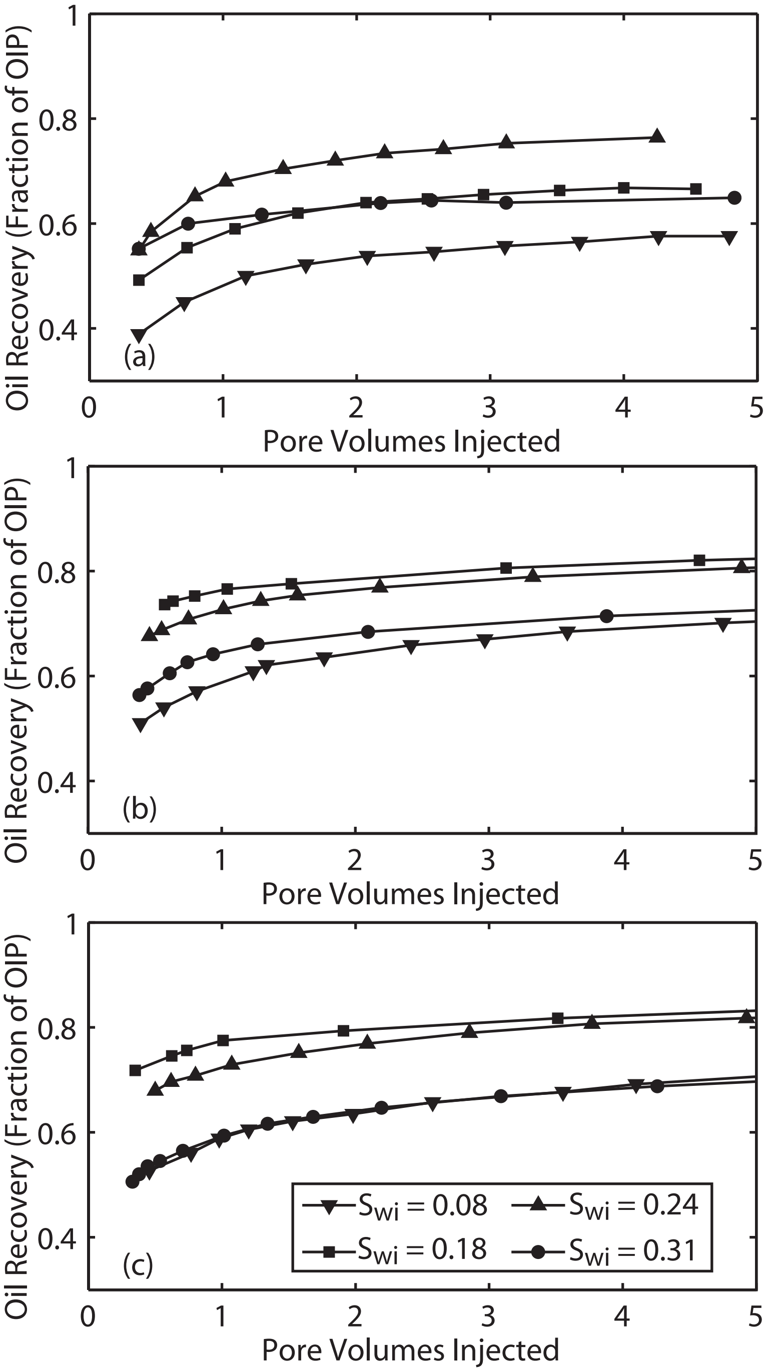

Figure 5.1: Oil recovery for different initial water saturations. (a) Experimental data from Jadhunandan and Morrow [1995]. (b) Predicted recoveries using pore-scale modelling with a fixed distribution of intrinsic contact angles between 85 and 120 degrees. (c) Predictions where fewer pores become oil-wet for S_{wi} above 0.20.

Oil recovery is a direct function of the fractional water flow f_w, which in the one-dimensional Buckley-Leverett analysis is given by

$$f_w(S_w) = \frac{1}{1 + \dfrac{k_{ro}(S_w)\,\mu_w}{k_{rw}(S_w)\,\mu_o}}. \tag{5.2}$$

From (5.2) it is clear that the relative permeability being low for water and high for oil is advantageous to oil recovery. Relative permeability curves for different S_{wi} are shown in Figure 5.3, along with water fractional flow curves and capillary pressures. Although snap-off is possible, it is highly unfavourable compared to piston-like displacement in oil-wet conditions. Hence, water will typically enter the model through piston-like displacement from existing water-filled elements. If S_{wi} is low there are relatively few of these left following primary oil flooding, resulting in water entering the model though large well-connected clusters. To illustrate this we ran a 2D network simulation with the same distribution of contact angles and the results are shown in Figure 5.2 (a). As S_{wi} increases, the number of initially water-filled elements will increase rapidly, Figure 5.2 (b). These are typically isolated elements, resulting in water entering the system through many clusters only connected through layers. This behaviour has significant influence on relative permeability, since flow conductance in layers is typically orders of magnitude less than that in pore centres. In cases where there are many initial clusters, water has to repeatedly flow through layers to connect from inlet to outlet, resulting in low relative permeability, as evident from the S_{wi} = 0.18 case in Figure 5.3. Since the initially oil-filled elements are oil-wet, water preferentially fills the larger pores and throats. This results in a large increase in water saturation with little change in water connectivity and hence water relative permeability, Figure 5.2 (c). Only at high water saturations, around 0.7, will the water clusters start to coalesce, resulting in a rapid increase in water relative permeability. In the limiting case where $S_{wi} = S_{wc}$ there is only a single water cluster originating from the inlet reservoir, which rapidly establishes a connected path of water-filled elements across the network giving a more gradual increase in k_{rw}.

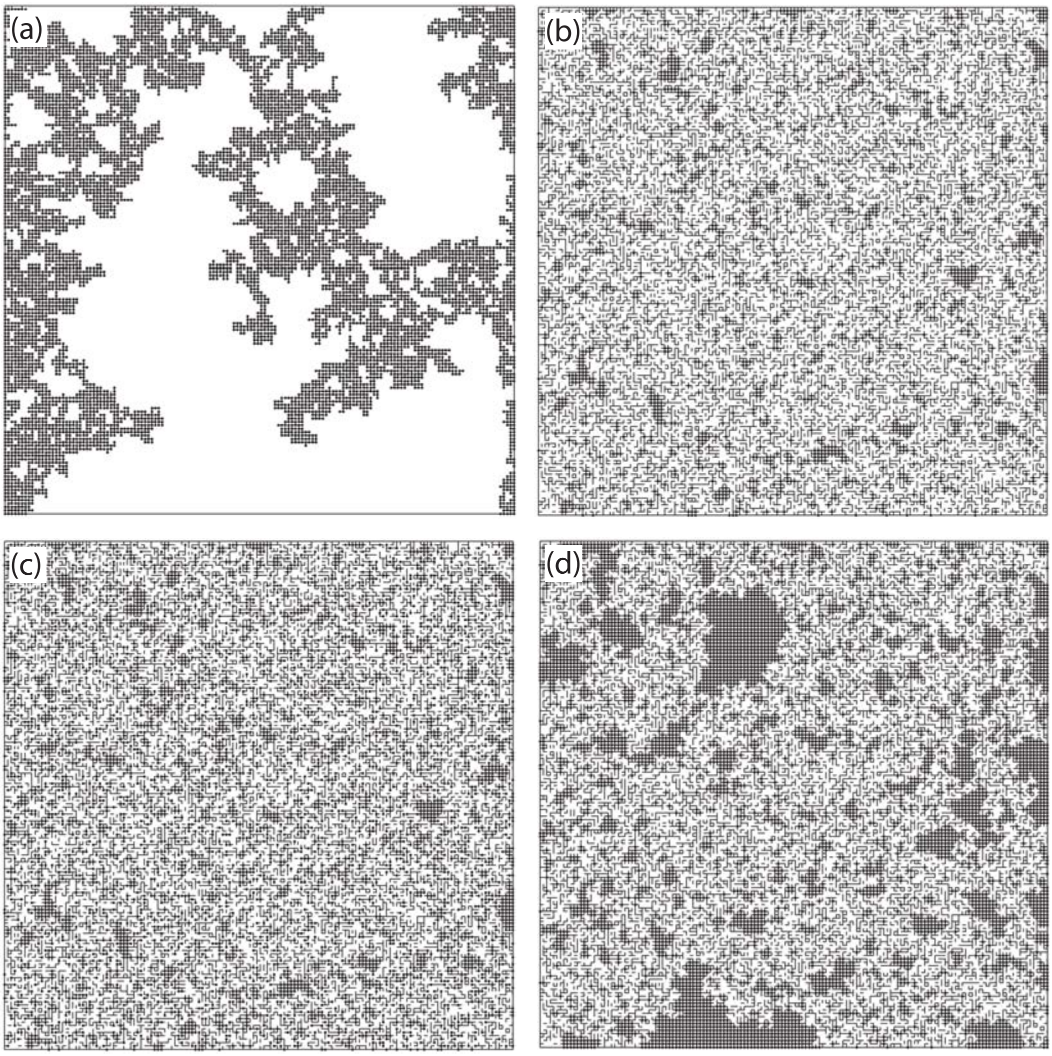

Figure 5.2: Distribution of water-filled elements during water flooding. (a) When $S_{wi} = S_{wc} = 0.08$ very few elements remain water-filled following primary oil flooding. During water flooding there will only be a few well connected clusters, even at $S_w = 0.40$ as shown. Water spans the network through completely filled elements, resulting in a high relative permeability. (b) When $S_{wi} = 0.18$ many throats will remain water-filled at the shown initial condition. (c) As water is injected, each water-filled throat will allow for piston-like displacement into a neighbouring pore body, resulting in rapid increase in water saturation without much change in the overall network conductivity, even at the shown saturation of 0.40, giving a very low water relative permeability. (d) When $S_{wi} = 0.31$ connected water clusters will remain at the shown initial conditions, resulting once again in increased water relative permeability.

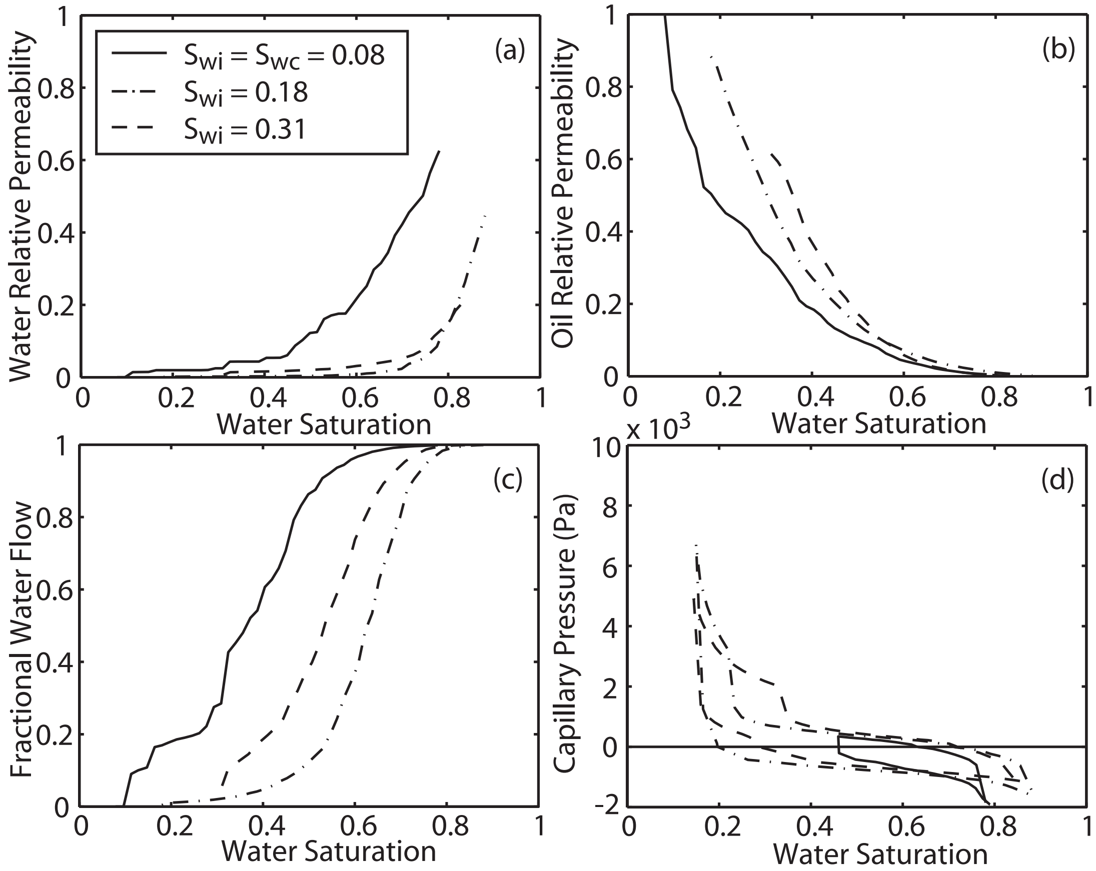

Figure 5.3: Influence of S_{wi} on macroscopic flow properties during secondary water flooding. We have assumed that all pores contacted by oil after primary oil flooding have a fixed distribution of intrinsic contact angles between 85 and 120 degrees, corresponding to the predictions shown in 5.1 (b). Each flooding cycle is terminated after 20 pore volumes have been injected. (a) Water relative permeability. (b) Oil relative permeability. (c) Fractional water flow. (d) Capillary pressure during secondary oil flooding and tertiary water.

There is less effect of S_{wi} on the oil relative permeability. The last elements to be filled during primary oil flooding are the smallest ones that also contribute the least to oil conductance, whereas the first elements filled during water flooding in oil-wet conditions are the largest, resulting in large oil relative permeability hysteresis. The oil relative permeability for a given S_{wi} will thus lie above those starting from a lower S_{wi}.

The effects on both oil and water relative permeability combine to give lower fractional water flow, and subsequently higher recovery, as S_{wi} increases. There is, however, an optimal S_{wi} above which recovery again starts to decrease, as evident from Figures 5.1 and 5.3 (c). Elements filled by water during water flooding still conduct oil due to oil layers, which is not the case for elements that remain water-filled from primary oil flooding. This results in increased oil trapping with S_{wi}, reducing oil relative permeability. Also, at some point so many elements still contain water at the beginning of water flooding that large water clusters can easily form, increasing the water relative permeability, as illustrated in Figure 5.2 (d). Whereas relative permeability and fractional flow show a non-uniform trend with S_{wi}, this is not the case for the Amott wettability indices (Table 5.2), calculated from the capillary pressures as shown in Figure 5.3 (d).

Table 5.2: Variation in Amott wettability indices for different initial water saturations.

	Experimental Data		Fixed wettability		Variable wettability	
S_{wi}	I_w	I_o	I_w	I_o	I_w	I_o
0.079	0.00	0.47	0.00	0.47	0.00	0.47
0.180	0.02	0.20	0.06	0.23	0.07	0.22
0.240	0.20	0.07	0.13	0.21	0.20	0.07
0.311	0.34	0.00	0.19	0.18	0.35	0.02

Although we are able to match the trend in recovery with S_{wi} (5.1), the quantitative match is poor in some cases. Maximum recovery is predicted to occur at lower S_{wi} and the variation in recovery with S_{wi} is predicted to be less than what is observed experimentally. Recovery and residual oil saturation, as a function of the Amott-Harvey water-oil index $I_{w\text{-}o}$, is shown in Figure 5.4. Again, the trend and maximum oil recovery are well predicted, though the predicted results are somewhat shifted towards more oil-wet conditions.

Our initial hypothesis that the distribution of contact angles in pores contacted by oil is independent of initial water saturation and brine salinity (in terms of Ca^{2+} content) does not seem to be entirely supported when comparing predicted and experimental trends in Amott wettability indices. In Table 5.2 the wettability indices corresponding to Figure 3.1 are tabulated. These experiments were all preformed with high salinity brines. It is clear that as initial water saturation increases the rock exhibits more water-wet behaviour than what can be attributed to just increasing S_{wi}.

This observation is further supported by Figure 5.5, where more experimental data points are included. A fixed distribution of contact angles will result in a linear increase in water index with S_{wi}, which is not seen experimentally. Physically, this can be explained using the pore-level scenario suggested by Kovscek *et al.* [1993]. Initially a water film covers the rock, preventing direct contact by the oil. At a certain capillary pressure this film will rupture, allowing the rock to become more oil-wet. As S_{wi} increases the maximum capillary pressure during primary oil flooding is reduced, preventing some of the pores attaining oil-wet characteristics. It would seem that for S_{wi} greater than 0.18 a significant fraction of the pores remain water-wet. To see if the quantitative match would improve, this trend was incorporated into the predictions, Figure 5.5.

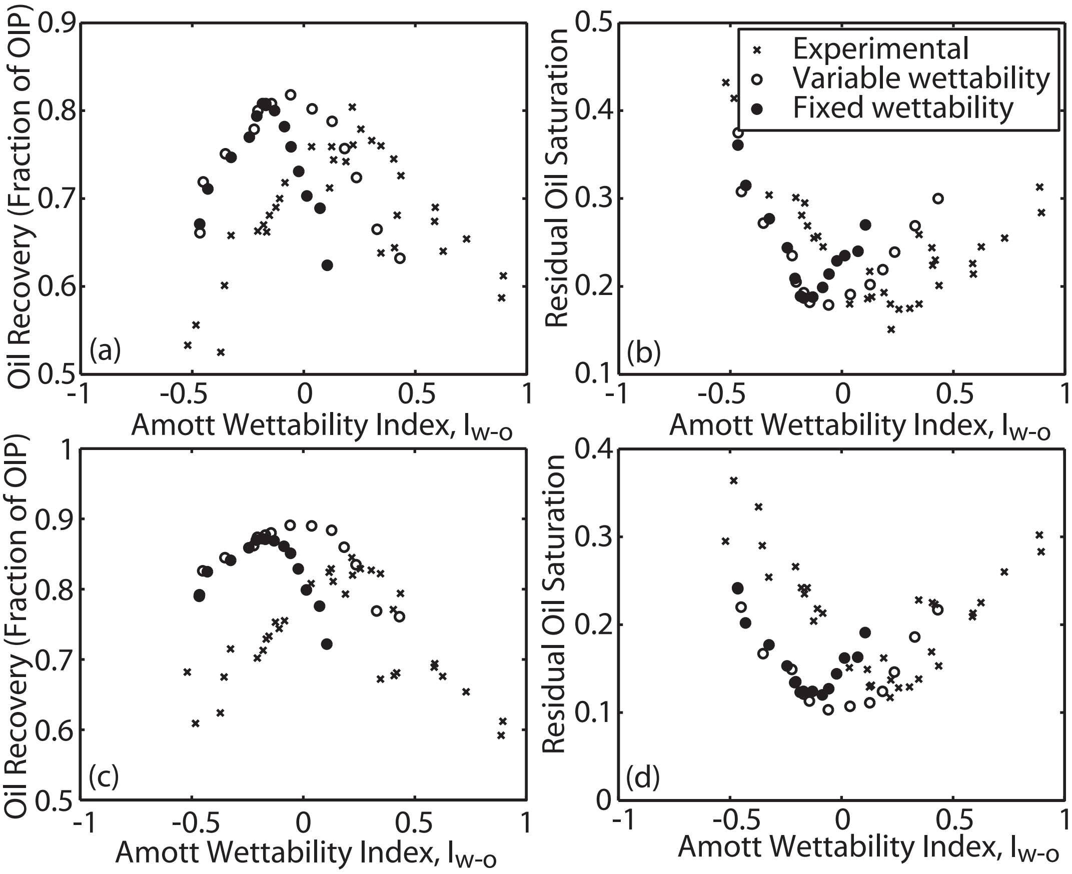

Figure 5.4: Recovery and residual oil saturation as a function of Amott wettability index I_{w-o} for (a-b) 3 pore volumes injected and (c-d) 20 pore volumes injected. Predictions are shifted towards more oil-wet conditions compared to experimental data.

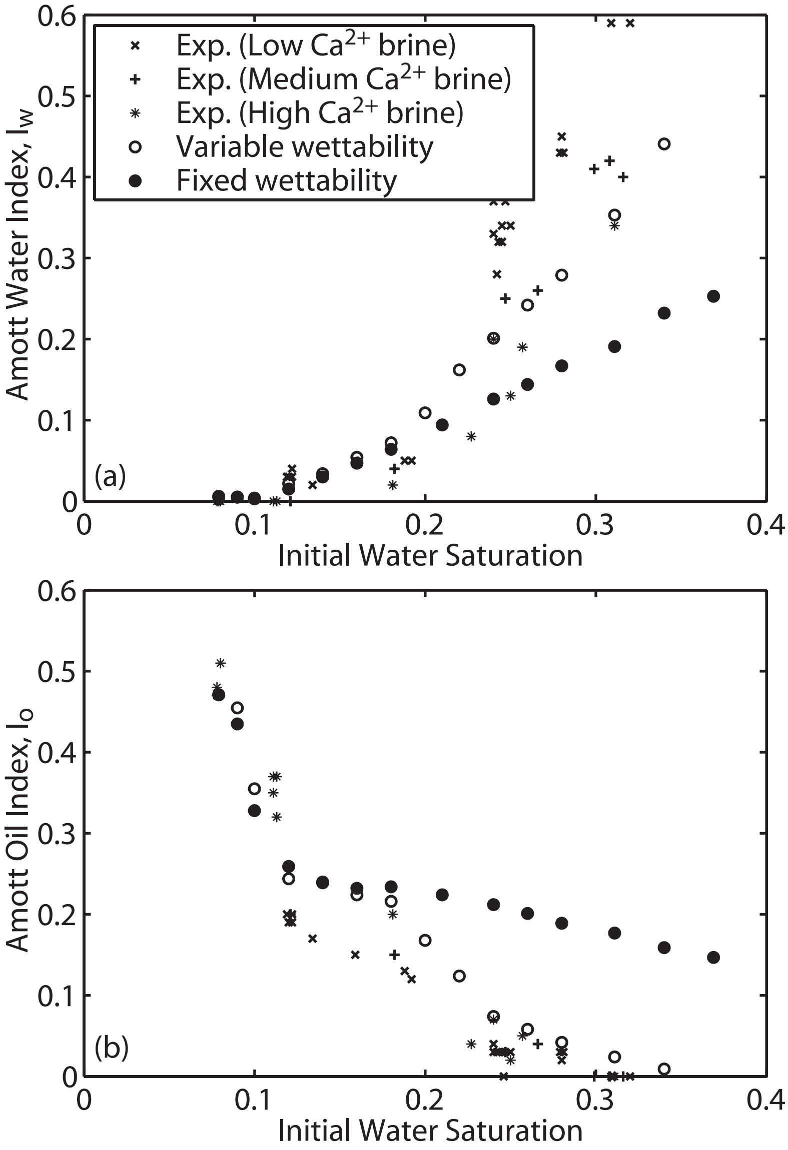

Figure 5.5: Influence of initial water saturation on Amott water (a) and oil (b) indices. From the experimental water indices it is clear that variation in wettability can not only be attributed to variation in S_{wi}.

After primary oil flooding we assigned a target volume fraction of oil-filled pores and throats that would become oil-wet. The largest oil-filled pores were made oil-wet with an intrinsic contact angle randomly distributed between 90° and 118°. Though this contradicts the pore-level scenario suggested by Kovscek *et al.* [1993], that suggested that the largest oil-filled pores would remain water-wet, it is consistent with the approach used by other network modelling studies [*McDougall and Sorbie*, 1995; *Øren and Bakke*, 2003] that have investigated the experimental data by Jadhunandan and Morrow [1995]. Oil-filled throats connected to oil-wet pores were made oil-wet with the same distribution of contact angles with a probability equal to the target oil-wet fraction. Progressively smaller oil-filled pores were made oil-wet until the target fraction was reached. The remaining oil-filled pores and throats were assigned intrinsic contact angles uniformly between 50° and 60°. We varied the upper bound on the oil-wet contact angle distribution along with the oil-wet fraction to better match the experimental Amott wettability indices for $S_{wi} > 0.18$, the results are shown in Table 5.2 and Figure 5.5. The upper bound of the contact angle distribution was reduced from 118 degrees at $S_{wi} = 0.18$ to 109 degrees at $S_{wi} = 0.31$, while the lower bound was kept at 90 degrees. The oil-wet fraction was reduced from 1 to 0.87. This did indeed widen the range of wetting conditions observed, Figure 5.4. However, maximum recovery still occurs at initial water saturations lower than those observed experimentally, 5.1 (c).

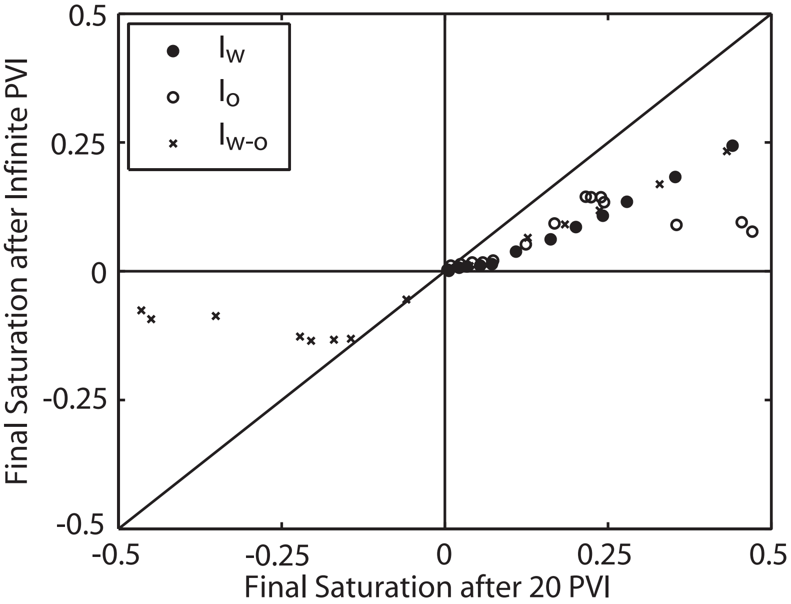

Figure 5.6: Effect from differences in saturation history when determining Amott water I_w, oil I_o, and combined I_{w-o} wettability indices. The additional forced displacement when allowing an infinite number of pore volumes to be injected will result in both lower water and oil indices, resulting in less variation in estimated wetting state.

Øren and Bakke [2003] also used a pore-scale network model, similar to the one presented in this work, to predict recoveries while matching the trend in S_{wi} and Amott wettability indices. Whereas we predicted maximum oil recovery to occur at weakly oil-wet conditions, they were able to reproduce the findings by Jadhunandan and Morrow [1995] that the maximum occurs at weakly water-wet conditions. When determining the final residual saturation after each flooding cycle, we considered it most realistic that this would be the saturation achieved after 20 pore volumes injected (PVI), as determined by the Buckley-Leverett analysis, following secondary oil flooding and tertiary water flooding. Though not explicitly stated, it is assumed that Øren and Bakke used secondary water and oil flooding cycles to determine the wetting state, allowing each cycle to continue until only a final trapped saturation remained, in effect allowing an infinite number of pore volumes to be injected. This will result in additional spontaneous and forced displacement, compared to our approach.

Table 5.3: Matched Amott wettability indices for different experimental core samples.

	Exp. Data		Infinite PVI		r_{min} correlation		$S_{wc} = 0.22$	
S_{wi}	I_w	I_o	I_w	I_o	I_w	I_o	I_w	I_o
0.079	0.00	0.47	0.00	0.47	0.00	0.48	0.00	0.47
0.113	0.00	0.37	0.01	0.38	0.01	0.38	0.00	0.38
0.121	0.00	0.20	0.01	0.21	0.01	0.21	0.00	0.20
0.159	0.05	0.15	0.05	0.15	0.05	0.14	0.05	0.16
0.181	0.02	0.20	0.03	0.21	0.02	0.20	0.02	0.20
0.188	0.05	0.13	0.05	0.12	0.05	0.12	0.05	0.14
0.227	0.08	0.04	0.08	0.03	0.09	0.04	0.08	0.05
0.240	0.20	0.07	0.20	0.08	0.20	0.07	0.20	0.07
0.250	0.13	0.02	0.13	0.02	0.12	0.02	0.13	0.02
0.250	0.34	0.03	0.34	0.03	0.34	0.03	0.33	0.03
0.266	0.26	0.04	0.27	0.04	0.27	0.04	0.26	0.04
0.311	0.34	0.00	0.35	0.01	0.33	0.01	0.34	0.01
0.316	0.40	0.00	0.42	0.01	0.41	0.01	0.41	0.01
0.320	0.59	0.00	0.57	0.00	0.58	0.01	0.56	0.01

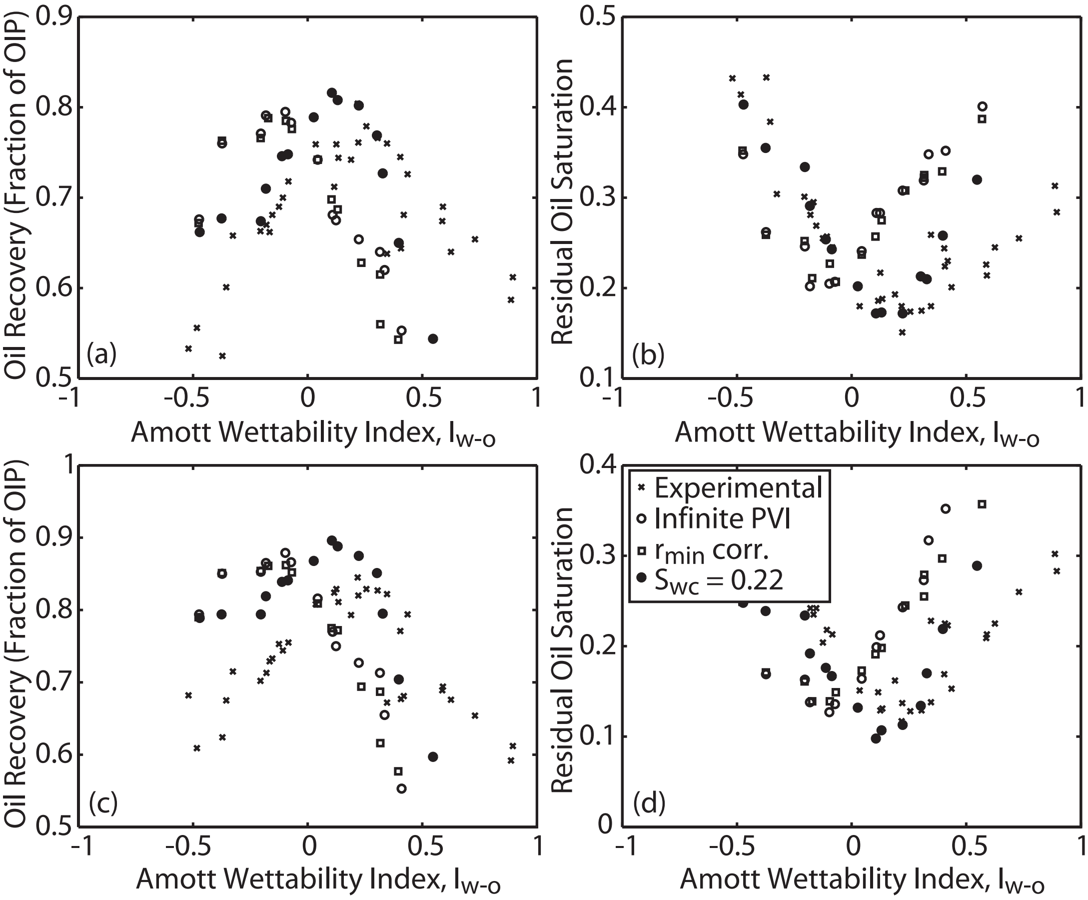

Figure 5.7: Recovery and residual oil saturation as a function of Amott wettability index $I_{w\text{-}o}$ for (a-b) 3 pore volumes injected and (c-d) 20 pore volumes injected. For all cases, the flooding cycles were terminated once the absolute residual saturations were reached, in effect allowing an infinite number of pore volumes to be injected.

To investigate the influence from these differences in saturation history, we reran our variable wettability cases, but used the secondary flooding cycles to determine the Amott wetting indices while allowing infinite pore volumes to be injected. From Figure 5.6 it is clear that this will result in less variation in the combined Amott wettability index $I_{w\text{-}o}$ but without changing the overall predicted wetting state (water or oil-wet). Maximum recovery is still predicted to occur at weakly oil-wet conditions, as evident from Figure 5.7 (infinite PVI case), where the wetting states of 14 experimental core samples were matched (Table 5.3). The water index was matched by varying the oil-wet fraction during secondary water flooding while the oil index was matched by adjusting the upper bound of the oil-wet contact angle distribution, keeping the lower bound at a constant intrinsic contact angle of 80 degrees. As predicted, a larger variation in the oil-wet fraction was needed to match the experimental data. For the $S_{wi} = 0.311$ an oil-wet fraction of 0.83 was needed, compared to a fraction of 0.87 used when terminating the flooding cycle after 20 PVI.

For all cases investigated so far the larger pores have been made preferentially oil-wet. In Figure 5.7 we investigate the effect from letting the smaller pores become preferentially oil-wet (r_{min} correlation). Once again the wetting states of 14 experimental core samples were matched (Table 5.3) while determining the Amott indices from the secondary flooding cycles, allowing an infinite number of PVI. There is very little difference in the results when compared to letting the larger pores become preferentially oil-wet. The reason for this is that recovery efficiency is dominated by the remaining water-filled elements following primary oil flooding with the oil-wet fraction of the invaded elements generally being quite high. Maximum recovery is predicted to occur at an oil-wet fraction of about 0.97.

In the network model we assumed a constant connate water saturation of 7.9 percent. Experimentally these low saturations could only be obtained by flooding the cores with nitrogen gas. When only flooding with brine the lowest S_{wi} obtained was 22 percent. This, combined with the fact that all the waterfloods were conducted on different core samples, makes it difficult to estimate accurately the true connate water saturation. What is clear is that this has significant impact on the predicted recoveries since the difference between S_{wi} and S_{wc} will add an additional water-wet component to the system, as already discussed for the fixed wettability cases. To quantify the effect we again matched the wetting states of 14 experimental core samples (Table 5.3) while keeping $S_{wc} = 0.22$ for cases where $S_{wi} > 0.22$, and $S_{wc} = S_{wi}$ for the rest. The wetting states were determined from the secondary oil flooding and tertiary water flooding cycles, allowing an infinite number of PVI. Predicted recoveries are shown in Figure 5.7, and there now is close agreement with the experimental results, especially at 3 pore volumes injected. These results are however not contradictory, but suggests that there is less of a correlation between maximum recovery and wetting state, than between maximum recovery and total amount of water-wet pore space during water flooding. From Figure 5.8 it would seem that maximum recovery occurs when about 10 percent of the effective pore space $(1 - S_{wc})$ is water-wet. The deviation seen at higher water-wet fractions is due to differences in how the water-wet elements are distributed on the pore-scale.

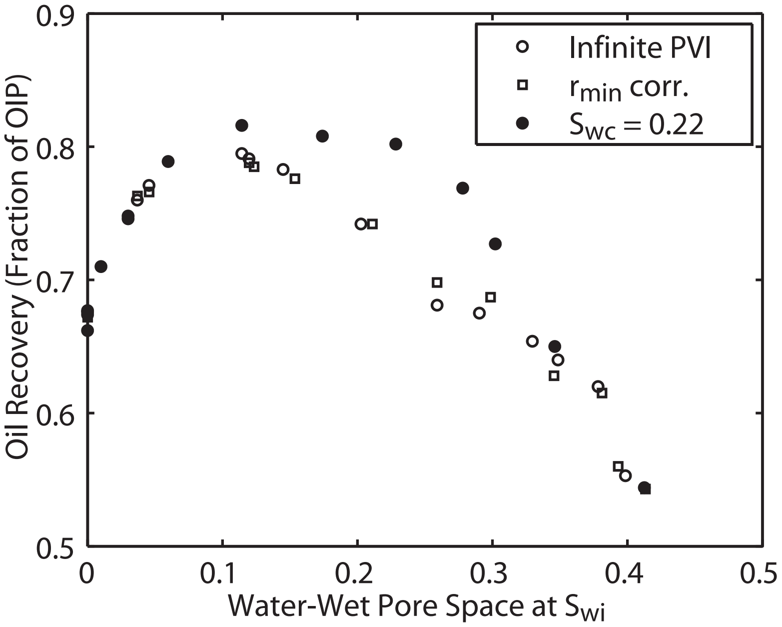

Figure 5.8: Relationship between oil recovery and the amount of effective pore space ($1 - S_{wc}$) that is water-wet when commencing water flooding (S_{wi}). The deviation between the cases at higher water-wet fractions is due to differences in how the water-wet elements are distributed on the pore-scale.

When $S_{wi} > S_{wc}$ the remaining water-filled elements will mostly be found in throats whereas if $S_{wi} = S_{wc}$ the water-wet elements are distributed in a mix of the smaller pores and throats. The pore-scale explanation for this trend is consistent with the behaviour illustrated in Figure 5.2. Maximum recovery will occur when the water relative permeability is low, something that occurs when there is a large number of separate water clusters. This can be the result of either $S_{wi} > S_{wc}$ or the oil-wet fraction being less than 1. The relative permeability and fractional water flow when oil recovery is maximized is shown in Figure 5.9 for the infinite PVI case and when $S_{wc} = 0.22$, corresponding to $S_{wi} = 0.18$ and 0.25 for the two cases respectively. The water relative permeabilities are both very low and similar in shape, resulting in high oil recovery.

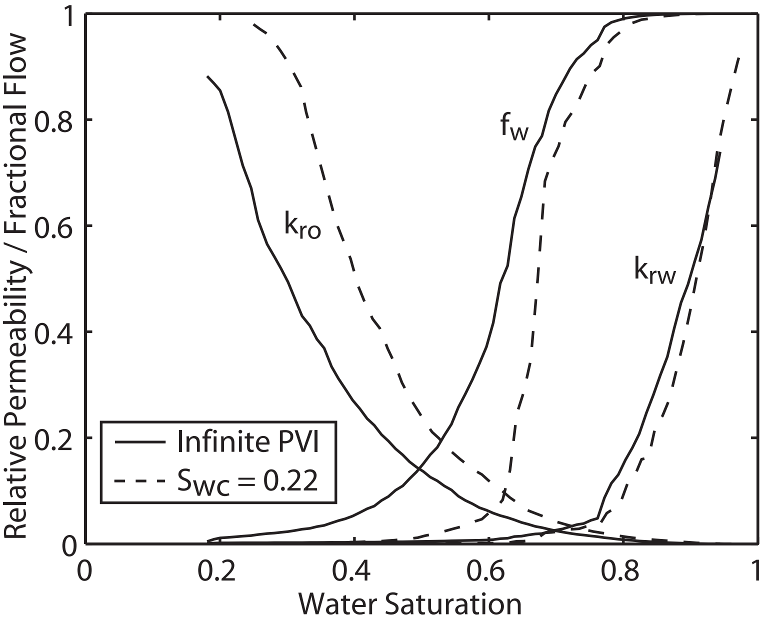

Figure 5.9: Relative permeability (k_r) and fractional water flow (f_w) when oil recovery is maximized. This will occur at $S_{wi} = 0.18$ for the infinite PVI case and $S_{wi} = 0.25$ when $S_{wc} = 0.22$. The water relative permeability is very similar in both cases, resulting in similar recoveries.

The calculated Amott water-oil index will also be significantly influenced by the choice of wettability hysteresis model (difference between advancing and receding contact angle). The Morrow [1975] model used, as illustrated in Figure 3.6, was developed using an ideal system. We will however not investigate this any further as it does not affect the overall understanding of the problem.

5.1.1 Field-scale implications

Due to capillary rise effects, initial water saturations might be considerably higher than the connate water saturation in the region above the oil-water contact, commonly referred to as the oil-water transition zone. When estimating reserves using finite difference reservoir simulation, relative permeability curves are needed for this zone, referred to as scanning curves ($S_{wi} > S_{wc}$). Empirical interpolation techniques are typically used for this [*Killough*, 1976; *Carlson*, 1981]. These models generally assume that the scanning curves lie between the bounding primary oil flooding and water flooding curves ($S_{wi} = S_{wc}$). However, from the last section it is clear that this is rarely the case. In a previous paper we compared field-scale oil recovery predictions when using different techniques to generate the scanning curves

[*Jackson et al.*, 2003]. Using pore-scale network modelling to generate the curves resulted in significantly higher prediction of overall recovery factor than when using empirical interpolation techniques. This is because in mixed-wet reservoirs maximum oil recovery is achieved when a significant portion of the pore space remain water-wet, something that is not captured by the currently used empirical models.

5.2 Mixed-wet intergranular carbonate

In the petroleum industry multiphase flow experiments are routinely performed on cores from hydrocarbon bearing reservoirs. Capillary pressure data are not usually available from steady-state measurements but rather found from centrifuge or mercury intrusion experiments. In both cases only pressures from the forced displacements are typically available. In this section we will use mercury-air capillary pressures to modify the network and then predict relative permeability. Though only available for the primary flooding cycle, this data has the benefit of not being influenced by wettability characterization issues as the mercury-air contact angle is generally assumed to be fixed at 140 degrees with an interfacial tension of 0.48 N/m.

The capillary pressure response of the network model was matched to experimental data for two samples of an intergranular carbonate using the same procedure that was described for the sand pack, and the results are shown in Figure 5.10. Both carbonate samples consisted of compacted, poorly sorted, peloidal grainstone. Since no spontaneous displacement data were available, the pore body size distribution was determined by maintaining the pore body to throat radius aspect ratio from the original Berea network. Since mercury will enter both micro and clay bound porosity, this method will not help in determining the connate water saturation. A realistic threshold radius is thus needed to determine what fraction of the pore space is accessible, effectively determining the minimum throat radius. Since no clay bound porosity is found in the samples a choice of about 0.1 μm would seem to be a realistic value in this case, resulting in connate water saturation of about 2 percent (Table 5.4). From the mercury intrusion data it is clear that the samples are fairly similar. The absolute permeability was predicted to be 1.60 and 1.28 mD for samples 1 and 2, compared to experimental values of 1.40 and 0.92 mD respectively.

Note that this is more than three orders of magnitude lower than the original network permeability, indicating that we have significantly altered the pore size distribution. These values are also tabulated in Table 5.5. No further parameters relating to the network were tuned for the subsequent flow predictions. Experimental primary oil flooding relative permeability data (only available for sample 1) will give some validation of the network modification process since the flow response is less affected by wettability, with the assumption that the rock is strongly water-wet. The predictions are in fairly good agreement with experimental data (Figure 5.11) suggesting that the modified network is representative of the rock. Fluid parameters used are given in Table 5.4.

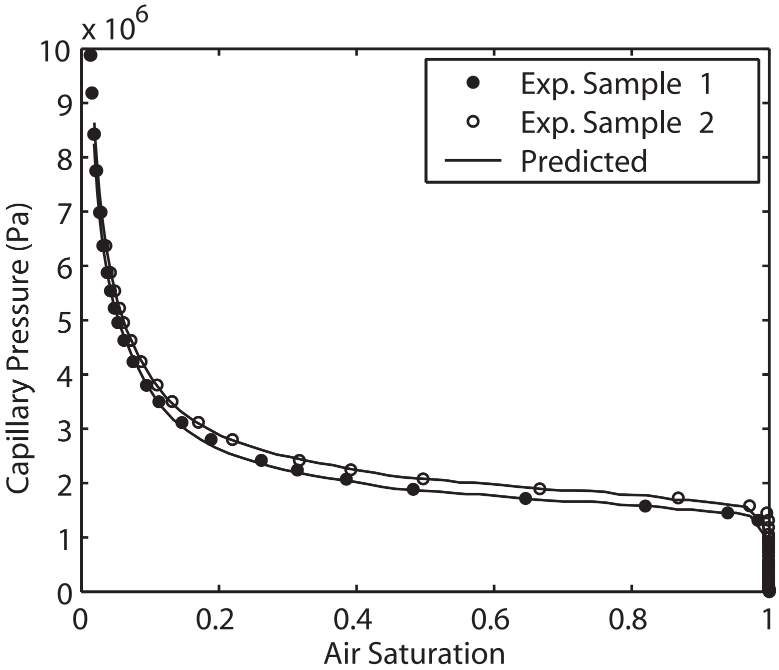

Figure 5.10: Comparison between experimental and matched mercury-air capillary pressure for two samples of intergranular carbonates.

Table 5.4: Fluid and rock properties used in predictions for mixed-wet intergranular carbonates.

Surface tension, σ (10^{-3} N/m)		29.9
Water viscosity, μ_w (10^{-3} Pa/s)		0.927
Oil viscosity, μ_o (10^{-3} Pa/s)		6.17
Porosity	Sample 1	0.264
	Sample 2	0.241
Initial Water Saturation, S_{wi}	Sample 1	0.181
	Sample 2	0.220
Connate Water Saturation, S_{wc}		0.021
Water-wet contact angles, θ_i (deg)		25 – 65
Oil-wet contact angles, θ_i (deg)		80 – 82
Oil-wet fraction by pore volume	Sample 1 and 2	0.68
	Sample 2 (less oil-wet)	0.65

Table 5.5: Experimental and predicted values for mixed-wet intergranular carbonates for absolute permeability and mean residual oil saturation following water flooding with associated standard deviation (sd).

	Experimental		Predicted		
Sample	K (mD)	S_{or}	K (mD)	S_{or}	S_{or} (sd)
1	1.40	0.30	1.60	0.30	0.01
2	0.92	0.42	1.28	0.36	0.02
2 (less oil-wet)	0.92	0.42	1.28	0.41	0.01

Table 5.6: Experimental and predicted values for mixed-wet intergranular carbonates for Amott wettability indices with associated standard deviation (sd).

	Experimental		Predicted			
Sample	I_w	I_o	I_w	I_w (sd)	I_o	I_o (sd)
1	0.50	0.00	0.48	0.01	0.00	0.00
2	0.74	0.00	0.55	0.03	0.00	0.00
2 (less oil-wet)	0.74	0.00	0.67	0.03	0.00	0.00

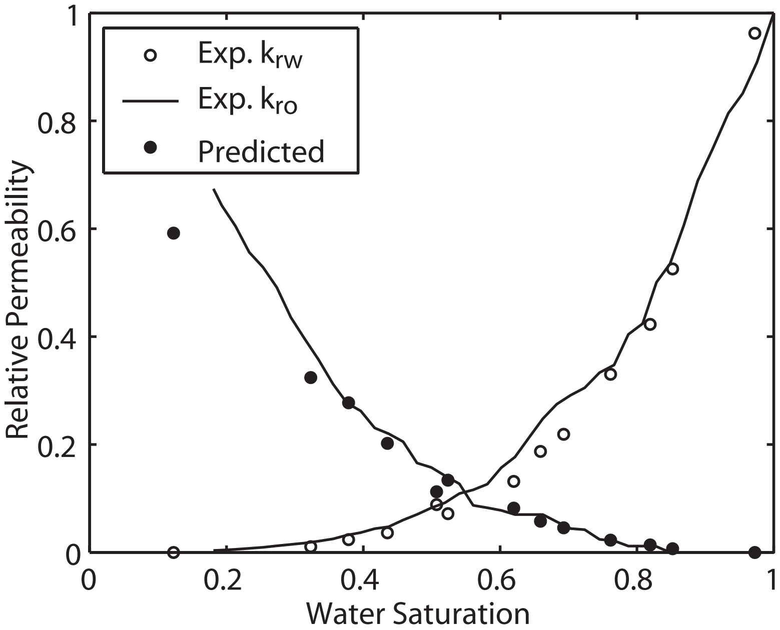

Figure 5.11: Comparison between experimental and predicted primary oil flooding relative permeability for a mixed-wet intergranular carbonate.

Water flooding adds the additional complexity of wettability characterization. The Amott water index is broadly controlled by adjusting the oil-wet fraction, whereas the residual oil saturation and oil index is more affected by the distribution of intrinsic contact angles in the oil-wet pores. A distribution towards strongly oil-wet conditions will result in low residual oil saturation as oil layers remain stable, allowing oil to escape even at low saturation. Conversely, a distribution towards more neutral conditions will result in more residual oil, as well as a lower oil index since a higher proportion of the pores will have receding contact angles less than 90°. The distribution of contact angles in the water-wet fraction has less influence on the predicted results, though a distribution towards more strongly water-wet conditions will result in poorer oil connectivity as snap-off events become more dominant. A flowchart of the outlined methodology is shown in Figure 5.12.

Using Cryo-scanning electron microscopy (Cryo-SEM) it is possible to visualize the distribution of oil and water at the pore-scale. Based on these studies there is some justification for suggesting that the pore size and geometry is important in determining which pores become oil-wet in carbonates [*Fassi-Fihri et al.*, 1991]. Hence, we assume that the smallest oil-filled pores following primary oil flooding become oil-wet [*Kovscek et al.*, 1993].

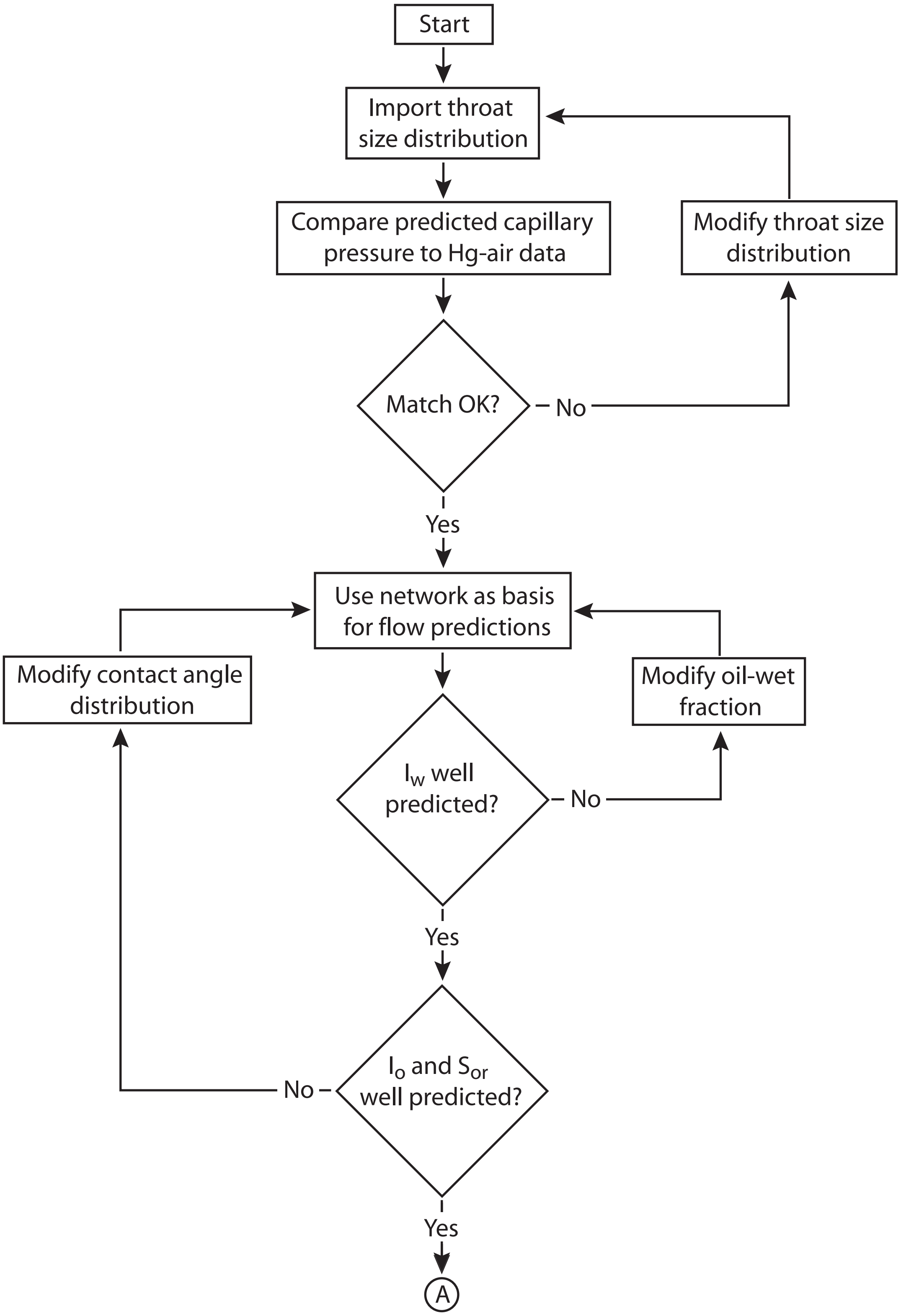

Figure 5.12: Flowchart for relative permeability predictions.

Both carbonate samples were from an oil-water transition zone. Sample 2 was taken lower in the zone than sample 1 and thus had a higher initial water saturation, 22 percent compared to 18 percent. It also exhibits more water-wet characteristics, higher residual oil and lower Amott water index (Table 5.5 and 5.6), than sample 1. This is a very similar scenario to what was investigated in the last section, where the influence of initial water saturation on wettability and production characteristics was discussed. However, rather than predicting oil recoveries we will now directly investigate the influence on relative permeability. Experimental centrifuge data from sample 1 was used to characterise the wettability, as shown in Figure 5.13 (a). Though the absolute capillary pressures were not that well matched, which is not surprising considering the uncertainties in both the wettability hysteresis model and the experimental centrifuge data, both residual oil saturation and Amott wettability indices were well matched as evident from Table 5.5 and 5.6. This same wetting condition was subsequently used for sample 2. The higher initial water saturation did indeed make the predicted wetting condition more water-wet, as shown in Figure 5.13 (b), but the experimental values were somewhat under-predicted. This is, however, consistent with the conclusions from the last section where we noted that the higher initial water saturation would probably reduce the pore space fraction becoming oil-wet due to the lower capillary pressure reached during primary oil-flooding. Reducing the oil-wet fraction from 0.68 to 0.65, while keeping the same distributions of contact angles, significantly improved the match with Amott wettability indices and residual oil saturation, as shown in Figure 5.13 (c) and tabulated in Table 5.5 and 5.6.

The predictions of relative permeability are shown in Figure 5.14. While the predictions for sample 2, Figure 5.14 (c), are excellent, both the water and oil relative permeability for sample 1 are not that well predicted, Figure 5.14 (a), with both being under-predicted. The most obvious reason for this would be that the network used, originally constructed from a Berea sandstone, is in fact not representative of the carbonate samples. This is supported by investigating the back scattered electron (BSE) images shown in Figure 5.15. The grain size distribution is clearly much more heterogeneous than in a Berea sandstone with the images shown not covering a representative elementary volume (REV). The network used for the predictions consists of about 12,300 pores, roughly equivalent to a 23^3 regular network, something that, from visual inspection of the BSE images, is unlikely to be larger than the REV of these carbonate samples. However, since the steady state flow experiments were conducted on much larger samples, and the original network is much larger than the REV of a Berea sandstone, the effects are not observed in the experimental or predicted results. The higher level of heterogeneity in the carbonates will result in not just under-estimation of the correlation length, but also in a too low average connection number and too low size contrasts between pore bodies and throats. The fact that the network does not capture the essential topological features of these carbonate samples, does significantly reduce the confidence one can attach to the predictions. However, if network topology and connectivity were the main reasons for the poor predictions, one would also expect this to influence the primary oil flooding results, which is not the case. Also, samples 1 and 2 would appear to be morphologically very similar, evident from both the mercury intrusion experiments as well as the BSE images, and water flood predictions of sample 2 are considerably better. These predictions were performed with a distribution of intrinsic contact angles in the oil-wet part between 80 and 82 degrees, corresponding to advancing contact angles between 116 and 120 degrees. This distribution was found by following the methodology illustrated in Figure 5.12, but it would seem to be rather narrow and low when compared to distributions found in similar carbonates. A final possible reason for the discrepancy in water flooding predictions can be the influence of viscous forces. Although both samples were found to contain negligible vuggy porosity, the range of pore sizes is large. Our assumption of complete capillary dominance might therefore not be valid in the larger pores, something that would affect the filling sequence of the network. To conclude this section, we have shown promising relative permeability predictions of two intergranular carbonate samples. However, it is uncertain whether a network originally constructed to represent a sandstone can sufficiently capture the essential topological features of these heterogeneous carbonate samples. It is possible that the predictions can be improved by using information directly obtained from the BSE images, like for example the size aspect ratio between pore bodies and throats.

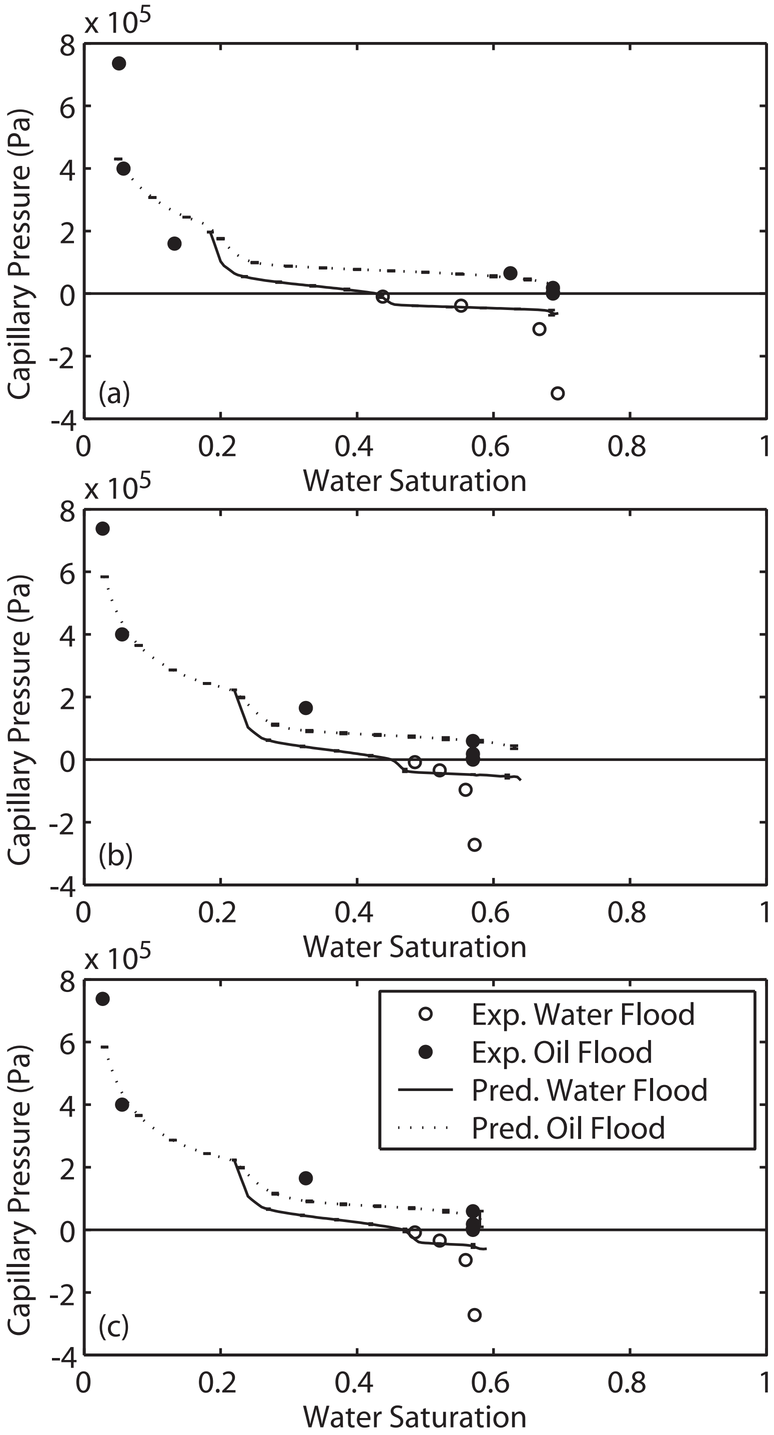

Figure 5.13: Comparison between experimental and predicted water-oil capillary pressure for secondary water and oil flooding cycles. (a) Sample 1 was used to characterise the wettability. (b) Using the same wetting condition for sample 2 as was found from sample 1 results in too oil-wet conditions. (c) Reducing the oil-wet fraction for sample 2 improves predictions.

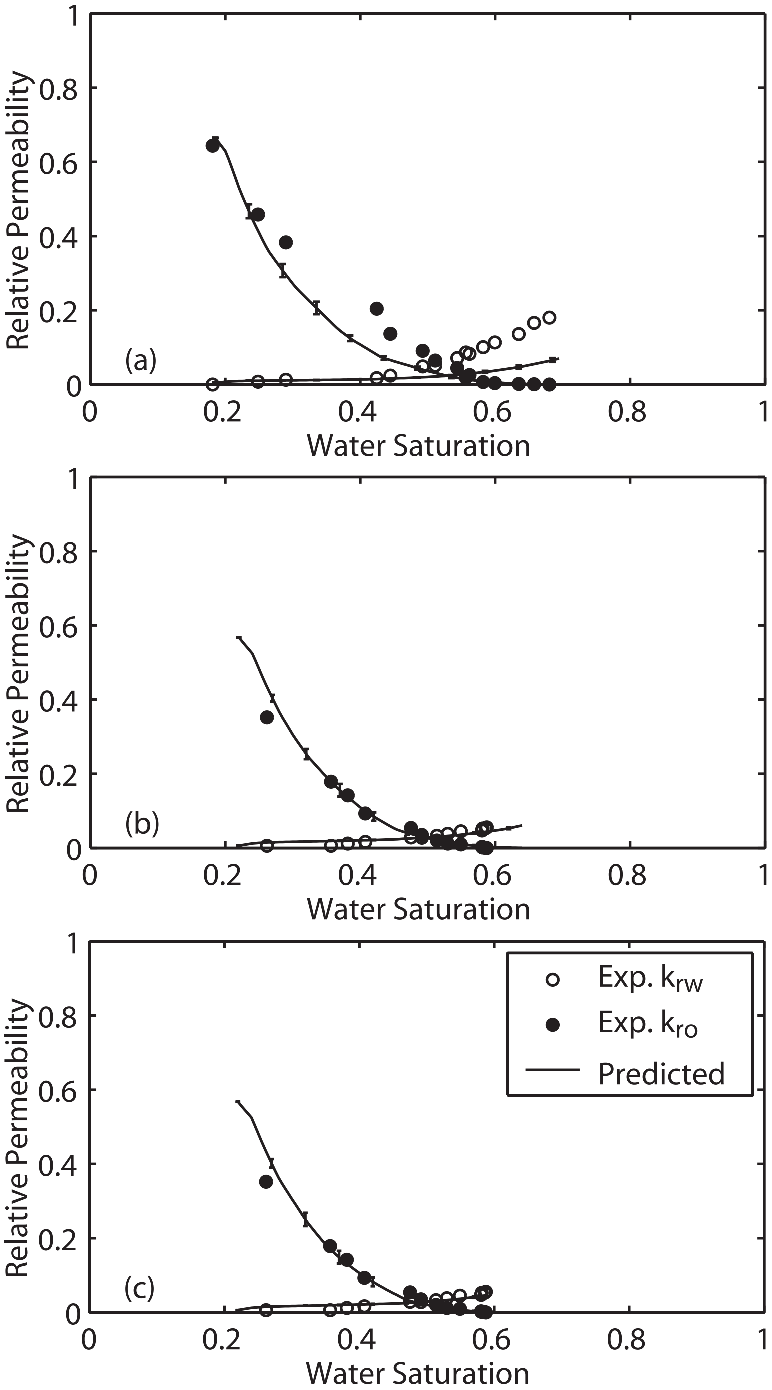

Figure 5.14: Comparison between experimental and predicted water flooding relative permeability for sample 1 (a), sample 2 (b) and sample 2 with a lower oil-wet fraction (c).

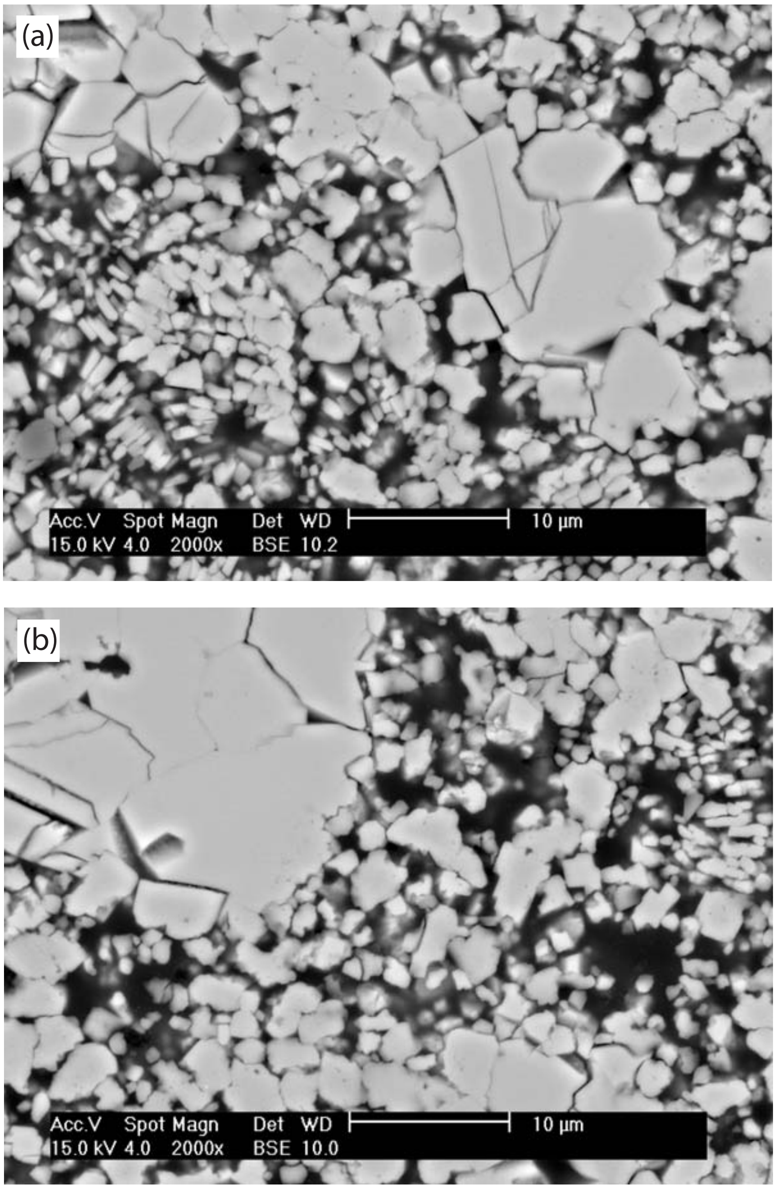

Figure 5.15: Back scattered electron (BSE) images of samples 1 (a) and 2 (b). These images suggest that the carbonate samples have a much more heterogeneous grain size distribution than would be expected in a Berea sandstone, raising doubt whether the network used in fact representative of the carbonate samples.

5.3 Mixed-wet reservoir sandstone

This dataset was based on a consolidated sandstone, taken from an oil-bearing reservoir. The same procedure of using primary mercury intrusion experiment to modify the network while applying a threshold to determine likely connate water saturation was used. A choice of 1 μm would seem to be a realistic value in this case, resulting in $S_{wc} = 0.11$. The absolute permeability was predicted to be 814 mD which compares well to the experimental value of 750 mD. Mercury intrusion and steady state flow experiments are not conducted on the same cores, hence the connate water saturation might be significantly different. The non-accessible porosity is subsequently adjusted such that S_{wc} in the network model is consistent with experimental data.

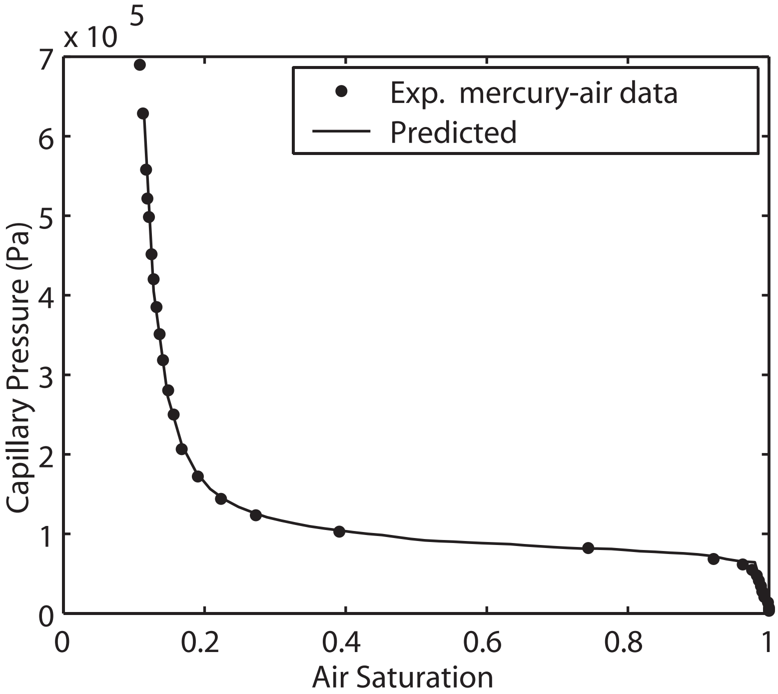

Figure 5.16: Comparison between experimental and matched mercury-air capillary pressure for a reservoir sandstone. Mercury will enter both micro and clay bound porosity. This porosity is not explicitly included in the network model and as a result capillary pressures corresponding to $S_w < 0.11$ will not be matched.

Though the Cryo-SEM studies found that pore size and geometry was important in determining which pores become oil-wet in carbonates, this is not necessarily the case for sandstones [*Fassi-Fihri et al.*, 1991; *Durand and Rosenberg*, 1998]. It was found that the presence of clay minerals, in particular kaolinite, was far more likely to make a pore oil-wet than its size. The distribution of these clay minerals might very well not be related to pore size. In this section we will therefore test three approaches to assigning wettability. In addition to the previous approach, where the smallest pores become oil-wet, we will also make the largest pores oil-wet. Finally we will assign oil-wet elements in spatially correlated patches. This is done by randomly selecting some oil-invaded pore regardless of size. All oil-invaded pores within a defined correlation length are then made oil-wet. Oil-filled throats connected to oil-wet pores are also made oil-wet. This process continues until a defined oil-wet fraction is achieved.

Following aging the sandstone exhibited mixed-wet characteristics with an Amott water index of 0.55, indicating that about half the pore space had become oil-wet. No oil index was measured. Fluid and rock properties used in the predictions are given in Table 5.7. In Figure 5.17 the water distribution in sections of the network model at $S_w = 0.5$ is shown for the different wettability characterization schemes, with the corresponding relative permeability curves shown in Figure 5.18. The saturation shown is towards the end of the spontaneous displacement and most of the remaining oil-filled elements are thus either trapped or oil-wet. In both cases where oil-wet elements are correlated to their inscribed radius (indicated as r_{min} and r_{max}) there is little continuity in completely water-filled elements. As water repeatedly has to flow through layers in order to connect from inlet to outlet, the water relative permeability will stay very low until water-filled elements start to connect across the model. This behaviour is very similar to that described in the previous section when $S_{wi} > S_{wc}$. In the case where the smallest pores become oil-wet, the oil relative permeability is reduced very quickly as the larger pores, which are also the most conductive, are filled by water early in the displacement. Spatially correlating the oil-wet elements, with a correlation length of about 7 pores, creates more continuity through the oil-wet pores, making it more likely for water to be able to flow from inlet to outlet in completely water-filled elements. The result is a more gradual increase in water relative permeability, consistent with the experimental data. There will necessarily be more statistical variation between the different realizations when using a spatial correlation approach, as evident from the larger error bars in Figure 5.18 when compared to previous figures. All the predicted Amott water indices are consistent with the experimental values, Table 5.8. There is more variation in the predicted oil indices, as there were no experimental data to compare against.

Table 5.7: Fluid and rock properties used in predictions for a mixed-wet reservoir sandstone.

Surface tension, σ (10^{-3} N/m)		30.0
Water viscosity, μ_w (10^{-3} Pa/s)		1.05
Oil viscosity, μ_o (10^{-3} Pa/s)		1.39
Porosity		0.27
Connate water saturation		0.34
Water-wet contact angles, θ_i (deg)		0 – 60
Oil-wet fraction by pore volume	r_{min} correlation	0.53
	r_{max} correlation	0.63
	spatial correlation	0.43
Oil-wet contact angles, θ_i (deg)	r_{min} correlation	70 – 110
	r_{max} correlation	140 – 180
	spatial correlation	100 – 160

Table 5.8: Predicted Amott wettability indices for a mixed-wet reservoir sandstone.

	Water		Oil	
	Amott Index	Standard deviation	Amott Index	Standard deviation
Experimental	0.55	—	—	—
r_{max} correlation	0.51	0.01	0.46	0.01
r_{min} correlation	0.54	0.01	0.00	0.00
Spatial correlation	0.56	0.08	0.32	0.08

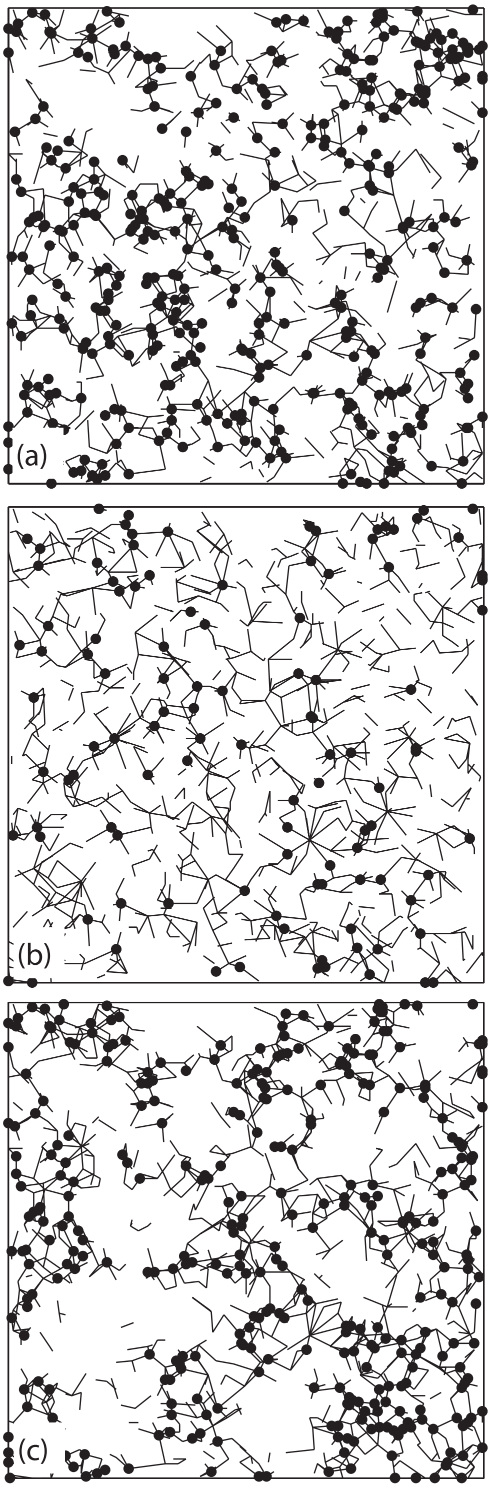

Figure 5.17: Distribution of water-filled elements during water flooding at $S_w = 0.5$ with oil-wet elements correlated by (a) maximum pore radius, (b) minimum pore radius or (c) spatial correlation. The saturation shown is towards the end of spontaneous displacement. Since water-wet elements are generally filled first, phase connectivity during water flooding is improved if there is spatial correlation in the oil-wet elements.

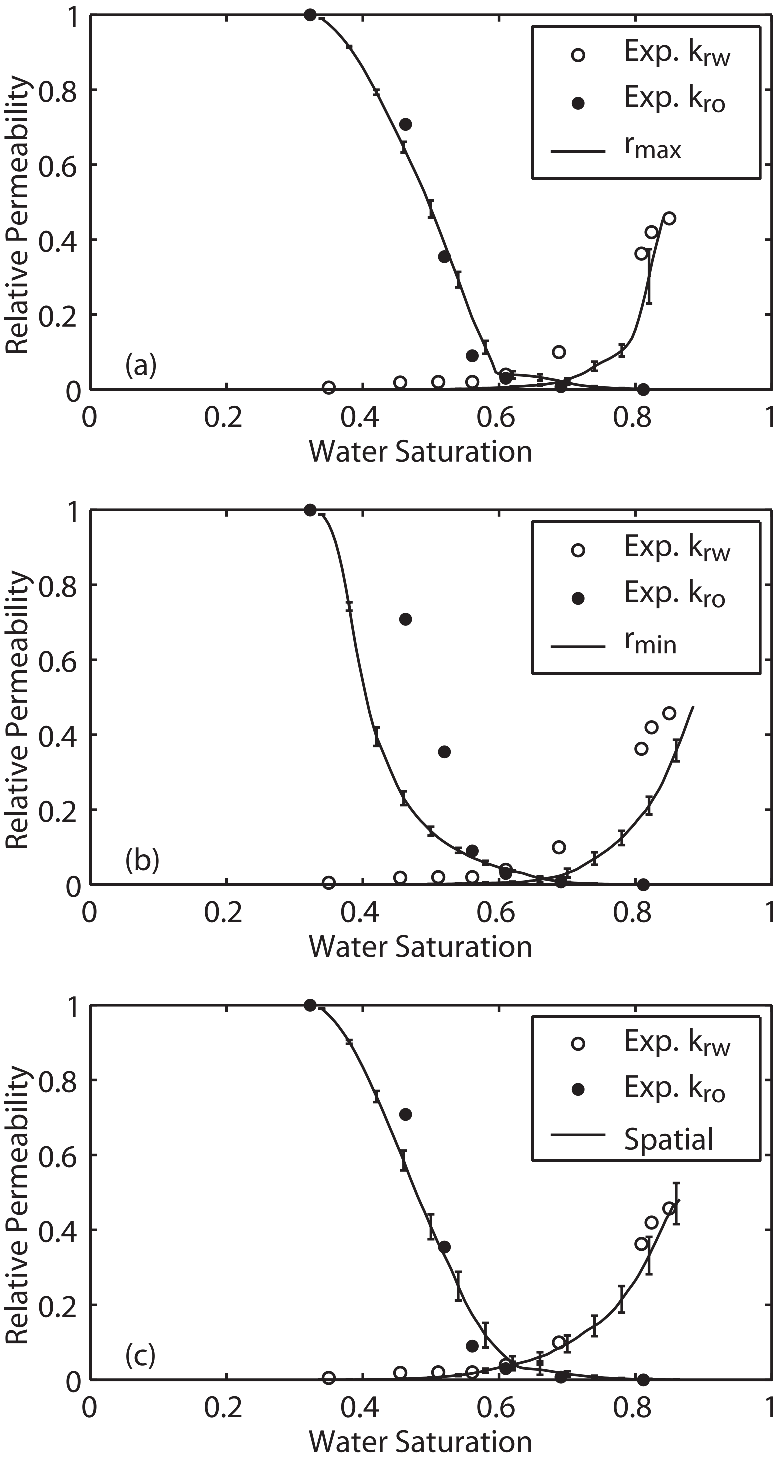

Figure 5.18: Comparison between experimental and predicted relative permeability for a reservoir sandstone. The experimental wetting state is fairly well predicted in all cases and the only difference between the cases is how wettability is characterized on the pore-scale. (a) The larger pores become preferentially oil-wet. (b) The smaller pores become preferentially oil-wet. (c) The oil-wet pores are spatially correlated.

5.4 Oil-wet reservoir sandstone

The final sandstone dataset had steady-state relative permeabilities measured on two core samples with experimental permeabilities of 248 and 328 mD. Since no mercury injection data were available, primary oil flooding capillary pressure had to be used for the network modification process, Figure 5.19. This was a centrifuge experiment performed on a different core sample from those used for relative permeability measurements, hence the difference in connate water saturation. Uncertainties in interfacial tension and contact angles meant that no reliable estimate of absolute permeability could be made. Rather than being strongly water-wet during primary oil flooding, the core exhibited mixed-wet characteristics with Amott water and oil indices of 0.33 and 0. Though this is consistent with a uniform distribution of receding contact angles between 10 and 40 degrees, there still is quite a large degree of uncertainty in the exact wetting state.

Following wettability alteration the core exhibited mainly oil-wet characteristics with Amott water and oil indices of 0.00 and 0.14. The low residual oil saturation is also an indication of an oil-wet system, a result of oil being able to escape through layers. The comparison between experimental and predicted relative permeability is good, Figure 5.19 (b). The predictions were made with $S_{wi} = 0.03$ and intrinsic contact angles distributed at random uniformly between 70 and 122 degrees.

The statistical fluctuations between realizations are less than for mixed-wet samples as all pores contacted by oil are assumed to be oil-wet. The predicted Amott indices of 0.00 and 0.15, with standard deviations of 0 and 0.01, for water and oil respectively, are also in good agreement with experimental values. Fluid and rock properties are given in Table 5.9.

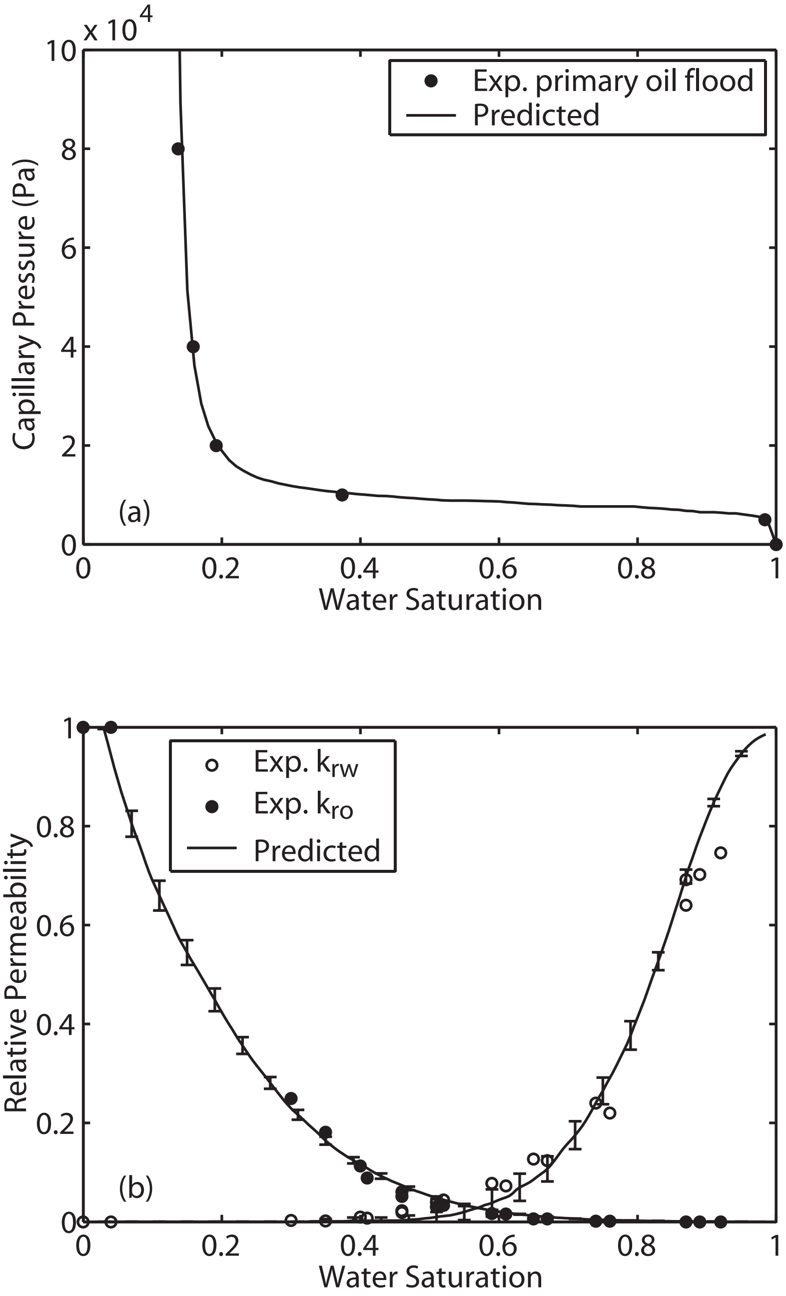

Figure 5.19: Comparison between predicted and experimental properties for an oil-wet reservoir sandstone. (a) Centrifuge primary oil flooding capillary pressures were used to modify the network. (b) Predicted water flooding relative permeability are compared to experimental steady-state data. The low residual oil saturation is a good indication oil-wet characteristics.

Table 5.9: Fluid and rock properties used in predictions for an oil-wet reservoir sandstone.

Surface tension, σ (10^{-3} N/m)	51.8
Water viscosity, μ_w (10^{-3} Pa/s)	1.00
Oil viscosity, μ_o (10^{-3} Pa/s)	0.29
Porosity	0.15
Connate water saturation	0.00
Initial water saturation	0.03
Contact angles during primary oil flooding, θ_r (deg)	10 – 40
Contact angles during water flooding, θ_i (deg)	70 – 122

Chapter 6

Conclusions

The aim of this work is not simply to match experiments, but to use easily acquired data to predict difficult to measure properties such as relative permeability. The confidence one can attach to these predictions is directly related to the three main components of pore-scale network modelling that we have focused on in this work – the geometric properties of the network such as topology and pore size distribution, the pore-scale physics, and the wettability characterization.

A state of the art pore-scale network model was developed, that combined topologically disordered networks that represent real systems with detailed displacement mechanisms for any sequence of water and oil flooding for any wettability. Though most of the implemented pore-scale physics has already been described in the literature, a new correlation for oil layer conductance was proposed that is more accurate than previously published work. The correlation was validated by an extensive series of finite element computations.

The implementation of the pore-scale network model was validated using experimental data from water-wet Berea sandstone and a network topology specifically generated to represent this sandstone. The predictions of relative permeability were not only in excellent agreement with experimental data but also agreed well with those presented by other authors [*Piri and Blunt*, 2002; *Øren and Bakke*, 2003]. The other water-wet dataset used, a sand-pack, was also very well predicted, further increasing our confidence in the presented pore-scale network model.

By developing a methodology combining realistic network topology with network properties tuned to experimental data such as mercury injection capillary pressure, we successfully predicted flow properties for several datasets including a sand pack, a reservoir carbonate and two reservoir sandstones while using a network initially developed to represent Berea sandstone. During primary oil flooding relative permeability is controlled by the network geometry and the pore-scale displacement processes and wettability is unambiguous. Predictions of both absolute permeability and primary oil flooding relative permeability were very good, suggesting this methodology is sufficient to predict single and multiphase properties for a wide range of porous media.

During water flooding relative permeability is strongly affected by wettability. The trend in oil recovery from a series of mixed-wet Berea sandstone cores [*Jadhunandan and Morrow*, 1995] was well predicted by closely reproducing the experimental conditions like S_{wi} and saturation history. The focus of this work is not so much on obtaining a quantitative match with the experiments, but rather on understanding the pore-scale processes that produce these surprising experimental recovery trends. However, by modifying our assumptions about the experimental conditions, a quantitative match was obtained.

Wettability characterization for mixed-wet systems is perhaps the most uncertain part of what has been investigated in this work. Though theoretical models have been suggested in the literature [*Kovscek et al.*, 1993], these do not always satisfactorily describe what is observed experimentally, both in terms of observed transport properties and from pore-scale imaging [*Fassi-Fihri et al.*, 1991; *Durand and Beccat*, 1998]. In the case of the mixed-wet sandstone samples we suggest that good predictions require the oil-wet pores to be spatially correlated. This ensured that the predicted relative permeability was in better agreement with experimental data than when correlating the oil-wet pores based on size only.

6.1 Applications and future direction

With the outlined methodology of first tuning a realistic network and subsequently predicting the flow performance, constrained by commonly available experimental data, we have shown how pore-scale network modelling can become a very useful tool in analyzing multiphase flow in porous media. By predicting experimental measurements we gain useful insight into pore-scale processes that might not be immediately obvious from just examining the data. By constraining predictions to a defined set of measurements, the predictions will also serve as quality control to the experiments. For this work we have only used a single network constructed from Berea sandstone. To improve confidence in predictions from a wider range of rocks it would be preferable to have a library of networks representing different rock types. The network that most closely matches the geological structure of the sample of interest would then be chosen for modelling studies.

An even more promising application of predictive pore-scale network modelling is where experimental data is not available or difficult to obtain. Available experimental data can be used to anchor the model to a specific core condition. In the reservoir these conditions might, however, vary considerably. Assessing the impact these variations have on relative permeability can be done more reliably using network modelling than extrapolation from experimental data, particularly for situations where there are wettability variations in the reservoir, or three-phase flow [*Piri and Blunt*, 2002]. In a previous paper [*Jackson et al.*, 2003] we used network modelling to generate relative permeability curves for a transition zone near the oil-water contact. These were subsequently used in a full-field reservoir simulation model and the predicted oil recovery was significantly different from that obtained using more traditional interpolation techniques.

Bibliography

Adler, P. M., and J. F. Thovert, Real porous media: Local geometry and macroscopic properties, *Applied Mechanics Reviews*, *51*, 537-585, 1998.

Al-Futaisi, A., and T. W. Patzek, Impact of wettability alteration on two-phase flow characteristics of sandstones: A quasi-static description, *Water Resources Research*, *39*, 1042, doi:1010.1029/2002WR001366, 2003.

Anderson, W. G., Wettability Literature Survey - Part 1: Rock-Oil-Brine Interactions and the Effects of Core Handling on Wettability, *Journal of Petroleum Technology*, *38*, 1125-1144, 1986a.

Anderson, W. G., Wettability Literature Survey - Part 2: Wettability Measurement, *Journal of Petroleum Technology*, *38*, 1246-1262, 1986b.

Bakke, S., and P. E. Øren, 3-D pore-scale modelling of sandstones and flow simulations in the pore networks, *SPE Journal*, *2*, 136-149, 1997.

Biswal, B., C. Manwart, R. Hilfer, S. Bakke, and P. E. Øren, Quantitative analysis of experimental and synthetic microstructures for sedimentary rock, *Physica A: Statistical Mechanics and its Applications*, *273*, 452-475, 1999.

Blunt, M., and P. King, Macroscopic Parameters from Simulations of Pore Scale Flow, *Physical Review A*, *42*, 4780-4787, 1990.

Blunt, M., and P. King, Relative Permeabilities from 2-Dimensional and 3-Dimensional Pore-Scale Network Modeling, *Transport in Porous Media*, *6*, 407-433, 1991.

Blunt, M. J., Effects of heterogeneity and wetting on relative permeability using pore level modeling, *SPE Journal*, *2*, 70-87, 1997a.

Blunt, M. J., Pore level modeling of the effects of wettability, *SPE Journal*, *2*, 494-510, 1997b.

Blunt, M. J., Physically-based network modeling of multiphase flow in intermediate-wet porous media, *Journal of Petroleum Science and Engineering*, *20*, 117-125, 1998.

Blunt, M. J., and H. Scher, Pore-Level Modeling of Wetting, *Physical Review E*, *52*, 6387-6403, 1995.

Bryant, S., and M. Blunt, Prediction of Relative Permeability in Simple Porous-Media, *Physical Review A*, *46*, 2004-2011, 1992.

Bryant, S. L., P. R. King, and D. W. Mellor, Network Model Evaluation of Permeability and Spatial Correlation in a Real Random Sphere Packing, *Transport in Porous Media*, *11*, 53-70, 1993a.

Bryant, S. L., D. W. Mellor, and C. A. Cade, Physically Representative Network Models of Transport in Porous-Media, *AIChE Journal*, *39*, 387-396, 1993b.

Buckley, J. S., Y. Liu, and S. Monsterleet, Mechanisms of wetting alteration by crude oils, *SPE Journal*, *3*, 54-61, 1998.

Carlson, F. M., Simulation of relative permeability hysteresis to the non-wetting phase, proceedings of the 1981 SPE Annual Technical Conference and Exhibition, SPE 10157, Soc. of Petroleum Engineers, San Antonio, 1981.

Chatzis, I., and F. A. L. Dullien, Modelling pore structures by 2-D and 3-D networks with application to sandstones, *Journal of Canadian Petroleum Technology*, *16*, 97-108, 1977.

Chen, S., and G. D. Doolen, Lattice Boltzmann method for fluid flows, *Annual Review of Fluid Mechanics*, *30*, 329-364, 1998.

Coelho, D., J. F. Thovert, and P. M. Adler, Geometrical and transport properties of random packings of spheres and aspherical particles, *Physical Review E*, *55*, 1959-1978, 1997.

Coker, D. A., S. Torquato, and J. H. Dunsmuir, Morphology and physical properties of Fontainebleau sandstone via a tomographic analysis, *Journal of Geophysical Research-Solid Earth*, *101*, 17497-17506, 1996.

Combes, R., M. Robin, G. Blavier, M. Aidan, and F. Degreve, Visualization of imbibition in porous media by environmental scanning electron microscopy: application to reservoir rocks, *Journal of Petroleum Science and Engineering*, *20*, 133-139, 1998.

Delerue, J. F., and E. Perrier, DXSoil, a library for 3D image analysis in soil science, *Computers & Geosciences*, *28*, 1041-1050, 2002.

Delerue, J. P., E. Perrier, Z. Y. Yu, and B. Velde, New algorithms in 3D image analysis and their application to the measurement of a spatialized pore size distribution in soils, *Physics and Chemistry of the Earth, Part A: Solid Earth and Geodesy*, *24*, 639-644, 1999.

Deutsch, C. V., and A. G. Journel, *GSLIB Geostatistical Software Library and User's Guide*, 2 edition, Oxford University Press, Oxford, 1998.

Dias, M. M., and D. Wilkinson, Percolation with Trapping, *Journal of Physics A: Mathematical and General*, *19*, 3131-3146, 1986.

Dillard, L. A., and M. J. Blunt, Development of a pore network simulation model to study nonaqueous phase liquid dissolution, *Water Resources Research*, *36*, 439-454, 2000.

Dixit, A. B., J. S. Buckley, S. R. McDougall, and K. S. Sorbie, Empirical Measures of Wettability in Porous Media and the Relationship between Them Derived From Pore-Scale Modelling, *Transport in Porous Media*, *40*, 27-54, 2000.

Dixit, A. B., S. R. McDougall, and K. S. Sorbie, Pore-level investigation of relative permeability hysteresis in water-wet systems, proceedings of the 1997 SPE International Symposium on Oilfield Chemistry, SPE 37233, Soc. of Petroleum Engineers, Houston, 1997.

Dixit, A. B., S. R. McDougall, and K. S. Sorbie, Analysis of relative permeability hysteresis trends in mixed-wet porous media using network models, proceedings of the 11th Symposium on Improved Oil Recovery, Soc. of Petroleum Engineers, Tulsa, 1998.

Dixit, A. B., S. R. McDougall, K. S. Sorbie, and J. S. Buckley, Pore-scale modeling of wettability effects and their influence on oil recovery, *SPE Reservoir Evaluation & Engineering*, *2*, 25-36, 1999.

Dullien, F. A. L., *Porous media: fluid transport and pore structure*, 2nd edition, Academic Press, San Diego, 1992.

Dullien, F. A. L., C. Zarcone, I. F. Macdonald, A. Collins, and R. D. E. Bochard, The Effects of Surface-Roughness on the Capillary-Pressure Curves and the Heights of Capillary Rise in Glass Bead Packs, *Journal of Colloid and Interface Science*, *127*, 362-372, 1989.

Dunsmuir, J. H., S. R. Ferguson, K. L. D'Amico, and J. P. Stokes, X-ray microtomography. A new tool for the characterization of porous media, proceedings of the 1991 SPE Annual Technical Conference and Exhibition, SPE 22860, Soc. of Petroleum Engineers, Dallas, 1991.

Durand, C., and P. Beccat, Use of XPS for reservoir sandstone wettability evaluation. Application to kaolinite and illite, *Journal of Petroleum Science and Engineering*, *20*, 259-265, 1998.

Durand, C., and E. Rosenberg, Fluid distribution in kaolinite- or illite-bearing cores: cryo-SEM observations versus bulk measurements, *Journal of Petroleum Science and Engineering*, *19*, 65-72, 1998.

Dury, O., Organic pollutants in unsaturated soils: Effect of butanol as model contaminant on phase saturation and flow characteristics of a quartz sand packing, Ph.D. thesis, Swiss Federal Institute of Technology, Zürich, Switzerland, 1997.

Dury, O., U. Fischer, and R. Schulin, Dependence of hydraulic and pneumatic characteristics of soils on a dissolved organic compound, *Journal of Contaminant Hydrology*, *33*, 39-57, 1998.

Fassi-Fihri, O., M. Robin, and E. Rosenberg, Wettability studies at the pore level. A new approach by the use of Cryo-Scanning Electron Microscopy, proceedings of the 1991 SPE Annual Technical Conference and Exhibition, SPE 22596, Soc. of Petroleum Engineers, Dallas, 1991.

Fatt, I., The network model of porous media I. Capillary pressure characteristics, *Trans AIME*, *207*, 144-159, 1956a.

Fatt, I., The network model of porous media II. Dynamic properties of a single size tube network, *Trans AIME*, *207*, 160-163, 1956b.

Fatt, I., The network model of porous media III. Dynamic properties of networks with tube radius distribution, *Trans AIME*, *207*, 164-181, 1956c.

Fenwick, D. H., and M. J. Blunt, Network modeling of three-phase flow in porous media, *SPE Journal*, *3*, 86-97, 1998.

Fischer, U., and M. A. Celia, Prediction of relative and absolute permeabilities for gas and water from soil water retention curves using a pore-scale network model, *Water Resources Research*, *35*, 1089-1100, 1999.

Gunstensen, A. K., and D. H. Rothman, Lattice-Boltzmann Studies of Immiscible 2-Phase Flow through Porous-Media, *Journal of Geophysical Research-Solid Earth*, *98*, 6431-6441, 1993.

Hazlett, R. D., S. Y. Chen, and W. E. Soll, Wettability and rate effects on immiscible displacement: Lattice Boltzmann simulation in microtomographic images of reservoir rocks, *Journal of Petroleum Science and Engineering*, *20*, 167-175, 1998.

Hilfer, R., Geometric and Dielectric Characterization of Porous-Media, *Physical Review B*, *44*, 60-75, 1991.

Hilfer, R., Local Porosity Theory and Stochastic Reconstruction for Porous Media, *in Lecture Notes in Physics,* vol. 554, edited by K. R. Mecke and D. Stoyan, Springer-Verlag, Berlin, 2000.

Hilfer, R., and C. Manwart, Permeability and conductivity for reconstruction models of porous media, *Physical Review E*, *64*, doi:10.1103/PhysRevE.1164. 021304, 2001.

Hilpert, M., R. Glantz, and C. T. Miller, Calibration of a pore-network model by a pore-morphological analysis, *Transport in Porous Media*, *51*, 267-285, 2003.

Hui, M.-H., and M. J. Blunt, Effects of wettability on three-phase flow in porous media, *Journal of Physical Chemistry B*, *104*, 3833-3845, 2000.

Jackson, M. D., P. H. Valvatne, and M. J. Blunt, Prediction of wettability variation and its impact on flow using pore- to reservoir-scale simulations, *Journal of Petroleum Science and Engineering*, *39*, 231-246, 2003.

Jadhunandan, P. P., and N. R. Morrow, Effect of Wettability on Waterflood Recovery for Crude-Oil Brine Rock Systems, *SPE Reservoir Engineering*, *10*, 40-46, 1995.

Jerauld, G. R., J. C. Hatfield, L. E. Scriven, and H. T. Davis, Percolation and Conduction on Voronoi and Triangular Networks - a Case-Study in Topological Disorder, *Journal of Physics C: Solid State Physics*, *17*, 1519-1529, 1984a.

Jerauld, G. R., and S. J. Salter, Effect of pore-structure on hysteresis in relative permeability and capillary pressure: Pore-level modeling, *Transport in Porous Media*, *5*, 103-151, 1990.

Jerauld, G. R., L. E. Scriven, and H. T. Davis, Percolation and Conduction on the 3d Voronoi and Regular Networks - a 2nd Case-Study in Topological Disorder, *Journal of Physics C: Solid State Physics*, *17*, 3429-3439, 1984b.

Jia, X., and R. A. Williams, A packing algorithm for particles of arbitrary shapes, *Powder Technology*, *120*, 175-186, 2001.

Jin, G., T. W. Patzek, and D. B. Silin, Physics-based Reconstruction of Sedimentary Rocks, proceedings of the SPE Western Regional / AAPG Pacific Section Joint Meeting, SPE 83587, Soc. of Petroleum Engineers, Long Beach, 2003.

Kaminsky, R., and C. J. Radke, Asphaltenes, water films, and wettability reversal, *SPE Journal*, *2*, 485-493, 1997.

Killough, J. E., Reservoir simulation with history-dependent saturation functions, *SPE Journal*, *16*, 37-48, 1976.

Kovscek, A. R., H. Wong, and C. J. Radke, A Pore-Level Scenario for the Development of Mixed Wettability in Oil-Reservoirs, *AIChE Journal*, *39*, 1072-1085, 1993.

Latham, J. P., Y. Lu, and A. Munjiza, A random method for simulating loose packs of angular particles using tetrahedra, *Geotechnique*, *51*, 871-879, 2001.

Latham, J. P., A. Munjiza, and Y. Lu, On the prediction of void porosity and packing of rock particulates, *Powder Technology*, *125*, 10-27, 2002.

Lee, T. C., R. L. Kashyap, and C. N. Chu, Building Skeleton Models Via 3-D Medial Surface Axis Thinning Algorithms, *Cvgip-Graphical Models and Image Processing*, *56*, 462-478, 1994.

Lenormand, R., C. Zarcone, and A. Sarr, Mechanisms of the Displacement of One Fluid by Another in a Network of Capillary Ducts, *Journal of Fluid Mechanics*, *135*, 337-353, 1983.

Lerdahl, T. R., P. E. Øren, and S. Bakke, A Predictive Network Model for Three-Phase Flow in Porous Media, proceedings of the SPE/DOE Symposium on Improved Oil Recovery, SPE 59311, Soc. of Petroleum Engineers, Tulsa, 2000.

Liang, Z., M. A. Ioannidis, and I. Chatzis, Geometric and topological analysis of three-dimensional porous media: Pore space partitioning based on morphological skeletonization, *Journal of Colloid and Interface Science*, *221*, 13-24, 2000.

Liang, Z. R., C. P. Fernandes, F. S. Magnani, and P. C. Philippi, A reconstruction technique for three-dimensional porous media using image analysis and Fourier transforms, *Journal of Petroleum Science and Engineering*, *21*, 273-283, 1998.

Lindquist, W. B., S. M. Lee, D. A. Coker, K. W. Jones, and P. Spanne, Medial axis analysis of void structure in three-dimensional tomographic images of porous media, *Journal of Geophysical Research - Solid Earth*, *101*, 8297-8310, 1996.

Lindquist, W. B., and A. Venkatarangan, Investigating 3D geometry of porous media from high resolution images, *Physics and Chemistry of the Earth, Part A: Solid Earth and Geodesy*, *24*, 593-599, 1999.

Lindquist, W. B., A. Venkatarangan, J. Dunsmuir, and T. F. Wong, Pore and throat size distributions measured from synchrotron X- ray tomographic images of Fontainebleau sandstones, *Journal of Geophysical Research - Solid Earth*, *105*, 21509-21527, 2000.

Lock, P. A., X. D. Jing, R. W. Zimmerman, and E. M. Schlueter, Predicting the permeability of sandstone from image analysis of pore structure, *Journal of Applied Physics*, *92*, 6311-6319, 2002.

Lu, B. L., and S. Torquato, Lineal-Path Function for Random Heterogeneous Materials, *Physical Review A*, *45*, 922-929, 1992.

Lucia, F. J., *Carbonate reservoir characterization*, Springer-Verlag, Berlin, 1999.

Ma, S., G. Mason, and N. R. Morrow, Effect of contact angle on drainage and imbibition in regular polygonal tubes, *Colloids and Surfaces A: Physicochemical and Engineering Aspects*, *117, 3*, 273-291, 1996.

Man, H. N., and X. D. Jing, Network modelling of wettability and pore geometry effects on electrical resistivity and capillary pressure, *Journal of Petroleum Science and Engineering*, *24*, 255-267, 1999.

Man, H. N., and X. D. Jing, Pore network modelling of electrical resistivity and capillary pressure characteristics, *Transport in Porous Media*, *41*, 263-286, 2000.

Man, H. N., and X. D. Jing, Network modelling of strong and intermediate wettability on electrical resistivity and capillary pressure, *Advances in Water Resources*, *24*, 345-363, 2001.

Manwart, C., U. Aaltosalmi, A. Koponen, R. Hilfer, and J. Timonen, Lattice-Boltzmann and finite-difference simulations for the permeability for three-dimensional porous media, *Physical Review E*, *66*, doi:10.1103/PhysRevE. 1166.016702, 2002.

Manwart, C., and R. Hilfer, Numerical simulation of creeping fluid flow in reconstruction models of porous media, *Physica A: Statistical Mechanics and its Applications*, *314*, 706-713, 2002.

Manwart, C., S. Torquato, and R. Hilfer, Stochastic reconstruction of sandstones, *Physical Review E*, *62*, 893-899, 2000.

Masalmeh, S. K., The effect of wettability heterogeneity on capillary pressure and relative permeability, *Journal of Petroleum Science and Engineering*, *39*, 299-408, 2003.

Mason, G., and N. R. Morrow, Capillary Behavior of a Perfectly Wetting Liquid in Irregular Triangular Tubes, *Journal of Colloid and Interface Science*, *141*, 262-274, 1991.

McDougall, S. R., and K. S. Sorbie, The Impact of Wettability on Waterflooding - Pore-Scale Simulation, *SPE Reservoir Engineering*, *10*, 208-213, 1995.

McDougall, S. R., and K. S. Sorbie, The application of network modelling techniques to multiphase flow in porous media, *Petroleum Geoscience*, *3*, 161-169, 1997.

Morrow, N. R., Effects of surface roughness on contact angle with special reference to petroleum recovery, *Journal of Canadian Petroleum Technology*, *14*, 42-53, 1975.

Mualem, Y., A new model for predicting the hydraulic conductivity of unsaturated porous media, *Water Resources Research*, *12*, 513-522, 1976.

Oak, M. J., Three-phase relative permeability of water-wet Berea, proceedings of the SPE/DOE Seventh Symposium on Enhanced Oil Recovery, SPE 20183, Soc. of Petroleum Engineers, Tulsa, 1990.

Okabe, H., and M. J. Blunt, Pore Space Reconstruction using Multiple-Point Statistics, *Journal of Petroleum Science and Engineering*, *submitted*, 2003.

Øren, P. E., and S. Bakke, Process based reconstruction of sandstones and prediction of transport properties, *Transport in Porous Media*, *46*, 311-343, 2002.

Øren, P. E., and S. Bakke, Reconstruction of Berea sandstone and pore-scale modelling of wettability effects, *Journal of Petroleum Science and Engineering*, *39*, 177-199, 2003.

Øren, P. E., S. Bakke, and O. J. Arntzen, Extending predictive capabilities to network models, *SPE Journal*, *3*, 324-336, 1998.

Patzek, T. W., Verification of a complete pore network simulator of drainage and imbibition, *SPE Journal*, *6*, 144-156, 2001.

Patzek, T. W., and J. G. Kristensen, Shape factor correlations of hydraulic conductance in noncircular capillaries II. Two-phase creeping flow, *Journal of Colloid and Interface Science*, *236*, 305-317, 2001.

Patzek, T. W., and D. B. Silin, Shape factor and hydraulic conductance in noncircular capillaries I. One-phase creeping flow, *Journal of Colloid and Interface Science*, *236*, 295-304, 2001.

Pilotti, M., Reconstruction of clastic porous media, *Transport in Porous Media*, *41*, 359-364, 2000.

Piri, M., and M. J. Blunt, Pore-scale modeling of three-phase flow in mixed-wet systems, proceedings of the 2002 SPE Annual Technical Conference and Exhibition, SPE 77726, Soc. of Petroleum Engineers, San Antonio, 2002.

Rajaram, H., L. A. Ferrand, and M. A. Celia, Prediction of relative permeabilities for unconsolidated soils using pore-scale network models, *Water Resources Research*, *33*, 43-52, 1997.

Reeves, P. C., and M. A. Celia, A functional relationship between capillary pressure, saturation, and interfacial area as revealed by a pore-scale network model, *Water Resources Research*, *32*, 2345-2358, 1996.

Roberts, A. P., D. P. Bentz, and M. A. Knackstedt, Correlating microstructure to the petrophysical properties of porous rocks, proceedings of the 1996 Asia Pacific Oil and Gas Conference, SPE 37024, Soc. of Petroleum Engineers, Adelaide, Australia, 1996.

Ruge, J. W., and K. Stueben, Algebraic Multigrid, *in Multigrid Methods, SIAM Frontiers in Applied Mathematics,* vol. 3, edited by S. F. McCormick, SIAM, Philadelphia, 1987.

Salathiel, R. A., Oil Recovery by Surface Films Drainage In Mixed-Wettability Rocks, *Journal of Petroleum Technology*, *25*, 1216-1224, 1973.

Sok, R. M., M. A. Knackstedt, A. P. Sheppard, W. V. Pinczewski, W. B. Lindquist, A. Venkatarangan, and L. Paterson, Direct and stochastic generation of network models from tomographic images; Effect of topology on residual saturations, *Transport in Porous Media*, *46*, 345-372, 2002.

Spanne, P., J. F. Thovert, C. J. Jacquin, W. B. Lindquist, K. W. Jones, and P. M. Adler, Synchrotron Computed Microtomography of Porous-Media - Topology and Transports, *Physical Review Letters*, *73*, 2001-2004, 1994.

Strebelle, S., Conditional simulation of complex geological structures using multiple-point statistics, *Mathematical Geology*, *34*, 1-21, 2002.

Talukdar, M. S., O. Torsaeter, M. A. Ioannidis, and J. J. Howard, Stochastic reconstruction, 3D characterization and network modeling of chalk, *Journal of Petroleum Science and Engineering*, *35*, 1-21, 2002.

Thovert, J. F., F. Yousefian, P. Spanne, C. G. Jacquin, and P. M. Adler, Grain reconstruction of porous media: Application to a low-porosity Fontainebleau sandstone, *Physical Review E*, *63*, doi:10.1103/PhysRevE.1163.061307, 2001.

Tsakiroglou, C. D., and A. C. Payatakes, Characterization of the pore structure of reservoir rocks with the aid of serial sectioning analysis, mercury porosimetry and network simulation, *Advances in Water Resources*, *23*, 773-789, 2000.

vanGenuchten, M. T., A closed-form equation for predicting the hydraulic conductivity of unsaturated soils, *Soil Science Society of America Journal*, *44*, 892-898, 1980.

Vogel, H. J., Morphological determination of pore connectivity as a function of pore size using serial sections, *European Journal of Soil Science*, *48*, 365-377, 1997.

Vogel, H. J., A numerical experiment on pore size, pore connectivity, water retention, permeability, and solute transport using network models, *European Journal of Soil Science*, *51*, 99-105, 2000.

Vogel, H. J., and K. Roth, A new approach for determining effective soil hydraulic functions, *European Journal of Soil Science*, *49*, 547-556, 1998.

Vogel, H. J., and K. Roth, Quantitative morphology and network representation of soil pore structure, *Advances in Water Resources*, *24*, 233-242, 2001.

Wilkinson, D., and J. F. Willemsen, Invasion Percolation - a New Form of Percolation Theory, *Journal of Physics A: Mathematical and General*, *16*, 3365-3376, 1983.

Wise, W. R., A New Insight on Pore Structure and Permeability, *Water Resources Research*, *28*, 189-198, 1992.

Xie, X., N. R. Morrow, and J. S. Buckley, Contact angle hysteresis and the stability of wetting changes induced by adsorption from crude oil, *Journal of Petroleum Science and Engineering*, *33*, 147-159, 2002.

Yeong, C. L. Y., and S. Torquato, Reconstructing random media, *Physical Review E*, *57*, 495-506, 1998a.

Yeong, C. L. Y., and S. Torquato, Reconstructing random media. II. Three-dimensional media from two-dimensiomal cuts, *Physical Review E*, *58*, 224-233, 1998b.

Zhou, D. G., M. Blunt, and F. M. Orr, Hydrocarbon drainage along corners of noncircular capillaries, *Journal of Colloid and Interface Science*, *187*, 11-21, 1997.

Appendix A

Description of Data Input File

The pore-scale network model is written in C++ and uses a keyword based input file. Most keywords are optional and there is no necessary order to them. Comments in the data file are indicated by '%', resulting in the rest of the line being discarded. All keywords should be terminated by '#'. The input data file can be supplied as an argument to the executable.

```
C:\path_to_executable\poreflow.exe default.dat
```

A.1 Required keywords

A.1.1 NETWORK

This specifies the files containing data such as inscribed radii, volumes and the connection list defining the network topology.

1. Are the files in binary format? Binary files take up less disk space and load substantially quicker than ASCII files. However, binary files can not be interchanged between different computer platforms (e.g. Windows and Solaris).
2. The network data are located in four files when using ASCII format (*filename_node1.dat, filename_node2.dat, filename_link1.dat, filename_link2.dat*) and two files when using binary format (*filename_node.bin* and *filename_link.bin*). Only the prefix *filename* is to be specified.

```
NETWORK
F  ../data/berea
#
```

A.1.2 SAT_TARGET

Each line represents a separate flooding cycle (e.g. primary oil flooding, secondary water flooding, *etc*).

1. Final water saturation target after the flooding cycle (fraction). The actual value might not actually be reached due to trapping or water retained in corners.
2. The cycle can also be terminated when a capillary pressure (Pa) is reached.
3. Target water saturation interval (fraction) between reporting results. The state of the model will be evaluated at the first possible configuration after the incremental target has been reached.
4. Target capillary pressure interval (Pa) between reporting results.
5. Should relative permeability be calculated? If this is not of primary interest it can be very time saving to set this option to false (‘`F`’) as most of the CPU time is spent solving the pressure field, required for relative permeability calculations.
6. Calculate resistivity index? CPU time required for this is the same as for relative permeability calculations.

```
SAT_TARGET
0.00    66380.0    0.02     5000.0    F    F
1.00    -1.0E21    0.02    10000.0    T    T
0.00     1.0E21    0.05     5000.0    T    T
#
```

A.1.3 EQUIL_CON_ANG

Once invaded by oil the wettability of a pore element will typically change. Advancing and receding contact angles are defined in terms of an intrinsic contact angle, either distributed according to a truncated Weibull distribution

$$\theta_i = (\theta_{i,max} - \theta_{i,min})\left(-\delta \ln\left[x\left(1 - e^{-1/\delta}\right) + e^{-1/\delta}\right]\right)^{1/\gamma} + \theta_{i,min}, \qquad \text{(A.1)}$$

where δ and γ are parameters defining the shape of the distribution and x is a random number between 0 and 1, or alternatively distributed uniformly by setting δ and γ to less than 0 in the input file.

1. What model should be used for determining receding and advancing contact angles? Model 1 sets $\theta_i = \theta_r = \theta_a$. Model 2 separates θ_r and θ_a by a constant angle, with $\theta_a(\theta_i = 0°) = 0°$ and $\theta_r(\theta_i = 180°) = 180°$. With a separation angle of 25.2° this corresponds to the Class II model defined by Morrow [1975]. Model 3 corresponds to the Class III model defined by Morrow [1975] and is illustrated in Figure 3.6.
2. Minimum intrinsic contact angle (degrees)
3. Maximum intrinsic contact angle (degrees)
4. δ exponent (set this to a negative number for uniform distribution).
5. γ exponent (set this to a negative number for uniform distribution).
6. How are the contact angles distributed on the pore-scale? ‘`rMax`’ associates the larger pores (in terms of inscribed radius) with the larger angles, ‘`rMin`’ associates the larger pores with the smaller angles and ‘`rand`’ distributes the angles randomly. Throats are assigned the angle of either connecting pore based on equal probability.
7. The separation angle for intrinsic contact angle model 2.

```
EQUIL_CON_ANG
2    30.0    60.0    -1.0    -1.0    rand    25.2
#
```

A.2 Keywords controlling the reporting of results

The remaining keywords are all optional. The default parameters are those given as example in each section, unless otherwise specified.

A.2.1 TITLE

All output files are prefixed by the indicated title (e.g. *title*_draincycle_1.out). If this keyword is omitted the title is taken to be the same as the name of the input data file.

```
TITLE
default
#
```

A.2.2 RES_FORMAT

There is a choice between three formats (‘`excel`’, ‘`matlab`’ or ‘`std`’) for the results files containing capillary pressure, relative permeability, *etc*. The excel format will create files with extension *.csv*, the matlab format will create files with extension *.m* and the standard format will create files with extension *.out*.

```
RES_FORMAT
std
#
```

A.2.3 WRITE_NET

Using this keyword it is possible to write the network that was used for the simulation to file. Omitting this keyword will result in no network files being written.

1. Should the files be written in binary format (true ‘`T`’ or false ‘`F`’)?
2. The filename along with the relative path to be used. The extensions, *_node1.dat*, *_node.bin, etc*., will be automatically added to the filename.

```
WRITE_NET
T     ../data/sandstone_s8
#
```

A.2.4 OUTPUT

Using this keyword it is possible to create output files containing the properties of individual network elements in terms of radii, volumes, connection numbers*, etc*. (*title_pores.out* and *title_throats.out*) and files containing the distribution of saturations in the network at every reporting interval (*title_pores_Sw.out* and *title_throats_Sw.out*). Both sets of files can become very space consuming. The file format used is the same as that used by the geostatistical package GSLIB [*Deutsch and Journel*, 1998]. The data are stored in columns. The first row is some arbitrary file header, followed by the number of data columns and the titles of each column.

1. Create files with the properties of individual network elements (true ‘`T`’ or false ‘`F`’)?
2. Create files with the water saturation of all pores and throats at every reporting interval (true ‘`T`’ or false ‘`F`’)?

```
OUTPUT
F     F
#
```

A.2.5 FILLING_LIST

Output files indicating the sequence that pores and throats got filled during the simulation can be created. The resulting files are formatted for easy entry into matlab for post-processing, with the filenames being *poreLocation.m, throatConnection.m, fill_draincycle_1.m* and *fill_imbcycle_2.m*.

1. Create filling list for oil flooding cycles (true ‘`T`’ or false ‘`F`’)?
2. Create filling list for water flooding cycles (true ‘`T`’ or false ‘`F`’)?
3. Create files with pore location and throat connection data (true ‘`T`’ or false ‘`F`’)?

```
FILLING_LIST
F    F    F
#
```

A.3 Convergence related keywords

A.3.1 SOLVER_TUNE

The pressure solver used for relative permeability calculations is an algebraic multigrid solver [*Ruge and Stueben*, 1987].

1. The performance of the solver can be tuned by varying the solution tolerance. A lower tolerance will result in an increased number of required solver iterations.
2. Memory allocation for the solver can be adjusted by the memory scaling factor. For large models it might be necessary to increase the factor above the default value.
3. Performance related information about the solver is written to the file *fort.11*. A value of 0 produces minimal information whereas a value of 3 will produce substantial information about tolerance, memory requirements*, etc*.
4. Setting this flag to true (‘`T`’) will output solver information to screen rather than to file.
5. In some cases it might be necessary to discard conductances below a certain threshold to ensure solver convergence. This option should be used with great

care and only when problems are observed (typically when solving for the oil pressure in cycles greater than the secondary).

```
SOLVER_TUNE
1.0E-15    5    0    F   0.0E-30
#
```

A.3.2 SAT_COVERGENCE

This keyword controls the accuracy at which the incremental water saturation target is reached. It is generally not feasible to calculate water saturation after each filling event, as that would be computationally very expensive. When starting a new saturation step, an approximate number of required filling events is estimated. This estimate is however quite uncertain as the water saturation does not vary linearly with the number of filling events. The actual number of filling events performed before recalculating water saturation should therefore be a relatively small fraction of the initial estimate. Subsequently an updated estimate of the required number of filling events is made, using information from the previous step. Still, only a fraction of the estimated filling events should be performed before recalculating water saturation, as the estimate remains fairly uncertain.

1. Minimum number of filling events between calculating water saturation.
2. Fraction applied to the initial estimate of required number of filling events.
3. Fraction applied to subsequent estimates of required number of filling events.
4. Maximum increase factor in required number of filling events estimates.
5. Only solve for relative permeability when a stable capillary configuration is reached (true ‘`T`’ or false ‘`F`’)?

```
SAT_COVERGENCE
10    0.1    0.8    2.0    F
#
```

A.3.3 SAT_COMPRESS

This keyword will change the target saturation interval, specified by entry 3 in `SAT_TARGET`, once relative permeability of the defending fluid drops below a specified threshold. If this keyword is omitted, the originally specified interval target will be used.

1. Relative permeability threshold.

2. New target saturation interval between the reporting of results.
3. Apply to oil flooding cycle (true ‘`T`’ of false ‘`F`’)?
4. Apply to water flooding cycle (true ‘`T`’ of false ‘`F`’)?

```
SAT_COMPRESS
0.1    0.005    T    F
#
```

A.3.4 RELPERM_DEF

1. Use flow rate at residual saturation (‘`residual`’) to calculate relative permeability, rather than that at single phase conditions (‘`single`’)? Using residual saturations will normalize all relative permeabilities between 0 and 1.
2. Maintain the conditions for trapping as defined in keyword `TRAPPING` (true ‘`T`’ or false ‘`F`’)? If set to false, the defending fluid only has to be connected to one face to be considered as not trapped, even when injecting from a single face of the network.

```
RELPERM_DEF
single    T
#
```

A.4 Keywords specifying fluid and rock properties

A.4.1 INIT_CON_ANG

The initial receding contact angles θ_r, used in elements that have never been invaded by oil, are distributed either uniformly or according to a truncated weibull distribution.

1. Minimum initial receding contact angle (degrees).
2. Maximum initial receding contact angle (degrees).
3. δ exponent (set to a negative number for a uniform distribution).
4. γ exponent (set to a negative number for a uniform distribution).

```
INIT_CON_ANG
0.0    0.0    0.2    3.0
#
```

A.4.2 FRAC_CON_ANG

Not all oil-invaded elements need necessarily attain oil-wet characteristics in mixed-wet systems. This effect can be modelled by defining two separate distributions of intrinsic contact angles. This wettability alteration will be applied after primary oil-flooding and will replace the contact angles defined by `EQUIL_CON_ANG` in those elements selected to belong to this second distribution. Only a single distribution, as defined by `EQUIL_CON_ANG`, will exist if this keyword is omitted. The first line of data defines the second distribution.

1. The fraction of oil-invaded elements following primary oil flooding whose contact angles should be altered.
2. Should the fraction be pore volume based (‘`T`’) or a quantitative split between pores (‘`F`’).
3. Minimum intrinsic contact angle (degrees).
4. Maximum intrinsic contact angle (degrees).
5. δ exponent (set to a negative number for a uniform distribution).
6. γ exponent (set to a negative number for a uniform distribution).

The second line defines how this second distribution is distributed on the pore-scale. Four approaches are possible. The first approach assumes that the second distribution is spatially correlated. This approach is selected by the keyword ‘`corr`’ followed by the diameter (in terms of pores) of the correlated regions. One can also select to make the largest (‘`rMax`’) or smallest (‘`rMin`’) pores belong to the second distribution. The final approach is randomly selecting the pores (‘`rand`’). In the last three approaches the connecting throats will be assigned the same contact angle as the pore with a probability equal to the altered fraction (as defined by the first entry in line 1).

1. How should the second distribution be distributed on the pore-scale (‘`corr`’, ‘`rMax`’, ‘`rMin`’ or ‘`rand`’)?
2. Correlation diameter when using the spatially correlated approach.

```
FRAC_CON_ANG
0.7    T    100.0    130.0    -1.0    -1.0
corr    7
#
```

A.4.3 FLUID

The fluid description is very simple with no pressure dependent properties.

1. Interfacial tension (mN·m^{-1})
2. Water viscosity (cp)
3. Oil viscosity (cp)
4. Water resistivity (Ohm·m)
5. Oil resistivity (Ohm·m)
6. Water gravity (kg·m^{-3})
7. Oil gravity (kg·m^{-3})

```
FLUID
30.0    1.0    1.0    1.2    1000.0    1000.0    1000.0
#
```

A.4.4 GRAV_CONST

Define the gravitational constant g ($z = 0$ is at the bottom of the model).

1. Gravitational component in the x direction (m/s^2).
2. Component in y direction.
3. Component in z direction.

```
GRAV_CONST
0.0    0.0    -9.81
#
```

A.4.5 PRS_DIFF

It is possible to include gravity effects when solving the pressure field. How much influence it will have depends on both the fluid density and the pressure difference imposed across the model.

1. Inlet pressure (Pa).
2. Outlet pressure (Pa).

3. Should gravity effects be included when solving the pressure field (true ‘`T`’ or false ‘`F`’)?

```
PRS_DIFF
1.0    0.0    F
#
```

A.5 Keywords for various network modelling options

A.5.1 RAND_SEED

This is the seed to the random number generator, which should be a large positive integer. If the keyword is omitted the computer clock will be used as seed.

```
RAND_SEED
54356457
#
```

A.5.2 CALC_BOX

Most of the elements close to the injection faces will be filled by the injecting fluid, resulting in most of the pressure loss occurring in this region when solving the pressure field for the displaced fluid. To avoid these boundary effects it is normal to only use a fraction of the network (away from the injecting faces) when calculating saturation and relative permeabilities.

1. Dimensionless location for lower boundary.
2. Dimensionless location for higher boundary.

```
CALC_BOX
0.50    1.00
#
```

A.5.3 PRS_BDRS

To avoid boundary effects only a section of the network is used for calculating relative permeability and water saturation, as defined by the `CALC_BOX` keyword. When computing relative permeability it is possible to solve the pressure field in the entire network, using the average pressure at the section boundaries for relative permeability,

$$k_{rp} = \frac{q_{tmp}\,\Delta P_{sp}}{q_{tsp}\,\Delta P_{mp}}, \tag{A.2}$$

where ΔP_{sp} and ΔP_{mp} are the single and multiphase pressure drops for phase p across the selected section. Alternatively the pressure field can be solved only within the selected section by applying constant pressures at the section boundaries, with relative permeability given by (3.40).

1. Solve the pressure field in the entire network (true ‘`T`’ or false ‘`F`’)?
2. Record the average pressure at cross-sectional planes within the selected section of the network (true ‘`T`’ or false ‘`F`’)? This is just for reporting purposes and the pressures will be written to the results files.
3. The number of cross-sectional pressure planes where the average pressure is to be recorded.

```
PRS_BDRS
F    F    0
#
```

A.5.4 TRAPPING

This keyword controls some aspects of the trapping routine. If fluid is injected from only one face of the model, the defending fluid must be connected to both the inlet and outlet to be considered as not trapped. If injecting from both faces, the defending fluid only has to be connected to one face to be considered as not trapped.

1. Inject fluid from inlet face?
2. Inject fluid from outlet face?
3. Allow drainage of dangling ends (pores with only one connecting throat) through wetting layers.
4. The water conductance ($m^4 \cdot Pa^{-1} \cdot s^{-1}$) of circular elements completely filled with oil.

```
TRAPPING
T    F    T    0.0E-30
#
```

A.5.5 POINT_SOURCE

Rather than inject fluid from the face of the network, it is possible to inject from any interior pore. If this keyword is included it will take precedence over the `TRAPPING` keyword, and no fluid will be injected from any network face.

1. Pore index to inject from. This will have to be greater than 0 and less than the total number of pores.

```
POINT_SOURCE
5050
#
```

A.5.6 PORE_FILL_ALG

During spontaneous invasion, the capillary entry pressure for pore bodies will depend on the number *n* of adjacent oil-filled throats (cooperative pore body filling). Several different models have been proposed in the literature. The default models is the one proposed by Blunt [1998] and is described in Chapter 3.3.2 (‘`blunt2`’),

$$P_c = \frac{2\sigma\cos\theta_a}{r} - \sigma\sum_{i=1}^{n} A_i x_i\,, \tag{A.3}$$

where A_i are arbitrary numbers and x_i are random numbers between zero and one. Another model proposed by Blunt [1997a] is given by (‘`blunt1`’)

$$P_c = \frac{2\sigma\cos\theta_a}{r + \sum_{i=1}^{n} A_i x_i}\,. \tag{A.4}$$

Also implemented is the model proposed by Øren *et al.* [1998], given by (‘`oren1`’)

$$P_c = \frac{2\sigma\cos\theta_a}{r + \sum_{i=1}^{n} A_i r_i x_i}\,, \tag{A.5}$$

where r_i is the radius of connecting throat *i*. A similar model correcting for non-circular pore shapes is given by (‘`oren2`’)

$$P_c = \frac{(1 + 2\sqrt{\pi G})\,\sigma\cos\theta_a}{r + \sum_{i=1}^{n} A_i r_i x_i}\,. \tag{A.6}$$

1. Model to be used for cooperative pore body filling (‘`blunt1`’, ‘`blunt2`’, ‘`oren1`’ or ‘`oren2`’).

```
PORE_FILL_ALG
blunt2
#
```

A.5.7 PORE_FILL_WGT

The weights A_i, used in the models for pore body filling, will clearly have an impact on the filling sequence during spontaneous invasion. These are specific to the chosen model, specified by the keyword `PORE_FILL_ALG`. Typical values for $A_1 - A_6$ for the models proposed by Øren *et al.* [1998] are 0.0, 0.5, 1.0, 2.0, 5.0 and 10.0. The approach for calculating the weights for the default model (‘`blunt2`’) by Blunt [1998] is given in Chapter 3.3.2.

1. Weight for an I_1 event, A_1.
2. Weight for an I_2 event, A_2.
3. Weight for an I_3 event, A_3.
4. Weight for an I_4 event, A_4.
5. Weight for an I_5 event, A_5.
6. Weight for an I_6 event, A_6, and up.

```
PORE_FILL_WGT
0    15000    15000    15000    15000    15000
#
```

A.6 Keywords for tuning the network properties

If any of the keywords in this section are omitted, the original properties of the network will be retained.

A.6.1 MODIFY_PORO

All pore and throat volumes can be adjusted by a constant factor such that the target porosity is reached. We assume that the total porosity, $\phi_t = \phi_n + \phi_c$, is made up of the net porosity ϕ_n and the micro and clay bound porosity ϕ_c.

1. Target net porosity, ϕ_n.
2. Target micro and clay bound porosity, ϕ_c.

```
MODIFY_PORO
0.24    0.03
#
```

A.6.2 MODIFY_RAD_DIST

This keyword is used for modifying the pore size distribution, useful when tuning a network to become representative of a given type of porous medium. The first line of data refers to throats and the second to pores. The various options for pores are identical to those for throats.

1. There are 6 approaches available for how the pore/throat size distribution should be modified. Setting the index to ‘`-1`’ will bundle the throats together with the pores or vice versa. So if the first line of data is set to ‘`-1`’ the second line will apply to pores and throats, rather than just pores. Setting the index to ‘`0`’ will result in nothing being done. The pore/throat size distribution can be read from file by setting the index to ‘`1`’. Setting the index to ‘`2`’ will result in the pore/throat radius being determined by the radii of connecting pores or throats. When setting the index to ‘`3`’, each pore/throat radius will be multiplied by a constant factor. The shape of the pore/throat size distribution can also be stretched or compressed by setting the index to ‘`4`’. Finally, by setting the index to ‘`5`’ the radii are randomly distributed, either uniformly or according to a truncated weibull distribution. For options 1 to 5 additional parameters are needed.

A.6.2.1 READ FROM FILE (OPTION ‘1’)

2. The file containing the target distribution. The file should contain two columns. The first column is the pore/throat diameter in micrometers. This should be monotonically decreasing. The second column should be the corresponding fraction of pore/throat space occupied, going from 0 to 1.

3. If the target distribution is derived from mercury injection data it might be necessary to apply a lower cut-off to exclude effects from mercury entering the micro porosity. Micro porosity (and clays) should be accounted for with the `MODIFY_PORO` keyword. No cut-off will be applied if a negative value is specified.

4. It might also be necessary to apply a higher cut-off.

A.6.2.2 ASPECT RATIO (OPTION ‘2’)

The average connecting radius will be multiplied by a user defined aspect ratio, α, distributed uniformly or according to a truncated weibull distribution. The radius of a pore body is then given by

$$r_p = \max\left(\alpha \frac{\sum_{i=1}^{n} r_i}{n},\ \max(r_i) \right), \tag{A.7}$$

while the throat radius is given by

$$r_t = \min\left(\alpha \frac{\sum_{i=1}^{n} r_i}{n},\ \min(r_i) \right). \tag{A. 8}$$

2. Minimum aspect ratio. If minimum and maximum aspect ratios are set to a negative number the original ratios of the network will be used.

3. Maximum aspect ratio.

4. δ exponent (set to a negative number for a uniform distribution).

5. γ exponent (set to a negative number for a uniform distribution).

A.6.2.3 MULTIPLICATION FACTOR (OPTION ‘3’)

2. Multiplication factor.

A.6.2.4 STRETCH OR COMPRESS DISTRIBUTION (OPTION ‘4’)

The original pore/throat size distribution will be either stretched or compressed along the size axis according to the function

$$r = \frac{r_o^{a}}{\bar{r}_o^{a-1}}, \tag{A.9}$$

where r_o is the original radius and $\bar{r}_o$ is the pore volume based average radius.

2. The exponent a determines if the distribution is stretched ($a > 1$) or compressed ($a < 1$).

3. Should the function be applied to pores or throats with radii greater than the volume based average (true '`T`' or false '`F`')?
4. Should the function be applied to pores or throats with radii less than the volume based average (true '`T`' or false '`F`')?

A.6.2.5 NEW RANDOM DISTRIBUTION (OPTION '5')

2. Minimum radius.
3. Maximum radius.
4. δ exponent (set to a negative number for a uniform distribution).
5. γ exponent (set to a negative number for a uniform distribution).

The third line of data contains some additional parameters.

1. Should the average throat length to radius ratio be maintained from the original network? If this is set to true ('`T`') all throat lengths will be scaled along with pore locations and absolute model size.
2. Should the new pore and throat size distributions be written to file (true '`T`' or false '`F`')? The files will be named *RadDist_pores.csv* and *RadDist_throats.csv*.
3. How many data points should there be in the distributions written to file?

```
MODIFY_RAD_DIST
1    ./hg_final.txt    -1.0    -1.0
2    -1.0    -3.0    0.2    3.0
T    T    50
#
```

A.6.3 MODIFY_G_DIST

In the same way that pore and throat size distributions can be modified, so can the various shape factors. Again, the first line of data refers to throats and the second to pores, and the various options for pores are identical to those for throats. Square ($G = 1/16$) and circular ($G = 1/4\pi$) elements will not be modified. For triangular elements the maximum shape factor is $\sqrt{3}/36$ which represents an equilateral triangle.

1. There are 5 approaches available for how the shape factor distribution should be modified. Setting the index to '`-1`' will bundle the throats together with the pores or vice versa. So if the first line of data is set to '`-1`' the second line will

apply to pores and throats, rather than just pores. Setting the index to ‘`0`’ will result in nothing being done. The shape factor distribution can be read from file by setting the index to ‘`1`’. When setting the index to ‘`3`’, each pore or throat shape factor will be multiplied by a constant factor. The shape of the shape factor distribution can also be stretched or compressed by setting the index to ‘`4`’. Finally, by setting the index to ‘`5`’ the shape factors are randomly distributed, either uniformly or according to a truncated weibull distribution. For options 1 to 5 additional parameters are needed, but these are identical to those described for MODIFY_RAD_DIST and will not be repeated here. When applying (A.9) to shape factors, $\bar{G}_o$ refers to the median rather than the volume based average. If the distributions are read from file, the second column refers to the quantitative fraction of pores or throats.

The third line contains some additional parameters.

1. Should the new pore and throat shape factor distributions be written to file (true ‘`T`’ or false ‘`F`’)? The files will be named *ShapeFactDist_pores.csv* and *ShapeFactDist_throats.csv*.
2. How many data points should there be in the distributions written to file?

```
MODIFY_G_DIST
-1
5    0.001    0.04811    -1.0    -1.0
F    50
#
```

A.6.4 MODIFY_CONN_NUM

The average coordination number of the network is very important for fluid connectivity and hence relative permeability. For a given network this can be reduced by removing throats.

1. Target coordination number. This should be less than the original (can be found from the *.prt* file).
2. Which throats should be removed? Four different options are available. Lowest volume (‘`volume`’), smallest shape factor (‘`shape`’), smallest radius (‘`radius`’) or selected at random (‘`rand`’).

```
MODIFY_CONN_NUM
4.0    radius
#
```

A.6.5 MODIFY_MOD_SIZE

By changing the absolute size of the network the absolute permeability will also change. All lengths will be scaled (pore positions, radii, volumes and lengths). In most cases it is however best to let the model size be scaled through the keyword `MODIFY_RAD_DIST` where the length to radius ratio is maintained from the original network.

1. Fractional change to the absolute size of the model.

```
MODIFY_MOD_SIZE
1.2
#
```

A.7 Examples of input data files

A.7.1 Water-wet Berea sandstone

This is the data file used for Chapter 4.2.

```
SAT_TARGET
%finalSat   maxPc   maxDeltaSw   maxDeltaPc   calcKr    calcI
   0.00    1.0E21     0.02        500000.0      T         F
   1.00   -1.0E21     0.02        500000.0      T         F
#

INIT_CON_ANG
% min   max   delta  gamma
  0.0   0.0   -0.2   -3.0
#

EQUIL_CON_ANG
% model  min   max   delta  gamma scheme m2_separation
    3   50.0  60.0   -1.0   -1.0   rand      25.2
#

RES_FORMAT
  matlab
#

REL_PERM_DEF
% kr_def  trpCond
  single     F
#
```

```
SAT_COMPRESS
% kr_thres  maxDeltaSw  OilFlood  WatFlood
     0.1      0.001         T        T
#

TRAPPING
%   Inject fluid from     allow drainage      water cond in
%      entry  exit       of dangling ends    filled circ elem
         T     F                T               0.0E-30
#

SOLVER_TUNE
%     min    memory scaling   solver    verbose   conductance
%  tolerance    factor         output    solver     cut-off
    1.0E-30      8             0          F         0.0
#

PRS_BDRS
% calc kr using   record press    num press
%  avg press        profiles      profiles
      F                F              20
#

PORE_FILL_ALG
  blunt2
#

PORE_FILL_WGT
  0.0  18904  18904  18904  18904  18904
#

FLUID
% interfacial   water       oil      water   oil     water     oil
%  tension    viscosity  viscosity  resist. resist. density  density
%   (mN/m)      (cp)       (cp)     (Ohm.m) (Ohm.m) (kg/m3)  (kg/m3)
     30.0       1.05       1.39       1.2   1000.0  1000.0   1000.0
#

CALC_BOX
  0.5   1.0
#

NETWORK
% bin     filename
   T   ../Data/Berea
#

SAT_COVERGENCE
%  minNumFillings   initStepSize   nextStepSize  maxIncr  stable
       10                0.1            0.8        2.0       F
#
```

A.7.2 Water-wet sand pack

This is the data file used for Chapter 4.3.

```
RAND_SEED
  9512367
#
```

```
SAT_TARGET
%finalSat   maxPc   maxDeltaSw   maxDeltaPc   calcKr    calcI
   0.00    16000.0    0.3        100000.0       F        F
   1.00   -1.0E21     0.3        100000.0       F        F
   0.00    16000.0    0.02        1000.0        T        F
   1.00   -1.0E21     0.02        1000.0        T        F
#

SAT_COMPRESS
% kr_thres  maxDeltaSw  OilFlood  WatFlood
    0.1      0.005         F         T
#

INIT_CON_ANG
% min   max   delta  gamma
  0.0   0.0    0.2    3.0
#

EQUIL_CON_ANG
% model  min   max   delta  gamma scheme m2_separation
   3    30.0  40.0   -1.0   -1.0    rand     25.2
#

RES_FORMAT
  matlab
#

TRAPPING
%   Inject fluid from     allow drainage      water cond in
%      entry  exit       of dangling ends    filled circ elem
         T     F                T                0.0E-30
#

RELPERM_DEF
% kr_def  trpCond
  residual    F
#

SOLVER_TUNE
%     min    memory scaling   solver    verbose   conductance
%  tolerance    factor        output    solver     cut-off
   1.0E-30         7            0          F         0.0
#

PRS_BDRS
% calc kr using   record press    num press
%  avg press        profiles      profiles
       F               F             20
#

PORE_FILL_ALG
  blunt2
#

PORE_FILL_WGT
  0  7473   7473   7473   7473   7473
#
```

```
FLUID
% interfacial   water       oil      water   oil     water     oil
%  tension    viscosity  viscosity  resist. resist. density  density
%   (mN/m)      (cp)      (cp)       (Ohm.m) (Ohm.m) (kg/m3)  (kg/m3)
     70.25      0.97       0.018     1.2    1000.0   1000.0   1.22
#

CALC_BOX
  0.50  1.00
#

NETWORK
% bin     filename
  T   ../../../Data/dury_final
#

SAT_COVERGENCE
%  minNumFillings   initStepSize   nextStepSize  maxIncr  stable
       10               0.1            0.8         2.0      F
#
```

A.7.3 Mixed-wet Berea sandstone

This is the data file used for Chapter 5.1 for the variable wettability case and S_{wi} = 0.24.

```
RAND_SEED
  6844625
#

SAT_TARGET
%finalSat   maxPc   maxDeltaSw   maxDeltaPc    calcKr    calcI
  0.24     1.0E21      0.20     500000.0        F       F
  0.90    -1.0E21      0.015    500000.0        T       F
  0.14     1.0E21      0.015    500000.0        T       F
  0.91    -1.0E21      0.015    500000.0        T       F
#

INIT_CON_ANG
% min   max   delta  gamma
 0.00   0.00   0.2    3.0
#

EQUIL_CON_ANG
% model  min   max   delta  gamma scheme m2_separation
   3    50.0  60.0   -1.0   -1.0    rand    25.2
#

FRAC_CON_ANG
% fraction  volBased  min     max   delta    gamma
    0.94        T     90.0   112.0   -10.0   -1.0
%  method
   rMax
#

RES_FORMAT
  matlab
#
```

```
TRAPPING
%   Inject fluid from     allow drainage      water cond in
%      entry  exit       of dangling ends    filled circ elem
         T     F               T                 0.0E-30
#

SOLVER_TUNE
%     min    memory scaling   solver    verbose   conductance
%  tolerance    factor        output    solver     cut-off
    1.0E-30       8             0          F       0.0E-35
#

PRS_BDRS
% calc kr using   record press    num press
%  avg press        profiles      profiles
      F                F             50
#

PORE_FILL_ALG
  blunt2
#

PORE_FILL_WGT
  0.0   18904   18904   18904   18904   18904
#

FLUID
% interfacial   water       oil      water   oil     water     oil
%  tension    viscosity  viscosity  resist. resist. density  density
%   (mN/m)      (cp)       (cp)     (Ohm.m) (Ohm.m) (kg/m3)  (kg/m3)
     12.3       0.991      5.23       1.2    1000.0  1044.0   845.0
#

CALC_BOX
  0.50   1.00
#

NETWORK
% bin           filename
   T    ../../Data/Berea_76pc_clay
#
```

A.7.4 Mixed-wet carbonate

This is the data file used for Chapter 5.2 for sample 2 with a lower oil-wet fraction.

```
SAT_TARGET
%finalSat   maxPc   maxDeltaSw   maxDeltaPc   calcKr    calcI
  0.220    1.0E21      0.20       500000.0       F       F
  1.000   -1.0E21      0.02       500000.0       T       F
  0.030    1.0E21      0.02       500000.0       F       F
#

INIT_CON_ANG
% min   max   delta  gamma
  0.0   0.0    0.2    3.0
#
```

```
EQUIL_CON_ANG
% model  min   max   delta  gamma scheme m2_separation
    3   25.0  65.0   -1.0   -1.0    rand     25.2
#

FRAC_CON_ANG
% fraction  volBased  min     max   delta    gamma
    0.65        T    80.0    82.0   -1.0     -1.0
%  method
    rmin
#

RES_FORMAT
  matlab
#

TRAPPING
%   Inject fluid from     allow drainage      water cond in
%      entry  exit       of dangling ends    filled circ elem
         T     F                T                0.0E-30
#

SOLVER_TUNE
%     min    memory scaling   solver    verbose   conductance
%  tolerance    factor        output    solver     cut-off
    1.0E-40       7             0         F        0.0E-40
#

PRS_BDRS
% calc kr using   record press    num press
%  avg press        profiles      profiles
      F                F             20
#

PORE_FILL_ALG
  blunt2
#

PORE_FILL_WGT
  0  844113  844113  844113  844113  844113
#

FLUID
% interfacial   water       oil      water   oil     water     oil
%  tension    viscosity  viscosity  resist. resist. density  density
%   (mN/m)      (cp)       (cp)     (Ohm.m) (Ohm.m) (kg/m3)  (kg/m3)
     29.9       0.927     6.17        1.2   1000.0   829.3   1094.6
#

PRS_DIFF
% prsIn  prsOut  gravity
   1.0    0.0      T
#

CALC_BOX
  0.50  1.00
#
```

```
NETWORK
% bin           filename
  T   ../../Data/Shell_carb_24
#
```

A.7.5 Mixed-wet sandstone

This is the data file used for Chapter 5.3 when using spatially correlated mixed-wetting.

```
SAT_TARGET
%finalSat   maxPc   maxDeltaSw   maxDeltaPc    calcKr    calcI
   0.000    1.0E21     0.20      500000.0         F       F
   1.000   -1.0E21     0.01      500000.0         T       F
   0.000    1.0E21     0.20      500000.0         F       F
#

INIT_CON_ANG
% min   max   delta  gamma
  0.0   0.0    0.2    3.0
#

EQUIL_CON_ANG
% model  min   max   delta  gamma scheme m2_separation
    3    0.0  60.0   -1.0   -1.0    rand     25.2
#

FRAC_CON_ANG
% fraction  volBased   min     max    delta    gamma
    0.43        T     100.0   160.0   -1.0     -1.0
%  method  corrDiam
    corr     7
#

RES_FORMAT
  matlab
#

TRAPPING
%   Inject fluid from     allow drainage      water cond in
%      entry  exit       of dangling ends    filled circ elem
         T     F                T                0.0E-30
#

SOLVER_TUNE
%     min    memory scaling   solver    verbose   conductance
%  tolerance    factor        output    solver     cut-off
    1.0E-40       7             0          F        0.0E-40
#

PRS_BDRS
% calc kr using   record press    num press
%  avg press        profiles      profiles
      F                F             20
#
```

```
PORE_FILL_ALG
  blunt2
#

PORE_FILL_WGT
  0  33472  33472  33472  33472  33472
#

FLUID
% interfacial   water       oil      water   oil     water     oil
%  tension    viscosity  viscosity  resist. resist. density  density
%   (mN/m)      (cp)       (cp)     (Ohm.m) (Ohm.m) (kg/m3)  (kg/m3)
     30.0       1.05       1.39       1.2   1000.0  1000.0   1000.0
#

PRS_DIFF
% prsIn  prsOut  gravity
   10.0   0.0      T
#

CALC_BOX
  0.50  1.00
#

NETWORK
% bin          filename
  T      ../../Data/Shell_sst
#

MODIFY_PORO
% phi_eff   phi_clay
   0.18       0.09
#
```

A.7.6 Oil-wet sandstone

This is the data file used for Chapter 5.4.

```
SAT_TARGET
%finalSat   maxPc   maxDeltaSw   maxDeltaPc   calcKr    calcI
  0.03     1.0E21     0.20       500000.0       F        F
  1.00    -1.0E21     0.01       500000.0       T        F
  0.03     1.0E21     0.20       500000.0       F        F
#

INIT_CON_ANG
% min   max   delta  gamma
 20.0  60.0   -0.2   -3.0
#

EQUIL_CON_ANG
% model  min   max   delta  gamma scheme m2_separation
   3    70.0  123.0  -1.0   -1.0    rand     25.2
#

RES_FORMAT
  matlab
#
```

```
TRAPPING
%   Inject fluid from     allow drainage      water cond in
%      entry  exit       of dangling ends    filled circ elem
         T     F                T               0.0E-30
#

SOLVER_TUNE
%     min    memory scaling   solver    verbose   conductance
%  tolerance    factor        output    solver     cut-off
    1.0E-40       8             0         F        0.0E-40
#

PRS_BDRS
% calc kr using   record press    num press
%  avg press        profiles      profiles
      F                F             20
#

PORE_FILL_ALG
  blunt2
#

PORE_FILL_WGT
  0  24837  24837  24837  24837  24837
#

FLUID
% interfacial   water       oil      water   oil     water     oil
%  tension    viscosity  viscosity  resist. resist. density  density
%   (mN/m)      (cp)       (cp)     (Ohm.m) (Ohm.m) (kg/m3)  (kg/m3)
    30.0        1.0       0.289      1.2    1000.0  1000.0    800.0
#

PRS_DIFF
% prsIn  prsOut  gravity
  10.0    0.0       T
#

CALC_BOX
  0.5  1.0
#

NETWORK
% bin           filename
   T   ../../Data/Statoil_sst_40avg
#

MODIFY_PORO
% phi_eff  phi_clay
   0.153     0.0
#
```